DEVELOPMENT OF MODALITY-INDEPENDENT ELASTOGRAPHY AS A METHOD OF BREAST CANCER DETECTION

By

Jao Jih Ou

Dissertation

Submitted to the Faculty of the

Graduate School of Vanderbilt University

in partial fulfillment of the requirements for

the degree of

DOCTOR OF PHILOSOPHY

in

Biomedical Engineering

May, 2008

Nashville, Tennessee

Approved:

Professor Michael I. Miga

Professor Robert L. Galloway, Jr.

Professor Thomas E. Yankeelov

Professor Benoit M. Dawant

Professor Mark C. Kelley

ACKNOWLEDGEMENTS

I find myself afforded a quintessential opportunity to reflect upon the last few years and remind myself of all the wonderful help I have received.

Thanks first goes to Dr. Miga for being my advisor over the course of this research and helping to greatly expand my knowledge base and intellectual perspective. Through all the ups and downs, his steady assurance that the work would take care of itself has been the hallmark of his guidance in getting me to this point. It has always been my hope that the success of this work would make his investment worthwhile, and I welcome his continued support.

Thanks to Dr. Galloway for his assistance and generosity over the years. I can honestly say that my decision to come to Vanderbilt was shaped by the impression he left on me seven years ago. It is gratifying to have gained and developed his trust in me, especially in developing technology resources for the laboratory. And of course, to be able to revel in those Dukie moments is a uniquely irreplaceable experience. Go to hell, Carolina!

Thanks to Dr. Yankeelov for igniting a sparkplug for me in the last two years that broadened my horizons on approaching research and being an extra sounding board for ideas and issues. His patience and encouragement that I not be my own worst enemy were invaluable.

Thanks to Dr. Dawant for influencing my way of thinking, perhaps quite much more than he realized, through his class and other informative conversations. His presentations of image processing concepts in no small way have served to consolidate my understanding of the field.

Thanks to Dr. Kelley for agreeing to be a part of my committee. While the core aspects of this project are by nature quite technical, his presence alone is a statement of validation and confidence that the future development of this nascent but novel work is indeed of clinical relevance.

Thanks to my colleagues and peers of the BML and SNARL, past and present, with whom I am honored to have shared time and energy in the pursuit of academic achievement and the occasional camaraderie. To fully list these acclamations would require another document, but those who know the part they played also are always assured of my sincerity. It has been a privilege to work alongside all of you and a thrill in the moments knowing I made a contributory positive impact. For every discussion, for every thing learned each day, it made the lab worthwhile. This is my time to say in turn to those before and after me, with no trace of maudlin sentimentality or irony, "you have touched me", and that I am grateful.

Thanks to my colleagues and friends outside of the lab and even at other institutions who shared ideas and stories over the years that have kept all involved entertained and sane.

Thanks to the MSTP, ASEE, Whitaker Foundation, and the CDMRP/DoD in their generous funding of my work. The recognition by these various agencies for the continuation of this research is a great compliment.

Thanks also to the wonderful support staff of this institution, especially the University machine shop and VUH CT Technologist teams, for their willingness to share their time and expertise.

And finally, I am most thankful for my family, who are the best part—and whole—of who I am as a person. Their unwavering support, appropriately admonishing reminders of reality, and unconditional love is the essence of everything worthwhile. To my parents and sister, for everything they have done, no more words can adequately express the depth of what I feel, always and forever; I dedicate this work to them.

TABLE OF CONTENTS

LIST OF FIGURES

LIST OF TABLES

CHAPTER I

INTRODUCTION

Early detection of masses within the breast that may transform into malignancies is known to be essential for positive treatment and outcome. The use of palpation in the physical exam is a widely accepted clinical practice for correlating relative stiffness with tissue health, and the advent of medical imaging has added a great amount of diagnostically relevant information to the screening process. Recent research has demonstrated that the field of elastography provides an alternative means of interrogating soft tissue structures by creating a spatial mapping of material properties (e.g. elasticity) that can be inspected for the detection and assessment of lesions. In particular, a novel inverse problem technique known as 'modality-independent elastography' (MIE) has been developed in the course of this work and holds much promise in combining the intuitive discrimination from manual detection with the superior depth of penetration and anatomical detail typically given by imaging.

Breast Cancer: Overview

Breast cancer is the most common cancer of women in the United States, the second most common cause of cancer death in women, and the leading cause of death in women ages 45 to 55. Estimates for the year 2007

indicate that 178,480 American women will be diagnosed with the disease and 40,910 women will die from it [1]. Worldwide, more than 700,000 women die of breast cancer annually, and it is estimated that eight to twelve percent of women will develop breast cancer in their lifetime [2, 3]. A number of risk factors and causative agents have been implicated in the development of the disease; these can be grouped by genetics (mutations in BRCA-1, BRCA-2, p53) [4-6], hormonal influences (early menarche, late menopause, exogenous estrogen) [7-11], and environment (socioeconomic status, obesity) [12, 13].

An entire spectrum of neoplasms may arise within the adult human female breast from its various constituents, including epithelial, mesenchymal, and adipose cells. The majority of breast cancers are carcinomas, which arise from the epithelium of breast ducts and lobules, allowing for histologic classification of ductal or lobular carcinomas as *in situ* or invasive [14]. The staging of breast carcinomas can range from stage 0 (*in situ*) to stage IV (distant metastases), with 5-year survival rates dropping from >90% for stage 0 disease to as low as 20% for stage IV [1]. Current guidelines for the treatment of breast cancer have led to improved disease-free survival and quality of life, but early detection remains of paramount importance in the effort to decrease the overall mortality of patients with this disease. The past decade or so has seen annual mortality rates drop by approximately 2.3% per year, and this decline can be attributed, in part, to improved and aggressive interventions resulting from more vigilant screening that allows for detection of the disease in its earlier stages [15-18]. Though histologic examination of tissue is a

necessary element of staging breast cancer, the collection of these tissues (i.e. biopsy) hinges upon on the ability of current radiographic methods to reliably locate lesions. Therefore, there is a critical need for continued developments in clinical imaging to enhance our ability to detect and characterize breast lesions.

Breast cancer detection and screening

The two primary forms of screening and detection performed on a nearly routine basis are the physical examination, either by self-exam or by a physician, and X-ray mammography. The physical examination is performed by careful palpation of the breast tissue and associated lymphatic structures, moving from the axilla to the midline. Mammography involves compressing the breast firmly between a plate and an X-ray cassette containing film (physical or digital) that records a projection image of the tissue. It is now considered to be a clinical standard because the majority of breast cancers are associated with abnormal findings in its interpretation [19, 20]. Although generally accepted to have had a significant role in recent statistics on earlier detection and consequent mortality reduction, the specificity and sensitivity of mammographic assessment is still of some debate. Issues range from the difficulty in studying the various age groups and breast characteristics in populations to the perception of overly broad interpretations provided in BI-RADS (the Breast Imaging Reporting and Data System) classification [21-27].

Despite the dominance of mammography usage, palpation still plays an important part in a proper evaluation. One study of women in their 50s found that careful clinical breast examination alone, when compared with evaluation by both physical examination and mammography, showed no difference in impacting the cancer mortality rate in 13 years of follow-up [28],[29]. A review of controlled trials and case-control studies estimated that the clinical breast examination had about 54% sensitivity and 94% specificity [30] but concluded that there was sufficient indirect evidence to support its use for breast cancer screening. The National Breast and Cervical Cancer Early Detection Program also found that palpation detected about 5-10% percent of cancers that were not visible to mammography [31]. Finally, the National Cancer Institute's recommendations currently note that both mammography and clinical examination have effectiveness in reducing breast cancer mortality [27]. Only the self-exam has become more widely acknowledged as having little or no benefit due to difficulties in teaching and performing proper technique [30],[32], though the primary motivation for women to seek further evaluation still comes from awareness of changes within their breasts.

Beyond the relatively established practices of the physical exam and mammography, there is rapidly growing interest in developing and utilizing other methods of breast cancer detection and screening, particularly those involving imaging. Ultrasound examination of the breast is becoming an important adjunct technique used to differentiate between solid and cystic masses that have been detected and to provide guidance in interventional

procedures. The clinical benefit of ultrasound has been reported to be a reduction in false positive assessments by mammography and palpation [33, 34], as well as the ability to characterize solid masses as benign or malignant. However, the variability of operators in performing a consistent exam and contrasting findings of specificity [35-37] have led to a consensus that despite a high negative predictive value in follow-up evaluations, ultrasound is not yet well-developed enough to be considered a screening tool [38]. Attention has also been given to exploring the use of magnetic resonance (MR) imaging for breast cancer detection. It has been found that the majority of invasive breast carcinomas enhance with gadolinium contrast [39-41], with some clinical evidence indicating that it may have a role in evaluating women with dense breast tissue and detecting occult cancers not found by any other method [42]. Recently, the use of MR has been advocated as a screening test for high-risk women [43, 44]. In one prospective study, researchers found that MR detection outperformed mammography [41], while others have determined that a wide range of specificities (37% to 97%) exist in the test [45]. As with ultrasound, the impact of MR screening is as of yet undetermined but evolving.

Elasticity Imaging in Breast Cancer

Given the current status of available detection and screening techniques and various imaging modalities for breast cancer, there is merit to an active investigation of alternative methods for breast tissue examination. The desire to find other disease indicators has led to research in novel techniques which

attempt to analyze inherent properties of tissue that can be discovered through stimulation from various applied energy sources ranging from electromagnetic [46-51] (e.g. electrical impedance tomography and near-infrared tomography) to mechanical (i.e. elastography).

The physical examination and medical imaging achieve their clinical value because fundamentally, cancer is a non-physiologic proliferation of tissue that often manifests as palpable and/or visible morphological abnormalities. Evidence suggests that elastic properties may differ by at least an order of magnitude within soft tissues between various physiological and pathological states [52-54]. A number of classic characteristics of a suspicious lesion found on physical examination have been described in the clinical literature, including solitary occurrence, a hard "marble-like" feel, relative immobility, irregular borders, and a size greater than or equal to 2 cm in diameter [55]. This reasoning forwarded research to extend the range and sensitivity of palpation with imaging, thereby combining the relative strengths of each method. Studies of the late 1980s using ultrasound [56-60] noted distinct changes in images of tissues in response to mechanical excitation. These observations and others led to the development of a set of methods known as elastography, with seminal papers of this field often identified as those presented by Ophir, *et al* in 1991 [65] using ultrasound and Muthupillai, *et al* in 1995 [66] with MR. Elastography methods are highly varied but largely follow a common strategy: assuming that a tissue follows understood physical principles of mechanical behavior, apply a stress to the tissue, obtain measurements of

internal displacements, and translate those displacements into elasticity values. Deformation can be applied using any number of static (e.g. step compression), dynamic (e.g. harmonic shear waves), or transient sources (e.g. acoustic radiation force) [61, 66-71]. Imaging is preponderantly accomplished through ultrasound and MR for the purpose of making displacement measurements in the tissue by capitalizing on phase sensitivity properties of the modalities. Motion estimates can be obtained by speckle tracking, Doppler effects, and cross-correlation of ultrasound signals [72, 73], while MR techniques utilize motion-sensitive gradient encoding schemes [64, 74-76]. The creation of the final elasticity mapping involves reconstruction of variations in tissue response using direct (strain imaging) or indirect methods (inverse elasticity problem). Strain images (often referred to as 'elastograms') are formed by a derivative operation on the displacement estimations, thereby indicating the presence of hard inclusions by a region of lower strain surrounded by stress concentration effects reminiscent of ultrasound enhancement artifacts occurring behind a cyst. In contrast, the inverse elasticity problem requires a computational model with boundary conditions in order to spatially assign modulus values and reconstruct an elasticity image of the domain [77-79].

While the use of elastography has been employed in other organ systems, the breast is of particular interest because of its relatively non-invasive anatomic access and the intuitive concept of associating disease state with tissue elasticity. Preliminary work in breast elastography in the late 1990s

found that ultrasound-based methods could distinguish solid tumors from their surroundings, and one group suggested that their method could correctly classify most benign and malignant masses [80-84]. A review of clinical usage of various ultrasound elastography techniques to date finds enthusiasm for further study and encouraging data for its ability to detect a lesion. Current evidence places most cancer discrimination sensitivities and specificities at approximately 70% and 90%, respectively [85-91], which is essentially equivalent to standard direct ultrasonic examination. With MR-based elastography methods, similar findings are available that show promise in detecting breast cancers confirmed by physical examination and/or mammography. The most recent clinical trials [92-99] have generally been performed on small groups of patients for procedural validation studies, but their results qualitatively agree with those obtained by ultrasound elastography research groups. Although it is difficult to evaluate the performance of elastography methods as a whole due to the wide spectrum of implementations and enhancements from each investigating group, virtually all characterizations of breast cancer show that disease often corresponds with higher stiffness values compared with normal tissue, and in most cases, malignancy of growth is associated with the stiffest mechanical behavior. It should be noted that there appears to be an overlap of elasticity value ranges which may ultimately be a confounding factor in the differentiation of soft malignant tumors and stiff benign lesions, but the available data collectively suggests that there is a

clinical role for elastography methods in identifying and/or discriminating breast lesions.

Modality Independent Elastography

Because the aforementioned approaches to elastography rely heavily on the accuracy of estimated displacements, many researchers have focused on attempts to enhance a particular imaging modality through alternative hardware and specialized post-processing. In response to this perceived dependence on acquisition technique, Miga [100] proposed a generalized framework of image analysis of an inverse elasticity problem utilizing an intensity-based intramodal non-rigid image registration guided by a finite element model of tissue mechanics. By assuming sufficiency of image heterogeneity provided by inherent anatomical variation, any standard diagnostic image set of a tissue in two different states of mechanical loading as obtained from the major modalities is therefore theoretically suitable for analysis. Washington and Miga [101] followed this work to further codify the paradigm by demonstrating an implementation with a two-dimensional approximation of deformation processes and the use of standard image similarity metrics on image data from X-ray computed tomography (CT) and MR, thereby coining the term 'modality independent elastography' (MIE).

Specific Aims

The ideal elastography method would be accurate in identifying the presence of a lesion (or lesions) both in spatial position and extent, quantifying material properties, and making a specific and sensitive clinical judgment comparable to direct histologic assessment. Because the simultaneous fulfillment of these qualities poses a significant challenge in the development of any such method, it is necessary to explore the capabilities of MIE and address the practical issues of feasibility for breast tumor detection and screening. Therefore, the hypothesis of the proposed work was that testing and development of the MIE methodology will characterize this novel approach to elastography with respect to its clinical potential in breast lesion identification. This was investigated through the following specific aims:

Specific Aim 1: *To provide proof-of-concept characterization of the MIE framework*

- Apply the method using a two-dimensional approximation to a thin membrane phantom testing platform.
- Demonstrate the ability of the method to detect multiple inclusions and utilize image data from various modalities.
- Examine the sensitivity of the method to input quality in order to establish guidelines for appropriate data collection and processing.

Specific Aim 2: *To expand and enhance the MIE framework*

- Design and create an implementation of the method capable of handling fully three-dimensional data.
- Develop strategies for enhancing computational performance and pre-processing task efficiency through *in silico* studies.

Specific Aim 3: *To assess the clinical feasibility of the MIE framework*

- Construct and test a data acquisition system suited to the MIE implementation.
- Demonstrate detection of material inhomogeneity in a breast-mimicking phantom.
- Study practicality of clinical system deployment.

References

[1] ACS, "Cancer Facts and Figures," American Cancer Society, Atlanta 2007.

[2] S. Heywang-Kobrunner, D. Dershaw, and I. Schreer, *Diagnostic Breast Imaging: Mammography, Sonography, Magnetic Resonance Imaging, and Interventional Procedures*. Stuttgart (Germany): Thieme Medical, 2001.

[3] B. E. Henderson and L. Bernstein, "The international variation in breast cancer rates: an epidemiological assessment," *Breast Cancer Res Treat,* vol. 18 Suppl 1, pp. S11-7, May 1991.

[4] J. Peto and T. M. Mack, "High constant incidence in twins and other relatives of women with breast cancer," *Nat Genet,* vol. 26, pp. 411-4, Dec 2000.

[5] P. Lichtenstein, N. V. Holm, P. K. Verkasalo, A. Iliadou, J. Kaprio, M. Koskenvuo, E. Pukkala, A. Skytthe, and K. Hemminki, "Environmental and heritable factors in the causation of cancer--analyses of cohorts of twins from Sweden, Denmark, and Finland," *N Engl J Med,* vol. 343, pp. 78-85, Jul 13 2000.

[6] A. S. Hamilton and T. M. Mack, "Puberty and genetic susceptibility to breast cancer in a case-control study in twins," *N Engl J Med,* vol. 348, pp. 2313-22, Jun 5 2003.

[7] J. L. Kelsey, M. D. Gammon, and E. M. John, "Reproductive factors and breast cancer," *Epidemiol Rev,* vol. 15, pp. 36-47, 1993.

[8] M. Clemons and P. Goss, "Estrogen and the risk of breast cancer," *N Engl J Med,* vol. 344, pp. 276-85, Jan 25 2001.

[9] M. C. Pike, D. V. Spicer, L. Dahmoush, and M. F. Press, "Estrogens, progestogens, normal breast cell proliferation, and breast cancer risk," *Epidemiol Rev,* vol. 15, pp. 17-35, 1993.

[10] J. L. Kelsey, D. B. Fischer, T. R. Holford, V. A. LiVoisi, E. D. Mostow, I. S. Goldenberg, and C. White, "Exogenous estrogens and other factors in the epidemiology of breast cancer," *J Natl Cancer Inst,* vol. 67, pp. 327-33, Aug 1981.

[11] B. MacMahon, D. Trichopoulos, J. Brown, A. P. Andersen, P. Cole, F. deWaard, T. Kauraniemi, A. Polychronopoulou, B. Ravnihar, N. Stormby, and K. Westlund, "Age at menarche, urine estrogens and breast cancer risk," *Int J Cancer,* vol. 30, pp. 427-31, Oct 15 1982.

[12] W. C. Willett, B. Rockhill, S. E. Hankinson, D. J. Hunter, and G. A. Colditz, "Epidemiology and nongenetic causes of breast cancer," in *Diseases of the Breast*, J. Harris, Lippman, ME, Morrow, M, Osborne, CK Ed. Philadelphia: Lippincott, Williams and Wilkins, 2000.

[13] C. J. Bradley, C. W. Given, and C. Roberts, "Race, socioeconomic status, and breast cancer treatment and survival," *J Natl Cancer Inst,* vol. 94, pp. 490-6, Apr 3 2002.

[14] V. Kumar, N. Fausto, and A. Abbas, *Robbins and Cotran Pathologic Basis of Disease*, 7th ed.: Saunders, 2004.

[15] B. K. Edwards, M. L. Brown, P. A. Wingo, H. L. Howe, E. Ward, L. A. Ries, D. Schrag, P. M. Jamison, A. Jemal, X. C. Wu, C. Friedman, L. Harlan, J. Warren, R. N. Anderson, and L. W. Pickle, "Annual report to the nation on the status of cancer, 1975-2002, featuring population-based trends in cancer treatment," *J Natl Cancer Inst,* vol. 97, pp. 1407-27, Oct 5 2005.

[16] K. C. Chu, R. E. Tarone, L. G. Kessler, L. A. Ries, B. F. Hankey, B. A. Miller, and B. K. Edwards, "Recent trends in U.S. breast cancer incidence, survival, and mortality rates," *J Natl Cancer Inst,* vol. 88, pp. 1571-9, Nov 6 1996.

[17] D. A. Berry, K. A. Cronin, S. K. Plevritis, D. G. Fryback, L. Clarke, M. Zelen, J. S. Mandelblatt, A. Y. Yakovlev, J. D. Habbema, and E. J. Feuer, "Effect of screening and adjuvant therapy on mortality from breast cancer," *N Engl J Med,* vol. 353, pp. 1784-92, Oct 27 2005.

[18] "SEER cancer statistics review, 1973-1995," National Cancer Institute, Bethesda 1998.

[19] C. R. Smart, W. H. Hartmann, O. H. Beahrs, and L. Garfinkel, "Insights into breast cancer screening of younger women. Evidence from the 14-year follow-up of the Breast Cancer Detection Demonstration Project," *Cancer,* vol. 72, pp. 1449-56, Aug 15 1993.

[20] P. C. Stomper, W. J.S., G. Proulx, T. Hurd, and S. Edge, "Mammographic detection and staging of ductal carcinoma in situ: mammographic-pathologic correlation," *Seminars in Breast Disease,* vol. 3, pp. 26-41, 2000.

[21] P. C. Gotzsche and O. Olsen, "Is screening for breast cancer with mammography justifiable?," *Lancet,* vol. 355, pp. 129-34, Jan 8 2000.

[22] O. Olsen and P. C. Gotzsche, "Cochrane review on screening for breast cancer with mammography," *Lancet,* vol. 358, pp. 1340-2, Oct 20 2001.

[23] L. Nystrom, I. Andersson, N. Bjurstam, J. Frisell, B. Nordenskjold, and L. E. Rutqvist, "Long-term effects of mammography screening: updated overview of the Swedish randomised trials," *Lancet,* vol. 359, pp. 909-19, Mar 16 2002.

[24] N. Bjurstam, L. Bjorneld, J. Warwick, E. Sala, S. W. Duffy, L. Nystrom, N. Walker, E. Cahlin, O. Eriksson, L. O. Hafstrom, H. Lingaas, J. Mattsson, S. Persson, C. M. Rudenstam, H. Salander, J. Save-Soderbergh, and T. Wahlin, "The Gothenburg Breast Screening Trial," *Cancer,* vol. 97, pp. 2387-96, May 15 2003.

[25] D. A. Freedman, D. B. Petitti, and J. M. Robins, "On the efficacy of screening for breast cancer," *Int J Epidemiol,* vol. 33, pp. 43-55, Feb 2004.

[26] L. L. Humphrey, M. Helfand, B. K. Chan, and S. H. Woolf, "Breast cancer screening: a summary of the evidence for the U.S. Preventive Services Task Force," *Ann Intern Med,* vol. 137, pp. 347-60, Sep 3 2002.

[27] "National Cancer Institute. Breast Cancer PDQ: Screening," 2006.

[28] A. B. Miller, C. J. Baines, T. To, and C. Wall, "Canadian National Breast Screening Study: 2. Breast cancer detection and death rates among women aged 50 to 59 years," *Cmaj,* vol. 147, pp. 1477-88, Nov 15 1992.

[29] A. B. Miller, T. To, C. J. Baines, and C. Wall, "Canadian National Breast Screening Study-2: 13-year results of a randomized trial in women aged 50-59 years," *J Natl Cancer Inst,* vol. 92, pp. 1490-9, Sep 20 2000.

[30] M. B. Barton, R. Harris, and S. W. Fletcher, "The rational clinical examination. Does this patient have breast cancer? The screening clinical breast examination: should it be done? How?," *Jama,* vol. 282, pp. 1270-80, Oct 6 1999.

[31] J. K. Bobo, N. C. Lee, and S. F. Thames, "Findings from 752,081 clinical breast examinations reported to a national screening program from 1995 through 1998," *J Natl Cancer Inst,* vol. 92, pp. 971-6, Jun 21 2000.

[32] J. P. Kosters and P. C. Gotzsche, "Regular self-examination or clinical examination for early detection of breast cancer," *Cochrane Database Syst Rev,* p. CD003373, 2003.

[33] K. Flobbe, A. M. Bosch, A. G. Kessels, G. L. Beets, P. J. Nelemans, M. F. von Meyenfeldt, and J. M. van Engelshoven, "The additional diagnostic value of ultrasonography in the diagnosis of breast cancer," *Arch Intern Med,* vol. 163, pp. 1194-9, May 26 2003.

[34] E. A. Sickles, R. A. Filly, and P. W. Callen, "Benign breast lesions: ultrasound detection and diagnosis," *Radiology,* vol. 151, pp. 467-70, May 1984.

[35] W. A. Berg, L. Gutierrez, M. S. NessAiver, W. B. Carter, M. Bhargavan, R. S. Lewis, and O. B. Ioffe, "Diagnostic accuracy of mammography, clinical examination, US, and MR imaging in preoperative assessment of breast cancer," *Radiology,* vol. 233, pp. 830-49, Dec 2004.

[36] J. A. Baker, P. J. Kornguth, M. S. Soo, R. Walsh, and P. Mengoni, "Sonography of solid breast lesions: observer variability of lesion description and assessment," *AJR Am J Roentgenol,* vol. 172, pp. 1621-5, Jun 1999.

[37] G. Rahbar, A. C. Sie, G. C. Hansen, J. S. Prince, M. L. Melany, H. E. Reynolds, V. P. Jackson, J. W. Sayre, and L. W. Bassett, "Benign versus malignant solid breast masses: US differentiation," *Radiology,* vol. 213, pp. 889-94, Dec 1999.

[38] W. Teh and A. R. Wilson, "The role of ultrasound in breast cancer screening. A consensus statement by the European Group for Breast Cancer Screening," *Eur J Cancer,* vol. 34, pp. 449-50, Mar 1998.

[39] S. G. Orel, M. D. Schnall, V. A. LiVolsi, and R. H. Troupin, "Suspicious breast lesions: MR imaging with radiologic-pathologic correlation," *Radiology,* vol. 190, pp. 485-93, Feb 1994.

[40] W. B. Pierce, S. E. Harms, D. P. Flamig, R. H. Griffey, W. P. Evans, and J. E. Hagans, "Three-dimensional gadolinium-enhanced MR imaging of the breast: pulse sequence with fat suppression and magnetization transfer contrast. Work in progress," *Radiology,* vol. 181, pp. 757-63, Dec 1991.

[41] D. A. Bluemke, C. A. Gatsonis, M. H. Chen, G. A. DeAngelis, N. DeBruhl, S. Harms, S. H. Heywang-Kobrunner, N. Hylton, C. K. Kuhl, C. Lehman, E. D. Pisano, P. Causer, S. J. Schnitt, S. F. Smazal, C. B. Stelling, P. T. Weatherall, and M. D. Schnall, "Magnetic resonance imaging of the breast prior to biopsy," *Jama,* vol. 292, pp. 2735-42, Dec 8 2004.

[42] L. Esserman, N. Hylton, L. Yassa, J. Barclay, S. Frankel, and E. Sickles, "Utility of magnetic resonance imaging in the management of breast

cancer: evidence for improved preoperative staging," *J Clin Oncol,* vol. 17, pp. 110-9, Jan 1999.

[43] M. Kriege, C. T. Brekelmans, C. Boetes, P. E. Besnard, H. M. Zonderland, I. M. Obdeijn, R. A. Manoliu, T. Kok, H. Peterse, M. M. Tilanus-Linthorst, S. H. Muller, S. Meijer, J. C. Oosterwijk, L. V. Beex, R. A. Tollenaar, H. J. de Koning, E. J. Rutgers, and J. G. Klijn, "Efficacy of MRI and mammography for breast-cancer screening in women with a familial or genetic predisposition," *N Engl J Med,* vol. 351, pp. 427-37, Jul 29 2004.

[44] C. K. Kuhl, S. Schrading, C. C. Leutner, N. Morakkabati-Spitz, E. Wardelmann, R. Fimmers, W. Kuhn, and H. H. Schild, "Mammography, breast ultrasound, and magnetic resonance imaging for surveillance of women at high familial risk for breast cancer," *J Clin Oncol,* vol. 23, pp. 8469-76, Nov 20 2005.

[45] M. Morrow, "Magnetic resonance imaging in breast cancer: one step forward, two steps back?," *Jama,* vol. 292, pp. 2779-80, Dec 8 2004.

[46] V. Cherepenin, A. Karpov, A. Korjenevsky, V. Kornienko, A. Mazaletskaya, D. Mazourov, and D. Meister, "A 3Delectrical impedance tomography (EIT) system for breast cancer detection," *Physiological Meas.,* vol. 22, pp. 9-18, 2001.

[47] S. Scott and M. Morrow, "Breast cancer. Making the diagnosis," *Surg Clin North Am,* vol. 79, pp. 991-1005, Oct 1999.

[48] K. S. Osterman, T. E. Kerner, D. B. Williams, A. Hartov, S. P. Poplack, and K. D. Paulsen, "Multifrequency electrical impedance imaging: preliminary in vivo experience in breast," *Physiol Meas,* vol. 21, pp. 99-109, Feb 2000.

[49] B. W. Pogue, C. Willscher, T. O. McBride, U. L. Osterberg, and K. D. Paulsen, "Contrast-detail analysis for detection and characterization with near-infrared diffuse tomography," *Med Phys,* vol. 27, pp. 2693-700, Dec 2000.

[50] Q. Zhu, E. Conant, and B. Chance, "Optical imaging as an adjunct to sonograph in differentiating benign from malignant breast lesions," *J.Biomed Opt.,* vol. 5, pp. 229–236, 2000.

[51] S. B. Colak, M. B. van der Mark, G. W. Hooft, J. H. Hoogenraad, E. S. van der Linden, and F. A. Kuijpers, "Clinical optical tomography and NIR spectroscopy for breast cancer detection," *Ieee Journal of Selected Topics in Quantum Electronics,* vol. 5, pp. 1143-1158, Jul-Aug 1999.

[52] P. M. Meaney, M. W. Fanning, D. Li, S. P. Poplack, and K. D. Paulsen, "A clinical prototype for active microwave imaging of the breast," *Ieee Transactions on Microwave Theory and Techniques,* vol. 48, pp. 1841-1853, Nov 2000.

[53] T. Takenaka, H. Jia, and T. Tanaka, "Microwave imaging of electrical property distributions by a forward-backward time-stepping method," *Journal of Electromagnetic Waves and Applications,* vol. 14, pp. 1609-1626, 2000.

[54] J. B. Fowlkes, S. Y. Emelianov, J. G. Pipe, A. R. Skovoroda, P. L. Carson, R. S. Adler, and A. P. Sarvazyan, "Magnetic-resonance imaging techniques for detection of elasticity variation," *Med Phys,* vol. 22, pp. 1771-8, Nov 1995.

[55] A. P. Sarvazyan, A. R. Skovoroda, S. Y. Emelianov, J. B. Fowlkes, J. G. Pipe, R. S. Adler, R. B. Buxton, and P. L. Carson, "Biophysical bases for elasticity imaging," in *Acoustical Imaging*. vol. 21, J. P. Jones, Ed. New York: Plenum Press, 1995, pp. 223–40.

[56] Y. Fung, *Biomechanics: Mechanical Properties of Living Tissues*. New York: Springer-Verlag, 1993.

[57] L. Venet, P. Strax, W. Venet, and S. Shapiro, "Adequacies and inadequacies of breast examinations by physicians in mass screening," *Cancer,* vol. 28, pp. 1546-51, Dec 1971.

[58] M. Tristam, D. C. Barbosa, D. O. Cosgrove, J. C. Bamber, and C. R. Hill, "Application of Fourier analysis to clinical study of patterns of tissue movement," *Ultrasound Med Biol,* vol. 14, pp. 695-707, 1988.

[59] E. Ueno, E. Tohno, S. Soeda, Y. Asaoka, K. Itoh, J. C. Bamber, M. Blaszczyk, J. Davey, and J. A. McKinna, "Dynamic tests in real-time breast echography," *Ultrasound Med Biol,* vol. 14 Suppl 1, pp. 53-7, 1988.

[60] J. C. Bamber, L. De Gonzalez, D. O. Cosgrove, P. Simmons, J. Davey, and J. A. McKinna, "Quantitative evaluation of real-time ultrasound features of the breast," *Ultrasound Med Biol,* vol. 14 Suppl 1, pp. 81-7, 1988.

[61] J. Ophir, I. Cespedes, H. Ponnekanti, Y. Yazdi, and X. Li, "Elastography: a quantitative method for imaging the elasticity of biological tissues," *Ultrason Imaging,* vol. 13, pp. 111-34, Apr 1991.

[62] S. F. Levinson, "Ultrasound propagation in anisotropic soft tissues: the application of linear elastic theory," *J Biomech,* vol. 20, pp. 251-60, 1987.

[63] S. F. Levinson and V. L. Newhouse, "The Phase Response of Ultrasound to Vibration - a Method of Measuring Tissue Elasticity," *Ultrasonic Imaging,* vol. 10, pp. 74-75, Jan 1988.

[64] L. Axel and L. Dougherty, "Heart wall motion: improved method of spatial modulation of magnetization for MR imaging," *Radiology,* vol. 172, pp. 349-50, Aug 1989.

[65] E. A. Zerhouni, D. M. Parish, W. J. Rogers, A. Yang, and E. P. Shapiro, "Human heart: tagging with MR imaging--a method for noninvasive assessment of myocardial motion," *Radiology,* vol. 169, pp. 59-63, Oct 1988.

[66] R. Muthupillai, D. J. Lomas, P. J. Rossman, J. F. Greenleaf, A. Manduca, and R. L. Ehman, "Magnetic resonance elastography by direct visualization of propagating acoustic strain waves," *Science,* vol. 269, pp. 1854-7, Sep 29 1995.

[67] K. J. Parker, D. Fu, S. M. Gracewski, F. Yeung, and S. F. Levinson, "Vibration sonoleastography and the detectability of lesions," *Ultrasound Med. Biol.,* pp. 1937–1947, 1998.

[68] L. Gao, K. J. Parker, S. K. Alam, and R. M. Lernel, "Sonoelasticity imaging: theory and experimental verification," *J Acoust Soc Am,* vol. 97, pp. 3875-86, Jun 1995.

[69] K. R. Nightingale, R. W. Nightingale, M. L. Palmeri, and G. E. Trahey, "A finite element model of remote palpation of breast lesions using radiation force: factors affecting tissue displacement," *Ultrason Imaging,* vol. 22, pp. 35-54, Jan 2000.

[70] K. R. Nightingale, M. L. Palmeri, R. W. Nightingale, and G. E. Trahey, "On the feasibility of remote palpation using acoustic radiation force," *J Acoust Soc Am,* vol. 110, pp. 625-34, Jul 2001.

[71] J. Ophir, B. Garra, F. Kallel, E. Konofagou, T. Krouskop, R. Righetti, and T. Varghese, "Elastographic imaging," *Ultrasound Med Biol,* vol. 26 Suppl 1, pp. S23-9, May 2000.

[72] P. Chaturvedi, M. F. Insana, and T. J. Hall, "Ultrasonic and elasticity imaging to model disease-induced changes in soft-tissue structure," *Med Image Anal,* vol. 2, pp. 325-38, Dec 1998.

[73] M. O'Donnell, A. R. Skovoroda, B. M. Shapo, and S. Y. Emelianov, "Internal Displacement and Strain Imaging Using Ultrasonic Speckle Tracking," *Ieee Transactions on Ultrasonics Ferroelectrics and Frequency Control,* vol. 41, pp. 314-325, May 1994.

[74] M. M. Doyley, J. B. Weaver, E. E. Van Houten, F. E. Kennedy, and K. D. Paulsen, "Thresholds for detecting and characterizing focal lesions using steady-state MR elastography," *Med Phys,* vol. 30, pp. 495-504, Apr 2003.

[75] D. B. Plewes, J. Bishop, A. Samani, and J. Sciarretta, "Visualization and quantification of breast cancer biomechanical properties with magnetic resonance elastography," *Phys Med Biol,* vol. 45, pp. 1591-610, Jun 2000.

[76] Y. Kita, "Elastic-model driven analysis of several views of a deformable cylindrical object," *Ieee Transactions on Pattern Analysis and Machine Intelligence,* vol. 18, pp. 1150-1162, Dec 1996.

[77] M. M. Doyley, S. Srinivasan, S. A. Pendergrass, Z. Wu, and J. Ophir, "Comparative evaluation of strain-based and model-based modulus elastography," *Ultrasound Med Biol,* vol. 31, pp. 787-802, Jun 2005.

[78] H. T. Liu, L. Z. Sun, G. Wang, and M. W. Vannier, "Analytic modeling of breast elastography," *Med Phys,* vol. 30, pp. 2340-9, Sep 2003.

[79] I. Cespedes, J. Ophir, H. Ponnekanti, and N. Maklad, "Elastography: elasticity imaging using ultrasound with application to muscle and breast in vivo," *Ultrason Imaging,* vol. 15, pp. 73-88, Apr 1993.

[80] B. S. Garra, E. I. Cespedes, J. Ophir, S. R. Spratt, R. A. Zuurbier, C. M. Magnant, and M. F. Pennanen, "Elastography of breast lesions: initial clinical results," *Radiology,* vol. 202, pp. 79-86, Jan 1997.

[81] C. Sumi, K. Nakayama, and M. Kubota, "An effective ultrasonic strain measurement-based shear modulus reconstruction technique for superficial tissues--demonstration on in vitro pork ribs and in vivo human breast tissues," *Phys Med Biol,* vol. 45, pp. 1511-20, Jun 2000.

[82] T. Krouskop, R. Price, T. Wheeler, and P. Younes, "Modulus variations in breast tissues," in *Proc International Conference of the Ultrasonics Measurements and Imaging of Tissue Elasticity*, Niagara Falls, 2002.

[83] K. M. Hiltawsky, M. Kruger, C. Starke, L. Heuser, H. Ermert, and A. Jensen, "Freehand ultrasound elastography of breast lesions: clinical results," *Ultrasound Med Biol,* vol. 27, pp. 1461-9, Nov 2001.

[84] D. Melodelima, J. C. Bamber, F. A. Duck, J. A. Shipley, and L. Xu, "Elastography for breast cancer diagnosis using radiation force: system development and performance evaluation," *Ultrasound Med Biol,* vol. 32, pp. 387-96, Mar 2006.

[85] W. Khaled, S. Reichling, O. T. Bruhns, and H. Ermert, "Ultrasonic strain imaging and reconstructive elastography for biological tissue," *Ultrasonics,* Jun 30 2006.

[86] A. Thomas, T. Fischer, H. Frey, R. Ohlinger, S. Grunwald, J. U. Blohmer, K. J. Winzer, S. Weber, G. Kristiansen, B. Ebert, and S. Kummel, "Real-time elastography--an advanced method of ultrasound: First results in 108 patients with breast lesions," *Ultrasound Obstet Gynecol,* vol. 28, pp. 335-40, Sep 2006.

[87] A. Itoh, E. Ueno, E. Tohno, H. Kamma, H. Takahashi, T. Shiina, M. Yamakawa, and T. Matsumura, "Breast disease: clinical application of US elastography for diagnosis," *Radiology,* vol. 239, pp. 341-50, May 2006.

[88] G. M. Giuseppetti, A. Martegani, B. Di Cioccio, and S. Baldassarre, "Elastosonography in the diagnosis of the nodular breast lesions: preliminary report," *Radiol Med (Torino),* vol. 110, pp. 69-76, Jul-Aug 2005.

[89] S. A. Kruse, J. A. Smith, A. J. Lawrence, M. A. Dresner, A. Manduca, J. F. Greenleaf, and R. L. Ehman, "Tissue characterization using magnetic resonance elastography: preliminary results," *Physics in Medicine and Biology,* vol. 45, pp. 1579-1590, Jun 2000.

[90] A. Tardivon, C. El Khoury, F. Thibault, A. Wyler, B. Barreau, and S. Neuenschwander, "[Elastography of the breast: a prospective study of 122 lesions]," *J Radiol,* vol. 88, pp. 657-62, May 2007.

[91] H. Zhi, B. Ou, B. M. Luo, X. Feng, Y. L. Wen, and H. Y. Yang, "Comparison of ultrasound elastography, mammography, and sonography in the diagnosis of solid breast lesions," *J Ultrasound Med,* vol. 26, pp. 807-15, Jun 2007.

[92] A. Manduca, T. E. Oliphant, M. A. Dresner, J. L. Mahowald, S. A. Kruse, E. Amromin, J. P. Felmlee, J. F. Greenleaf, and R. L. Ehman, "Magnetic resonance elastography: non-invasive mapping of tissue elasticity," *Med Image Anal,* vol. 5, pp. 237-54, Dec 2001.

[93] P. J. McCracken, A. Manduca, J. Felmlee, and R. L. Ehman, "Mechanical transient-based magnetic resonance elastography," *Magn Reson Med,* vol. 53, pp. 628-39, Mar 2005.

[94] A. L. McKnight, J. L. Kugel, P. J. Rossman, A. Manduca, L. C. Hartmann, and R. L. Ehman, "MR elastography of breast cancer: preliminary results," *AJR Am J Roentgenol,* vol. 178, pp. 1411-7, Jun 2002.

[95] E. E. Van Houten, M. M. Doyley, F. E. Kennedy, J. B. Weaver, and K. D. Paulsen, "Initial in vivo experience with steady-state subzone-based MR elastography of the human breast," *J Magn Reson Imaging,* vol. 17, pp. 72-85, Jan 2003.

[96] T. Xydeas, K. Siegmann, R. Sinkus, U. Krainick-Strobel, S. Miller, and C. D. Claussen, "Magnetic resonance elastography of the breast: correlation of signal intensity data with viscoelastic properties," *Invest Radiol,* vol. 40, pp. 412-20, Jul 2005.

[97] J. Lorenzen, R. Sinkus, M. Lorenzen, M. Dargatz, C. Leussler, P. Roschmann, and G. Adam, "MR elastography of the breast:preliminary clinical results," *Rofo,* vol. 174, pp. 830-4, Jul 2002.

[98] J. Lorenzen, R. Sinkus, D. Schrader, M. Lorenzen, C. Leussler, M. Dargatz, and P. Roschmann, "[Imaging of breast tumors using MR elastography]," *Rofo,* vol. 173, pp. 12-7, Jan 2001.

[99] R. Sinkus, M. Tanter, T. Xydeas, S. Catheline, J. Bercoff, and M. Fink, "Viscoelastic shear properties of in vivo breast lesions measured by MR elastography," *Magn Reson Imaging,* vol. 23, pp. 159-65, Feb 2005.

[100] M. I. Miga, "A new approach to elastography using mutual information and finite elements," *Physics in Medicine and Biology,* vol. 48, pp. 467-480, Feb 21 2003.

[101] C. W. Washington and M. I. Miga, "Modality independent elastography (MIE): a new approach to elasticity imaging," *IEEE Trans Med Imaging,* vol. 23, pp. 1117-28, Sep 2004.

CHAPTER II

MANUSCRIPT 1: MODALITY INDEPENDENT ELASTOGRAPHY (MIE): POTENTIAL APPLICATIONS IN DERMOSCOPY

Michael I. Miga, Megan P. Rothney, and Jao J. Ou

Department of Biomedical Engineering, Vanderbilt University, Nashville, TN 37235

This manuscript has been published in *Medical Physics*, Vol. 32, No. 5, May 2005

Abstract

The use of palpation information for skin disease characterization is not as commonly used as in other soft tissues, although mechanical differences within lesions have been noted. For example, regions of hyperkeratosis have the potential to transform into cancerous lesions and likely feature different material properties from those of surrounding normal tissue due to varying cyto-architecture. As a result, the spatial distribution of lesion mechanical properties may serve to assist diagnosis or enhance visualization of the complete extent of a cancerous region, i.e. accurate information regarding the margins of disease for surgical therapy. In this work, a multi-resolution extension to a novel elastographic imaging method called Modality Independent Elastography (MIE) is used to characterize the mechanical properties of a skin-like phantom embedded with a mock stiff lesion. Simulation studies were also

performed to investigate the potential for characterizing realistic melanoma lesions. Elasticity image reconstructions from the phantom experiments localized the stiff inclusion and had good correlation between the Young's modulus contrast ratio and experimental measurements from material testing. In addition, multi-resolution MIE was shown to be a more robust framework than its single-resolution version. Results from the melanoma simulation demonstrate the potential for using multi-resolution MIE with dermoscopic images.

Introduction

Skin cancers are a growing health concern in the United States, with total annual cases being reported in the millions by the American Cancer Society. There are three major types of skin cancers [basal cell carcinoma (BCC), squamous cell carcinoma (SCC), and melanoma], with melanoma estimated to be the sixth most prevalent cancer and an estimated 55,100 new cases swithin the United Statesd to be diagnosed in 2004 [1]. In general, skin cancers develop from precancerous lesions of the epidermis that have dysplastic changes due to the damage inflicted by ultraviolet solar radiation. As with other cancers, the dysfunctional cells may aggressively compete with normal tissue for nutrients and space. The progression from a benign to malignant state depends upon the degree of cellular differentiation and the spatial extent of the growth, which approximately translates into the pathological determination of grade and stage.

When skin cancers are identified at an early stage and are still small in size, surgical excision is usually straightforward and effective. If the disease has progressed to invade deeper levels of the skin, treatment becomes more difficult and may involve more invasive surgery, radiation, and/or chemotherapy. It is clear that the early detection of cancer is critical in order to formulate a proper treatment plan and achieve the most favorable clinical outcome. However, detection and diagnosis still rely primarily on visual inspection followed by a biopsy of suspect areas for histological analysis. Therefore, a significant proportion of diagnostic technological advances have been concerned with obtaining a better view of the lesion *via* improved optics (i.e., dermoscopy) or more advanced and novel imaging systems ranging from high-frequency ultrasound to confocal laser microscopy [2,3]. Additional strategies involving electrical impedance mismatch [4], Raman spectroscopy [5], and cytological smears [3] have also been forthcoming.

As opposed to other methods mentioned above which capitalize on electrical, optical, and biochemical phenomena, we have chosen to pursue an alternative approach to skin health assessment which is based on its mechanical behavior. Detecting changes in tissue by palpation and then associating them with a disease state has had a longstanding history in clinical medicine. Although a health assessment of skin from palpation is performed to a lesser degree, utilizing changes in the mechanical properties to characterize the skin does have precedent within clinical dermatology. One thoughtful

review by Edwards and Marks discusses the complex mechanical behavior of skin when subjected to *in vitro* and *in vivo* testing [6]. Their review highlights extensive methodologies being used to quantify skin mechanical properties (e.g., uniaxial and biaxial extensometry, torsion stimulators, indentometery, ballistometric tests, shear wave application devices, dynamic suction methods, ultrasonics, and electrodynamometry) and also indicates the difficulties in comparing across these methods. As a result, Edwards and Marks emphasize the necessity for quantitative, reproducible methods to assess skin health given the wide subjectivity in clinical analysis [6]. For example, the work by Draaijers *et al.* suggests that reliable subjective assessment of the pliability of scars requires more than one observer while measurements using a noninvasive suction device can be accomplished with a single observer [7]. This type of work qualitatively confirms the Edwards and Marks conclusion that the need for technology and automation in skin assessment will be essential for reducing inter-rater variability.

While the characterization of skin cancer for diagnostic purposes and possibly surgical intervention is an interesting prospect, other investigations have begun to suggest relationships between skin elasticity parameters and other diseases. In a recent study using a noninvasive suction device, Pierard *et al.* demonstrated a correlation between bone mass density (BMD) and skin elasticity parameters. Specifically, in a 100-woman study in which a portion of the subjects were participating in hormone replacement therapy, a positive correlation existed between BMD of the hip and femoral neck and skin

elasticity parameters. The authors clearly state that their goal was not to develop a surrogate BMD assessment test, but the results are nevertheless intriguing [8,9]. Using a similar device, Yoon *et al.* demonstrated a relationship between skin elasticity parameters and patients afflicted with diabetes mellitus [10]. Other work has been forthcoming [11-16] that demonstrates the potential for using noninvasive measurements of skin mechanical parameters as diagnostic information.

To this end, the field of elastography has established methods to spatially characterize the mechanical properties of tissues under various states of deformation with the goal of developing functional parameters to characterize disease [17, 18]. In skin cancer, increases in cell density, atypia in the morphology and orientation of cells, and compositional alterations (e.g., hyperkeratosis) contribute to changes in the local cytoarchitecture. These changes in mechanical structure can propagate from microscopic to macroscopic levels and may manifest as a distortion of the normal anatomy. Given the influence of mechanical structure on the behavior of deforming tissue, elastographic imaging methods may be well suited for detecting and monitoring the growth of these cancerous anomalies. In fact, advances in applying ultrasound elastography and sonography techniques to skin are being reported [3, 19-22]. Most recently, Gennisson *et al.* demonstrated the use of a new sonoelastographic probe that measured a distinct difference between dermis and hypodermis shear wave velocities which was subsequently used to estimate Young's modulus [22]. Although interesting, this work is not

completely applicable to the clinical goals of understanding the spatial extents of a melanoma lesion.

Following previous work in Ref. 23, we are using a new elastographic method we have termed "modality-independent elastography" (MIE) that combines nonrigid image registration with an elasticity inverse problem. More specifically, image similarity metrics routinely used with image registration methods are recast within a nonlinear optimization algorithm whereby mechanical properties (e.g., Young's modulus) within a biomechanical model of the deforming tissue become the driving parameters for improved image registration. In this way, the MIE method circumvents two potential limitations of current elastographic techniques. First, it is not inherently dependent on preprocessing steps such as homologous feature selection and tracking which drive active contour models [19-21] or other traditional displacement-based iterative methods [24-29] (however, it does require the determination of boundary conditions). Second, because it is an image processing technique, MIE is not reliant on a particular imaging modality such as in ultrasound and magnetic resonance elastography, as long as the acquired images provide a sufficient pattern to allow for registration. Building on recently completed work with a dual-mesh implementation [30], in this paper we present a simplified multiresolution elasticity imaging framework for Young's modulus reconstruction. In addition, phantom and simulation experiments demonstrate its utility as a dermoscopic image analysis tool for evaluating skin lesions based on material elasticity.

As a final point, the work presented here represents a potentially new application of the MIE approach for the characterization of skin lesions using optical images. This may have significant implications at many length scales (subcellular, cellular, matrix level, and gross tissue). For example, properly designed, optically based MIE could be used to characterize the structural development of tissues at the cellular scale. This could be important for therapies such as Mohs micrographic surgery. Mohs is a surgical technique which combines surgery and pathological investigation to more effectively remove skin tumors. More specifically, after removing visibly cancerous regions, the surgeon removes an additional thin layer of the site margin and creates a "map" of the border. Upon pathological examination of the removed layer, the "map" can be used to target the remaining cancerous cells. Currently, the Mohs technique is a time-consuming procedure, but the success of the procedure is compelling and has been shown to be cost effective with certain considerations [39]. If MIE skin imaging could accurately assist or replace the pathologic characterization of the margin in less time, this would be of great value for this surgical therapy.

Methods

Model of Phantom/Skin Elasticity

One critical component within all model-based inverse problem frameworks is the selection of a computational model to represent the

continuum of interest. In our phantom and simulation studies, we have elected to employ a linear elastic model to simulate the skin. These assumptions (e.g., symmetry, isotropy, etc.) allow the simplification of Cauchy's law from 36 stiffness constants to 2 and employ the equation

$$\nabla \cdot \sigma = 0, \tag{1}$$

where σ is the two-dimensional (2-D) Cartesian stress tensor and is defined as

$$\sigma = \begin{bmatrix} \sigma_x & \tau_{xy} \\ \tau_{xy} & \sigma_y \end{bmatrix}. \tag{2}$$

The constitutive relationships for the material can be written as

$$\begin{bmatrix} \sigma_x \\ \sigma_y \\ \tau \end{bmatrix} = \frac{E}{(1-\nu)^2} \begin{bmatrix} 1 & \nu & 0 \\ \nu & 1 & 0 \\ 0 & 0 & \frac{1-\nu}{2} \end{bmatrix} \begin{bmatrix} \frac{\partial u}{\partial x} \\ \frac{\partial v}{\partial y} \\ \frac{\partial u}{\partial y} + \frac{\partial v}{\partial x} \end{bmatrix}, \tag{3}$$

where *E* is the Young's modulus, ν is Poisson's ratio, and υ, *v* are displacements in the *x* and *y* directions, respectively. For this work, Poisson's ratio was assumed to be constant at 0.485 for our skin phantoms and tissue simulations. This value was found by searching the reconstruction parameter space for an optimal value that achieved maximum similarity when comparing the homogeneous model-deformed image to its acquired counterpart. The constitutive relationships expressed in (3) represent a two-dimensional approximation to a three-dimensional system which assumes a symmetric, isotropic, thin specimen in equilibrium and stresses that are constrained to lie

within the plane, i.e. the classic plane stress approximation [31]. Using the Galerkin method of weighted residuals to integrate this set of partial differential equations, a finite element framework is generated and can be solved to represent a displacement field for a given distribution of Young's modulus values [32]. The boundary conditions for our studies below were either manually derived from a structured grid representation as in the phantom system or prescribed by the user in the case of the simulation studies.

Modality-Independent Elastography (MIE)

The MIE framework begins with the acquisition of a baseline pre-deformed "source" image and a post-deformed "target" image. The "source" image set is used to create a well-resolved finite element mesh of the tissue domain. In previous work, a second coarse mesh was also specified on the domain and was used specifically as the mechanical property reconstruction grid [30]. In this work, a new single-mesh region-based multi-resolution MIE approach has been employed which simplifies previous dual-grid techniques with the generation of a structured regionalization using a *K*-means clustering algorithm based on the element centroids of the well-resolved mesh. A *K*-means clustering algorithm iteratively partitions the element centroids into a given number (K) of *regions* (where *K* is the user-defined number of desired clusters) such that the sum of all point-to-*region* centroid distances over all *regions* is minimized. The advantage of using the *K*-means clustering approach as opposed to a regular grid is that the clustering approach can more

appropriately fit irregular domains (e.g. the circular domain for the dermoscopic image set). For this work, the implementation in the MATLAB (MathWorks, Natick, MA—www.mathworks.com) statistics toolbox was used. Figure 1 illustrates an example of this approach on a circular domain whereby the element centroids have been clustered into 16 separate homogeneous, isotropic *regions*.

The method has been adapted to a multiresolution strategy whereby coarser resolutions (i.e., fewer *regions*) can be initially reconstructed to provide better initial guesses to subsequent resolutions. The use of hierarchical multiresolution structures within both rigid and nonrigid registration algorithms has a longstanding precedent and lends credence to its application here [33-35]. In this work, six progressively finer resolutions were used within each reconstruction (16, 36, 64, 144, 256, 400 *regions*).

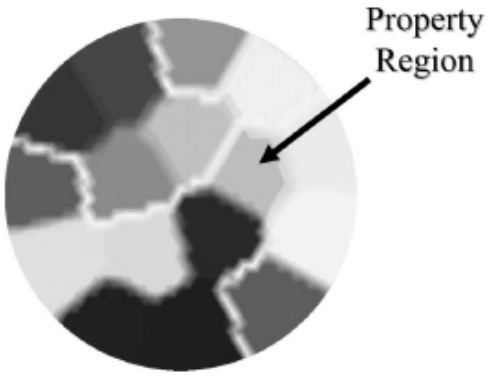

Figure 1. *K*-means material property clustering for a circular domain with 16 property regions designated.

Once the mesh and *K*-means resolutions have been specified, the reconstruction algorithm begins by assigning an initial modulus value to each *region* (a homogeneous initialization is assumed) at the first resolution, weighted residual equations are integrated, boundary conditions are applied, and the matrix equation system is generated:

$$[A(\vec{E}_E)]\{u\} = \{b\}, \tag{4}$$

where $[A(\vec{E}_E)]$ represents the model stiffness matrix based on the current distribution of properties $\vec{E}_E$, {*u*} is the vector of unknown tissue displacements, and {*b*} is the vector of known forces acting on the system and boundary conditions. Upon the calculation of tissue displacements, the source image can be deformed. This model-deformed source image is then compared to the target image using an image similarity method [23,30] which is calculated over a number of discrete spatial *zones* (e.g., for all reconstructions, approximately 400 similarity *zones* were designated within the image for a comparison). Modulus values in the *regions* are updated based on maximizing the similarity between the deformed source image and the target image over all the similarity *zones* until a tolerance is reached or the desired number of iterations has been completed. With respect to the optimization framework for MIE, it can be represented as a least squared error objective function:

$$\phi(\vec{E}) = \min\{\|S(\vec{E}_t) - S(\vec{E}_E)\|^2\}, \tag{5}$$

where $S(\vec{E}_t)$ is the similarity value achieved when comparing the target image to itself (i.e., the maximum value for the similarity metric) and $S(\vec{E}_E)$ is the similarity between the model-deformed source image and the target image using the current estimate of the elastic modulus, $\vec{E}_E$. Equation (5) can be solved by employing a Newton–Raphson-based approach:

$$[[J^T][J] + \alpha[I]]\{\Delta\vec{E}\} = [J^T]\{S(\vec{E}_t) - S(\vec{E}_E)\}, \qquad (6)$$

where [*J*] is the *M x N* Jacobian matrix of the form $J = \partial S(\vec{E}_E)/\partial\vec{E}$, *M* is the number of similarity measurement *zones*, and *N* is the number of material property *regions* and is equivalent to *K* as designated in the *K*-means clustering algorithm. The details of Eq. (6) have been reported previously [23,30]. Because $[J^T][J]$ (an approximation to the Hessian matrix) tends to be ill conditioned, it is regularized with an empirically determined α parameter found in the standard Levenberg–Marquardt approach [36]. The determination of this regularization parameter is described in Ref. 37. Figure 2 is a flow chart of the new multiresolution MIE approach.

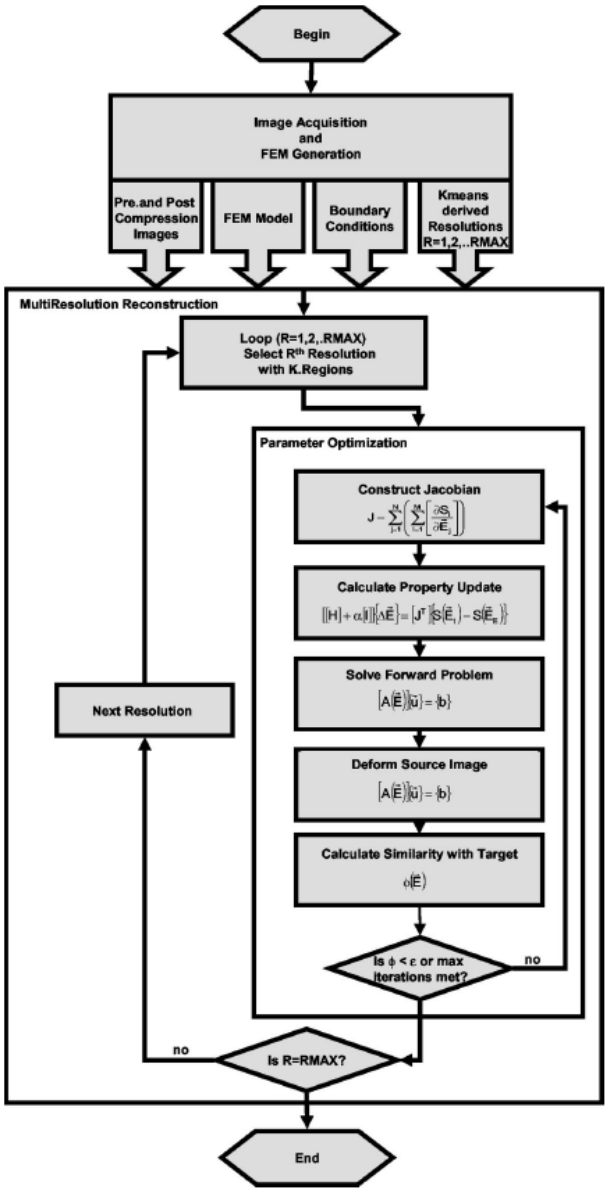

Figure 2. Multiresolution MIE algorithm flow chart where "$R=1,2,3\ldots,R_{MAX}$" is the resolution level with R_{MAX} the most well resolved; and "K" is the number of material regions within a particular resolution "R".

In previous work, we have analyzed the performance of our MIE algorithm with respect to four standard image similarity metrics found within the literature: the sum of squared differences, normalized mutual information,

the correlation coefficient (CC), and the gradient correlation coefficient (GC) [30]. Within this work, the correlation coefficient and gradient correlation coefficient were used for the similarity measurements.

Briefly stated, the CC operates on the distribution and mean intensity values of the overlapping regions of two images where I_1 would represent the intensity values within the "target" image and I_2 would be the model-deformed "source" image. The correlation coefficient can be calculated by the expression

$$CC = \frac{\Sigma_i (I_1(i) - \overline{I_1})(I_2(i) - \overline{I_2})}{\sqrt{\Sigma_i (I_1(i) - \overline{I_1})^2 (I_2(i) - \overline{I_2})^2}}, \quad \forall \in I_1 \cap I_2, \qquad (7)$$

where $\overline{I_1}$, $\overline{I_2}$ are the mean intensity values within each respective image, and *i* is the *i*th pixel within the respective image. The GC metric is calculated by applying the correlation coefficient to images that have been processed by any of the standard edge detection functions (e.g., Canny, Sobel, etc.).

Phantom Construction

A phantom was constructed that was approximately 25 cm long, 15 cm wide, and approximately 2 mm thick. The inclusion-surrounding bulk material of the phantom was Smooth-On™ Evergreen 10 polyurethane with an additive to allow permanent marker to adhere to the material surface (Smooth-On, 2000 Saint John Street, Easton, PA). A cylindrical inclusion was placed centrally within the membrane phantom that was approximately 5 cm in diameter and

was made of a stiffer polyurethane material (Smooth-On™ Evergreen 50). The inclusion material was chosen for its relative stiffness to that of Evergreen 10 and its color which is the same (to study the case of non-pigmented lesions). After the phantoms had set, a permanent marker was used to draw 15 cm x 15 cm grid with 1 cm x 1 cm squares on the phantom surface. Figure 3(a) shows the skin phantom used for data collection in this series of experiments.

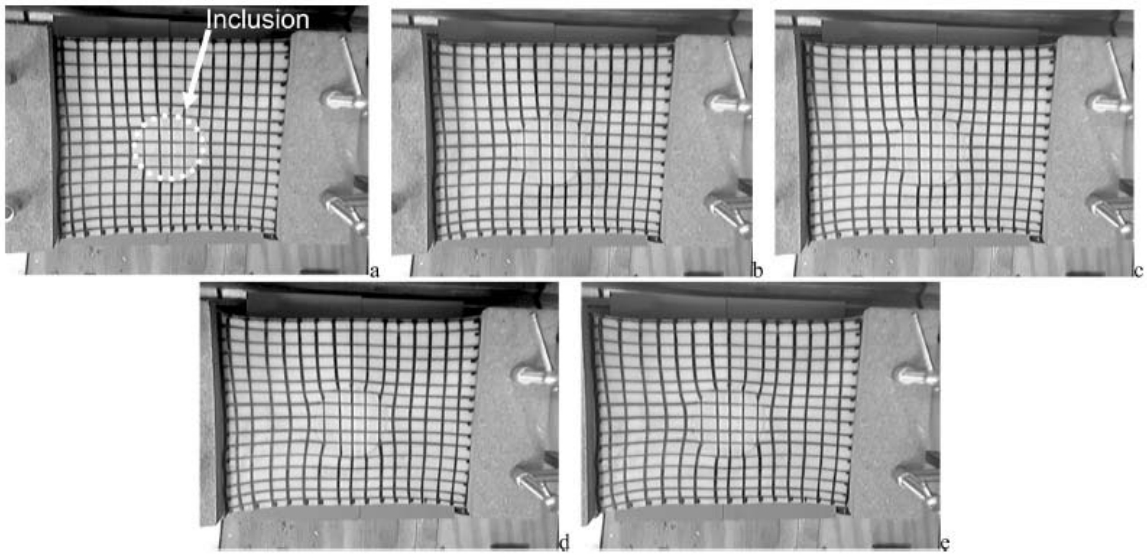

Figure 3. Experimental data from the skin-stretching setup shown in Fig. 4: (a) baseline, (b) 5 mm, (c) 10 mm, (d) 15 mm, (e) 20 mm.

Image Acquisition Protocol

To acquire the pre- and post-deformed images of the stretched skin phantom, the membrane was first secured in customized clamps attached to a milling vise to form a translation stage and then brought level with a nominal applied load to define the baseline position. Images were taken by a commercial web camera (Logitech QuickCam Pro 4000, 960 x 1280 pixel resolution) that was

rigidly mounted above the membrane at a single location to ensure a fixed field of view and frame of reference for the duration of the experiment. A series of five total images was collected (eight-bit grayscale) *via* laptop control of the camera—the baseline predeformation position and four subsequent positions with incremental stretches of approximately 5 mm each. Figure 4 is a schematic of the experimental setup, while Fig. 3(a) – 3(e) show an example dataset.

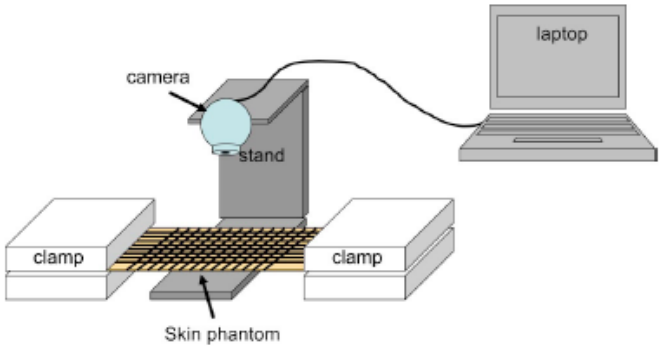

Figure 4. An illustration of the skin-phantom setup for image acquisition.

Material Testing Protocol

Material testing was performed in order to determine the accuracy of the reconstructed Young's modulus values. When the phantoms were poured, specimens of both the bulk and stiff polyurethane were allowed to cure in separate containers from the membranes. These samples were then cut into 1 cm x 1 cm x 1 cm cubes. Compression testing was performed on an EnduraTEC ELF 3200 material tester (EnduraTEC Systems Group, Minnetonka, MN). The polyurethane was assumed to be elastic, homogenous, and isotropic.

The Enduratec material testing protocol involved ramping the actuator linearly from the zero position to 24% strain at 2% strain increments. The max strain value was chosen to extend slightly beyond the range of observed strain in the experiment shown in Fig. 3 which was approximately 22% strain for the bulk material. Although the stiffer inclusion material only experienced approximately 1%–2% strain, stress values were reported for the full strain range up to 24%. Between each change in axial position a three second well time was imposed to allow viscoelastic responses to subside. Stress–strain plots were produced for both the bulk material and the inclusion material. Three samples of each material were tested and an average curve was calculated.

Phantom Experiment

To quantitatively test the MIE method within the context of dermoscopic applications using optical images, a series of studies using the elastic membrane of Fig. 3 were employed within the setup of Fig. 4. The single inclusion phantom was considered to be representative of a single lesion on the skin surface (nonpigmented in this case). The multiresolution MIE technique was used at each successive deformation for a total of four elasticity image reconstructions per similarity metric (in this case CC and GC only). The computational domain for these calculations involved 1051 nodes and 1973 elements. Boundary conditions were generated by analyzing the pre- and post-deformed structured grid and estimating the domain's deformation. The Young's modulus reconstructions were then compared to the elasticity values

as generated from the material testing protocol. It should be noted that only Young's modulus contrast was compared in these evaluations. This is due to the manner in which boundary conditions are prescribed in the model system. Currently, the approach is driven by displacement boundary conditions (i.e., Dirichlet type) which consequently make the elastic model only sensitive to Young's modulus contrast. Without knowledge of an applied stress at the boundary or a prescribed material property within the domain, absolute properties cannot be determined. In addition, it must also be noted that the reconstructions were constrained to a region of the phantom that was smaller than the overall phantom. This was a result from observing that at higher stretch states, out-of-plane distortions of the membrane became more prominent in the periphery.

Simulation Experiments

In an effort to test the algorithm within the context of a more realistic image acquisition scenario for skin cancer, a simulation study was performed on an image of the 1 cm melanoma lesion shown in Fig. 5(a). In addition, a grid structure was not specifically applied to the lesion image so as to test whether the natural skin-texture itself contained sufficient image information for reconstruction. The lesion was provided by the Dermatology Image Atlas project (*www.dermatlas.org*, Image Name: melanoma_1_040510, Contributed by Eric Ehrsam, M.D.) and represents a 1 cm pigmented melanoma plaque, located on the left arm of a 35-year-old woman [38]. For the simulation

boundary conditions, an annulus-shaped mechanical stretching device was assumed which would systematically stretch two semicircular regions apart by 2 mm. The melanoma was assumed to have a 2:1 elasticity contrast level with normal tissue, i.e., the melanoma was twice as stiff as the surrounding skin. The computational domain for the inverse problem contained 1294 nodes and 2459 elements. In addition, the mesh used to generate the forward-problem data was approximately 10% more resolved than the mesh used for reconstruction. This introduced a small degree of variability to the boundary conditions and image deformation to simulate potential acquisition noise. Figure 5(b) and Fig. 5(c) illustrates the localized application of the stretching and the simulated solution for both horizontal and vertical displacements, respectively. Upon completion, these image data was used as input to the multiresolution MIE algorithm. Results are reported using the CC and GC image similarity methods.

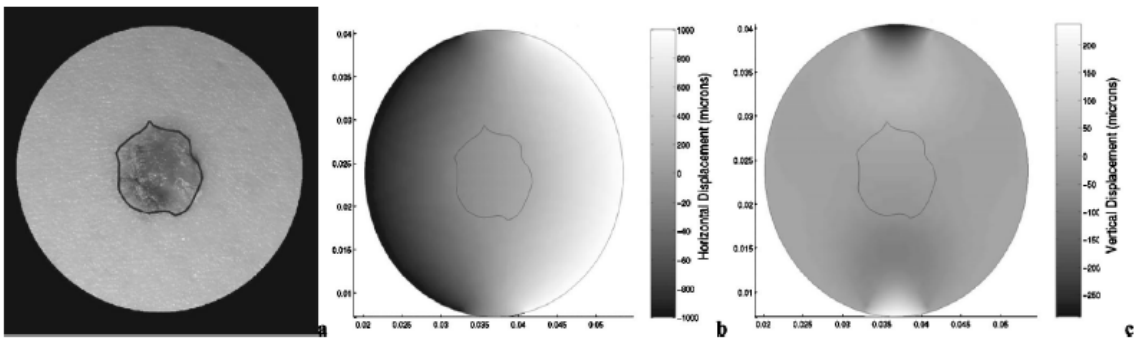

Figure 5. (a) Melanoma lesion, reproduced with the permission of Dr. Lehmann, MD., © Dermatlas, www.dermatlas.org, melanoma_1_040510. (b) Simulated horizontal and (c) vertical displacements shown (axis references are in meters while the gray scale is in microns). It should be noted that the contained region within the border represents the spatial regions of the stiffness in this simulation and was not contained within image data provided to the MIE algorithm.

Results

Material Testing

During the material testing phase, additional cyclic testing was performed in which viscoelastic behavior was noted. As a result, a waiting period was utilized at each strain level to allow viscoelastic responses to subside. The stress/strain behaviors at these quasistatic time periods for the bulk material and inclusion are shown in Figs. 6(a) and 6(b).

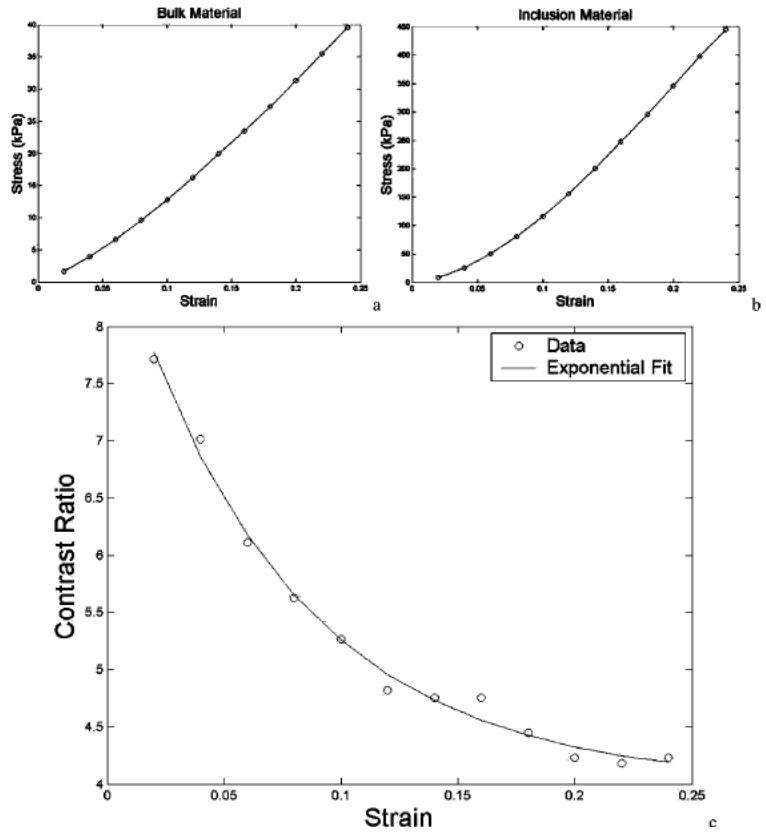

Figure 6. (a) Stress versus strain behavior for bulk material, (b) stress versus strain behavior for inclusion material, and (c) inclusion-to-bulk contrast ratio at various levels of bulk material strain (for all ratio determinations, the inclusion's 2% strain value for Young's modulus was used which was the approximate maximum strain reached in the inclusion based on experiment observations).

In addition, discrete finite difference approximations were made at the various strain levels to estimate a Young's modulus value. Table I represents a distribution of values calculated within the strain ranges tested. Once each modulus was calculated for each acquired strain level, a distribution of Young's modulus contrast ratios was calculated and is expressed by Eq. (2):

$$\mathrm{CR}(\varepsilon_{\mathrm{bulk}}) = \frac{E_{\mathrm{inc}}|_{\varepsilon=0.02}}{\overline{E}_{\mathrm{bulk}}}, \tag{8}$$

whereby the inclusion's 2% strain value (approximate maximum strain reached in the inclusion based on experimental observations) for Young's modulus was used and the bulk material was allowed to vary over the entire strain range. This contrast ratio formulation reflects the reality of the membrane experiments shown in Fig. 3 whereby the soft surrounding material experienced the majority of deformation with the inclusion remaining relatively unchanged over all applications of stretch. The distribution of the contrast ratios as described by Eq. (8) at differing strain levels is shown in Fig. 6(c).

To assist in determining inclusion-to-bulk contrast ratios for different bulk strain levels in each experimental stretch as reflected in Fig. 3, an exponential curve fit was prescribed:

$$\mathrm{CR}(\varepsilon = \varepsilon_{\mathrm{bulk}}) = A + Be^{-C\varepsilon}, \tag{9}$$

whereby A=4.0, B=5.0, C=13.8. The root mean square contrast ratio error between model and acquired data over the entire acquired strain range was 0.093. The quality of the exponential model can be seen in Fig. 6(c). Using the

expression described in (9), a series of Young's modulus contrast ratios values could be tabulated as a function of the specific strain levels used within the experiments of Fig. 1. These levels were determined by manually measuring strain levels within regions of the bulk material from the optical images. Table II reports the approximate contrast ratio for Young's modulus at the various bulk material strain levels experience during the stretching experiments using Eq. (9).

TABLE I. Young's elastic modulus values at several experimental strain levels.

Material strain (%)	Bulk material (kPa)	Inclusion material (kPa)
2	112.5	868.0
8	154.3	1635.0
12	180.0	2125.0
16	182.5	2375.0
23	206.3	2412.5

TABLE II. Contrast ratios for each experimental strain level.

Bulk material strain	Contrast ratio
Stretch 1: 8%	5.7
Stretch 2: 12%	5.0
Stretch 3: 16%	4.6
Stretch 4: 23%	4.2

Multiresolution MIE Phantom Reconstructions

Figures 7 and 8 are representations of the multiresolution elasticity image reconstruction performance for each of the different stretch states shown in Fig. 3 using CC and GC as the basis for image similarity, respectively.

The boundary contour represents the inclusion location as shown within the image. The contrast ratios designated within the transect images of Figs. 7 and 8 were based on Table II.

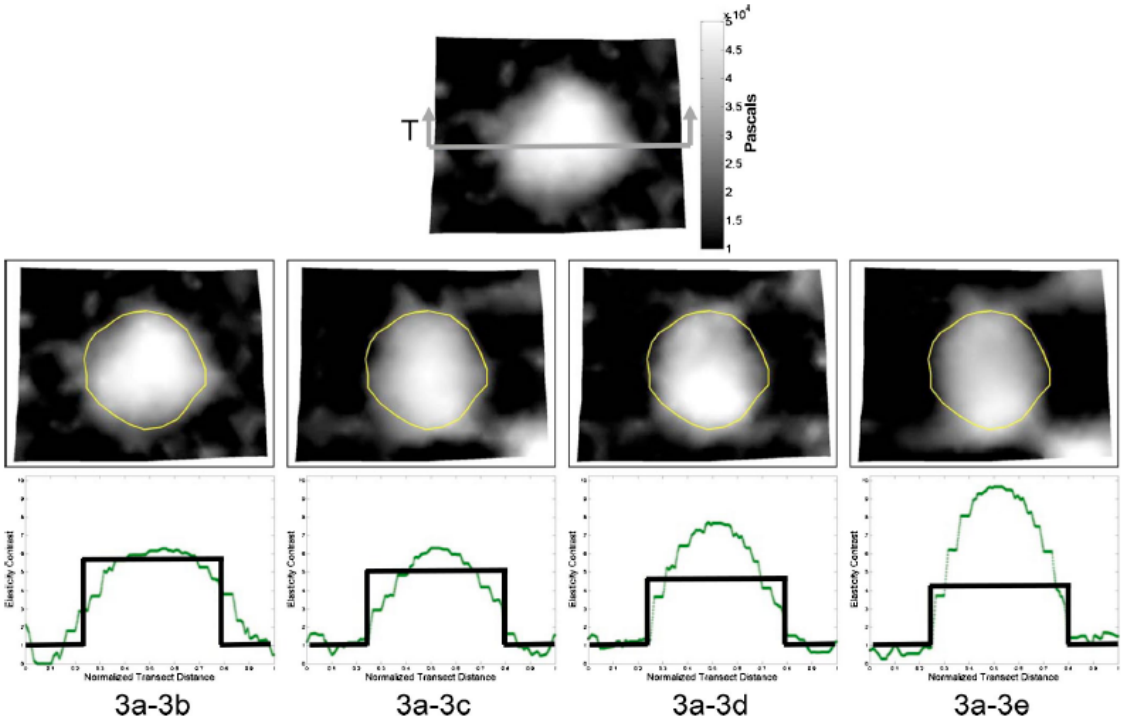

Figure 7. An illustration of elasticity image reconstructions using CC where each column represents the respective stretch relative to Fig. 3 (e.g., 3a-3b represents the stretch from base to the first increment). The top image shows the location of a transect as designated by the T and the gray scale associated with Young's Modulus (Pa). The middle row represents the reconstructed elasticity images at each stretch state with the contour showing the actual inclusion location. The bottom row shows the elastic property contrast ratio as compared to that predicted with the material testing (shown as a dark box-like contour) along the transect T.

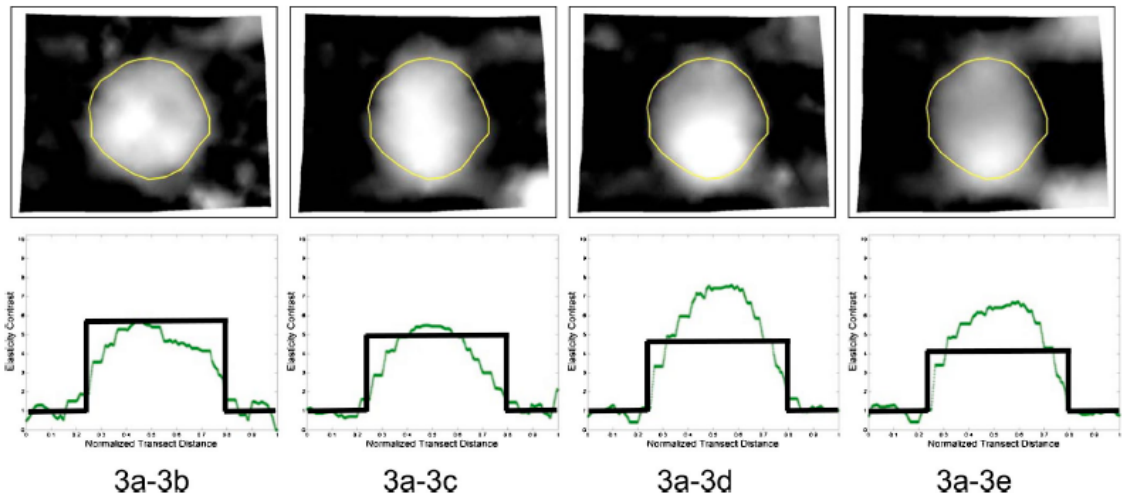

Figure 8. Illustration of elasticity image reconstructions using GC where each column represents the respective stretch relative to Fig. 3 (e.g., 3a-3b represents the stretch from base to the first increment). The top row represents the reconstructed elasticity images at each stretch state. The bottom row shows the elastic property contrast ratio as compared to that predicted with the material testing (shown as a dark box-like contour) along the transect T which was designated in Fig. 7.

Figure 9 shows elasticity images at varying stage resolutions within the multiresolution MIE reconstruction (reconstruction shown is the GC–3a–3b stretch regime).

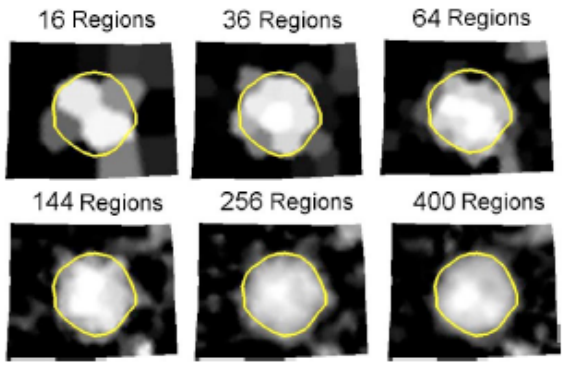

Figure 9. Elasticity image reconstruction for the GC 3a-3b reconstruction case at various resolutions of the multiresolution algorithm. The gray scale is the same is in Fig. 7.

To test the effect of the multiresolution framework, the same optical images were provided to our algorithm using a 400 property *region* resolution with an initial guess of homogeneity (i.e., coarser resolution solutions were not used as initial guesses). In results not reported here, the CC reconstruction was able to localize and quantify the stiff region similar to that of Fig. 7 at the high stretch states but was much worse with respect to the initial stretch state (i.e., 3a–3b image reconstruction).

Figure 10 represents the GC result for the four stretch states using the single 400 *region* high resolution parametrization. In Fig. 10(a) (3a–3b stretch state), the inclusion is localized but the contrast resolution is poor compared with its multiresolution counterpart in Fig. 8, first column. At subsequent stretch states (3a–3c, 3a–3d, and 3a–3e), the elasticity image has not converged to an acceptable representation of the inclusion. Interestingly, the distance traveled by grid squares within the homogenous regions near the stretching edge within the second stretch state (3a–3c) is approximately the size of one grid square (~1 cm).

It is evident that by using a single high resolution parametrization as opposed to a multiresolution approach, a local minimum is found and the elasticity image degrades considerably. Consequently, the error magnitude for the image shown in Fig. 8, the second column is a factor of 50% smaller than that of Fig. 10(b) thus demonstrating that Fig. 10(b) indeed represents a local minimum (it should be noted that all parameters were identical—number of similarity *zones*, filtering, regularization, relaxation, etc.).

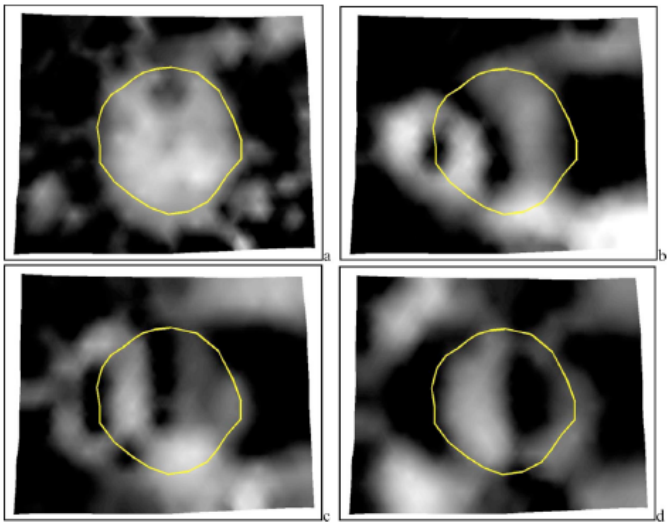

Figure 10. GC reconstructions using single 400 property zone resolution for (a) 3a-3b, (b) 3a-3c, (c) 3a-3d, and (d) 3a-3e, respectively. The gray scale is the same as in Fig. 7.

Multiresolution MIE Melanoma Reconstructions

In addition to the experimental results shown above, several similar simulations were executed using a pigmented melanoma image. Figure 11 shows the elasticity image reconstruction and transect results using the multiresolution MIE framework for both CC and GC. Figure 12 illustrates the inter-resolution results from the GC reconstruction shown in Fig. 11.

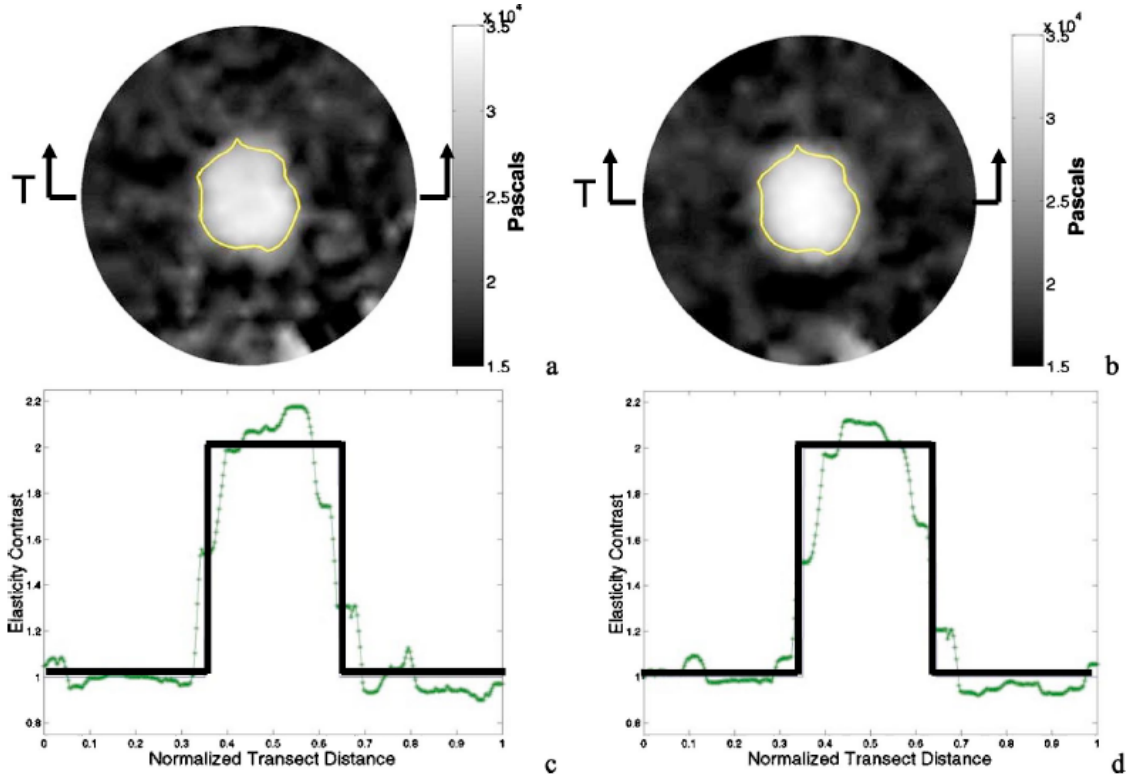

Figure 11. Elasticity image reconstruction of melanoma using (a) CC and (b) GC with contrast ratio values along the transect for (c) CC and (d) GC, respectively. The location of transect is designated by the T shown in (a) and (b).

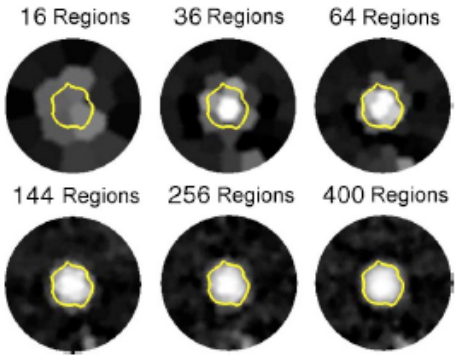

Figure 12. An example of multi-resolution solution development using GC for melanoma simulation.

Discussion

The elasticity image results from phantom (Figs. 7–9) and simulation (Figs. 11 and 12) studies demonstrate the utility of the multiresolution MIE approach. In addition, comparing the results in Figs. 8 and 10 clearly illustrates that instances can exist in which a single-resolution approach will fail whereas the multiresolution succeeds. A separate but related concern which is still under investigation is the degree and content of the image pattern needed to facilitate reconstruction; however, the preliminary elasticity image results from the melanoma simulations reported herein suggest that a sufficient intensity content exists in standard dermoscopic images.

Another important advance in this paper over previous work is the comparison between reconstructed elastic properties and their separately measured counterparts. The stress–strain curves shown in Figs. 6(a) and 6(b) and modulus values in Table I demonstrate a nonlinear elastic behavior. A good representative exponential fit to the Young's modulus contrast ratio data was achieved in Fig. 6(c) and provides a direct comparison to MIE-derived Young's modulus properties. One shortcoming is that because MIE is completely driven by displacement boundary conditions, only the contrast in Young's modulus values can be compared. However, the goal within this work is to investigate elastic properties as a mechanism for contrast within medical images.

Overall, the elastic image reconstructions shown in Figs. 7 and 8 demonstrated good localization with a varied performance in maintaining

lesion shape integrity for both the CC and GC similarity methods, respectively. It appears that at high strain levels, MIE was less successful at capturing the anticipated contrast ratio. In fact, in both CC and GC, the ratio was overestimated, thus producing more contrast. It should be noted that the reconstructions shown were performed on a domain that represented only a portion of the image that surrounded the inclusions (3–4 cm from the inclusion border). This was due to our inability to completely control the physical boundaries of the phantom given the large mismatch between the stiffness values of the two materials. This manifested itself as out-of-plane warping of the phantoms, i.e., a wrinkling at edges as the strain on the skin phantoms increased. The spatial location of these membrane distortions was more prominent with the distance from the inclusion. By making a more localized reconstruction region, the influence of these distortions was minimized although some effects are undoubtedly present. Ultimately, these out-of-plane motions would be interpreted as planar strains in the optical image acquisition system shown in Fig. 4. Although this variability in shape integrity existed, successful localization was achieved for all stretch states. It was encouraging that at small stretch states, where the model is most appropriate, proper quantitative contrast ratios were achieved (stretch states 3a–b, 3a–c in Figs. 7 and 8). Further encouragement was provided by successful localizations at high stretch states whereby nonlinear behavior is undoubtedly present and the small-strain assumptions are compromised (although the quantitative contrast ratio was not as satisfying). Undoubtedly, a large-deformation model is

necessary at these higher strains to match contrast ratios at this level; however, if proper empirical characterizations could be done using the linear model over many stretch states, effective contrast thresholds could be determined for the characterization of lesions. In addition, these results were also promising in that successful Young's modulus contrast and localization was achieved with a nonpigmented lesion. This indicates that only the deflections of the surrounding image pattern and not the lesion image intensity itself are responsible for the changes in the elastic modulus values. This enthusiasm must be tempered by the realization, however, that the *in vivo* model may require more thought with respect to boundary conditions. Undoubtedly, the influence of subcutaneous tissue connectivity would influence the results here if these additional constraints were applied. Given the inherent link between the image formation and the validity of the computational model, more work needs to be performed prior to clinical deployment.

Although these results are encouraging, not all reconstructions exhibited the same peak modulus or lesion localization. One reason could be the accuracy to which boundary conditions were determined for each stretch state. It is possible that the manual delineation of boundary conditions or the observed wrinkling at high stretch states resulted in some boundaries being mapped less precisely than others. In some of the reconstructions, significant boundary artifacts can be observed. For example, in the second and fourth column of Fig. 7, a Young's modulus peak is shown in the lower right hand region of the boundary. A second candidate for reconstruction inaccuracies

across stretch states could be the degree of model-data mismatch. It is interesting to note the correlation between increased stretch and the marked decrease in accuracy of the contrast-ratio transect plots. At the smaller stretches, 3a–b and 3a–c, both CC and GC reconstructions perform better in both localization and quantification while both show overpredictions within transects for stretch states, 3a–d and 3a–e. A model-data mismatch would seem a likely source for this change in performance, considering that the elastic model used is a small-strain model and the levels of strain are less in the first two stretch states. One somewhat qualitative observation that can also be made is that the GC-based method appears to reconstruct somewhat better than the CC-based method. This is also the case within the melanoma simulations. Interestingly, in Ref. 30, a similar experience was found in that the GC method outperformed other methods with respect to our phantom reconstructions. The principal difference between the CC and GC similarity methods is the form of the image to be used when calculation the correlation coefficient. GC employs the edge map of the image while CC uses the raw acquired image. The increased performance by GC may indicate that areas of structured sharp gradient intensities influence the MIE approach more significantly than more gradual intensity changes. However, this statement must be tempered with the realization of Fig. 10 whereby structural decorrelation has occurred although arguably at much larger length scales as compared to those in traditional USE.

The results from the melanoma simulations provide a more realistic representation of the types of images that can be acquired within the clinic. These images provide their own challenge in that although the lesion is pigmented, the surrounding structured pattern of the grid used in the phantom was not present. In this case, it was desirable to test MIE without the presence of the structured grid. Overall, the elasticity images and transects were satisfying, with the GC qualitatively outperforming the CC method. One interesting observation is related to the apparent suppression of modulus noise within the GC elasticity image as compared to the CC. This is more than likely due to the suppression of low-frequency image characteristics associated with extracting edges within the source and target images.

Figures 9 and 12 demonstrate the multiresolution aspect to our approach by showing the reconstructions at all six resolutions used within the generation of our images. One beneficial aspect is the availability of intraresolution elasticity images which represent accurate, albeit coarse, assessments of image progression. In addition, these intraresolution images could be used to dynamically alter the *K*-means clustering approach to locally refine the reconstruction process for the next resolution (although not done in this study). This would alter the algorithm representation in Fig. 2 by replacing precomputed resolution maps with an internal process block which calculated *K*-means *regions* dynamically based on areas of interest found during the reconstruction process.

Conclusions

In this paper, a novel multiresolution extension to Modality Independent Elastography (MIE) has been implemented which simplifies previous work (a dual-grid technique) and is shown to be more robust than the single-resolution version. In addition, the multi-resolution architecture implemented facilitates the monitoring of reconstruction quality at intermediate resolutions. To test the approach, a membrane experimental setup was created which utilizes sets of optical images for the reconstruction process. The use of optical images to generate Young's modulus reconstructions does represent a new modality within MIE development and could potentially be used within dermoscopic applications. Results from phantom and simulation experiments demonstrated that the multiresolution MIE approach is viable within the context for both nonpigmented and pigmented lesions, respectively. The nonpigmented phantom experiment highlighted direct comparisons between images of Young's modulus contrast and their independently measured counterparts, as provided by mechanical testing. Overall, the results indicated good localization and quantification. However, results did indicate a dependence on the fidelity of the reconstruction and the degree of applied deformation. In addition to the phantom experiment, a simulation using a clinical image of a pigmented melanoma was reported and illustrated excellent localization and quantification. Despite potential limitations in elasticity image resolution when compared to traditional MRE and USE, MIE's adaptability to an optical image-registration platform at multiple scales is an intriguing possibility.

Furthermore, this extension to another modality demonstrates that MIE-based approaches to elastography represent a new class of algorithms that may yield potentially new frameworks for disease characterization.

Acknowledgments

This work was supported in part by the Whitaker Young Investigator Program, Whitaker Foundation, Arlington, VA. The authors would like to acknowledge the contribution of Chad W. Washington from the University of Mississippi, School of Medicine for his assistance in laboratory training of students involved in this work.

References

[1] American Cancer Society, “Cancer facts and figures 2004,” July, 2004.

[2] A. A. Marghoob, L. D. Swindle, C. Z. M. Moricz, F. A. S. Negron, B. Slue, A. C. Halpern, and A. W. Kopf, “Instruments and new technologies for the in vivo diagnosis of melanoma,” J. Am. Acad. Dermatol. 49, 777–797, 2003.

[3] E. Ruocco, G. Argenziano, G. Pellacani, and S. Seidenari, “Noninvasive imaging of skin tumors,” Dermatol. Surg. 30, 301–310, 2004.

[4] R. Dua, D. G. Beetner, W. V. Stoecker, and D. C. Wunsch, “Detection of basal cell carcinoma using electrical impedance and neural networks,” IEEE Trans. Biomed. Eng. 51, 66–71, 2004.

[5] M. Gniadecka, P. A. Philipsen, S. Sigurdsson, S. Wessel, O. F. Nielsen, D. H. Christensen, J. Hercogova, K. Rossen, H. K. Thomsen, R. Gniadecki, L. K. Hansen, and H. C. Wulf, “Melanoma diagnosis by Raman spectroscopy and neural networks: Structure alterations in proteins and lipids in intact cancer tissue,” J. Invest. Dermatol. 122, 443–449, 2004.

[6] C. Edwards and R. Marks, “Evaluation of biomechanical properties of human skin,” Clin. Dermatol. 13, 375–380, 1995.

[7] L. J. Draaijers, Y. A. M. Botman, F. R. H. Tempelman, R. W. Kreis, E. Middelkoop, and P. P. M. van Zuijlen, “Skin elasticity meter or subjective evaluation in scars: A reliability assessment,” Burns 30, 109–114, 2004.

[8] G. E. Pierard, C. Pierard-Franchimont, S. Vanderplaetsen, N. Franchimont, U. Gaspard, and M. Malaise, “Relationship between bone mass density and tensile strength of the skin in women,” Eur. J. Clin. Invest 31, 731–735, 2001.

[9] G. E. Pierard, S. Vanderplaetsen, and C. Pierard-Franchimont, “Comparative effect of hormone replacement therapy on bone mass density and skin tensile properties,” Maturitas 40, 221–227, 2001.

[10] H. S. Yoon, S. H. Baik, and C. H. Oh, “Quantitative measurement of desquamation and skin elasticity in diabetic patients,” Skin Res. Technol. 8, 250–254, 2002.

[11] C. Braham, D. Betea, C. Pierard-Franchimont, A. Beckers, and G. E. Pierard, “Skin tensile properties in patients treated for acromegaly,” Dermatology, Basel, Switz.d 204, 325–329, 2002.

[12] J. A. Clark, J. C. Y. Cheng, and K. S. Leung, “Mechanical properties of normal skin and hypertrophic scars,” Burns 22, 443–446, 1996.

[13] H. Dobrev, “In vivo study of skin mechanical properties in psoriasis vulgaris,” Acta Derm Venereol 80, 263–266, 2000.

[14] D. N. H. Enomoto, J. R. Mekkes, P. M. M. Bossuyt, R. Hoekzema, and J. D. Bos, “Quantification of cutaneous sclerosis with a skin elasticity meter in patients with generalized scleroderma,” J. Am. Acad. Dermatol. 35, 381–387, 1996.

[15] N. Nikkels Tassoudji, F. Henry, C. PierardFranchimont, and G. E. Pierard, “Computerized evaluation of skin stiffening in scleroderma,” Eur. J. Clin. Invest 26, 457–460, 1996.

[16] H. Sumino, S. Ichikawa, M. Abe, Y. Endo, O. Ishikawa, and M. Kurabayashi, “Effects of aging, menopause, and hormone replacement therapy on forearm skin elasticity in women,” J. Am. Geriatr. Soc. 52, 945–949, 2004.

[17] J. Ophir, I. Cespedes, H. Ponnekanti, Y. Yazdi, and X. Li, “Elastography—A quantitative method for imaging the elasticity of biological tissues,” Ultrason. Imaging 13, 111–134, 1991.

[18] R. Muthupillai, D. J. Lomas, P. J. Rossman, J. F. Greenleaf, A. Manduca, and R. L. Ehman, “Magnetic-resonance elastography by direct visualization of propagating acoustic strain waves,” Science 269, 1854–1857, 1995.

[19] L. V. Tsap, D. B. Goldgof, and S. Sarkar, “Nonrigid motion analysis based on dynamic refinement of finite element models,” IEEE Trans. Pattern Anal. Mach. Intell. 22, 526–543, 2000.

[20] L. V. Tsap, D. B. Goldgof, and S. Sarkar, “Fusion of physically-based registration and deformation modeling for nonrigid motion analysis,” IEEE Trans. Image Process. 10, 1659–1669, 2001.

[21] L. V. Tsap, D. B. Goldgof, S. Sarkar, and P. S. Powers, “A vision-based technique for objective assessment of burn scars,” IEEE Trans. Med. Imaging 17, 620–633, 1998.

[22] J. L. Gennisson, T. Baldeweck, M. Tanter, S. Catheline, M. Fink, L. Sandrin, C. Cornillon, and B. Querleux, “Assessment of elastic parameters of human skin using dynamic elastography,” IEEE Trans. Ultrason. Ferroelectr. Freq. Control 51, 980–989, 2004.

[23] M. I. Miga, “A new approach to elastography using mutual information and finite elements,” Phys. Med. Biol. 48, 467–480, 2003.

[24] J. Ophir, S. K. Alam, B. Garra, F. Kallel, E. Konofagou, T. Krouskop, and T. Varghese, “Elastography: ultrasonic estimation and imaging of the elastic

properties of tissues," Proc. Inst. Mech. Eng., Part H: J. Eng. Med. 213, 203–233, 1999.

[25] T. L. Chenevert, A. R. Skovoroda, M. O'Donnell, and S. Y. Emelianov, "Elasticity reconstructive imaging by means of stimulated echo MRI" Magn. Reson. Med. 39, 482–490, 1998.

[26] R. Sinkus, J. Lorenzen, D. Schrader, M. Lorenzen, M. Dargatz, and D. Holz, "High-resolution tensor MR elastography for breast tumour detection" Phys. Med. Biol. 45, 1649–1664, 2000.

[27] D. B. Plewes, J. Bishop, A. Samani, and J. Sciarretta, "Visualization and quantification of breast cancer biomechanical properties with magnetic resonance elastography" Phys. Med. Biol. 45, 1591–1610, 2000.

[28] E. E. W. Van Houten, M. I. Miga, J. B. Weaver, F. E. Kennedy, and K. D. Paulsen, "Three-dimensional subzone-based reconstruction algorithm for MR elastography" Magn. Reson. Med. 45, 827–837, 2001.

[29] M. M. Doyley, P. M. Meaney, and J. C. Bamber, "Evaluation of an iterative reconstruction method for quantitative elastography" Phys. Med. Biol. 45, 1521–1540, 2000.

[30] C. W. Washington and M. I. Miga, "Modality independent elastograph (MIE): A new approach to elasticity imaging" IEEE Trans. Med. Imaging, in press.
[31] A. P. Boresi, Elasticity in Engineering Mechanics, 2nd ed. Wiley, New York, 2000.

[32] L. Lapidus and G. F. Pinder, Numerical Solution of Partial Differential Equations in Science and Engineering sWiley, New York, 1982d.

[33] G. K. Rohde, A. Aldroubi, and B. M. Dawant, "The adaptive bases algorithm for intensity based nonrigid image registration" IEEE Trans. Med. Imaging 22, 1470–1479 s2003d.

[34] D. Rueckert, C. Hayes, C. Studholme, P. Summers, M. Leach, and D. J. Hawkes, "Non-rigid registration of breast MR images using mutual information," in Medical Image Computing and Computer-Assisted Intervention— Miccai'98, Lecture Notes in Computer Science, 1998, Vol. 1496, pp. 1144–1152.

[35] D. Rueckert, L. I. Sonoda, C. Hayes, D. L. G. Hill, M. O. Leach, and D.J. Hawkes, "Nonrigid registration using free-form deformations: Application to breast MR images," IEEE Trans. Med. Imaging 18, pp. 712–721, 1999.

[36] D. W. Marquardt, "An algorithm for least-squares estimation of nonlinear parameters," SIAM J. Appl. Math. 11, 431–441 s1963d.

[37] N. Joachimowicz, C. Pichot, and J. P. Hugonin, “Inverse scattering: an iterative numerical method for electromagnetic imaging” IEEE Trans. Biomed. Eng. 39, 1742–1752, 1991.

[38] B. A. Cohen and C. U. Lehmann, “Dermatology Image Atlas” Dermatlas, 2000–2004.

[39] T. L. Bialy, J. Whalen, E. Veledar, D. Lafreniere, J. Spiro, T. Chartier, and S. C. Chen, “Mohs micrographic surgery vs traditional surgical excision—A cost comparison analysis,” Arch. Dermatol. 140, 736–742, 2004.

CHAPTER III

MANUSCRIPT 2: APPLICATION OF MULTI-RESOLUTION MODALITY INDEPENDENT ELASTOGRAPHY FOR DETECTION OF MULTIPLE ANOMALOUS OBJECTS

Jao J. Ou, Stephanie L. Barnes, Michael I. Miga

Vanderbilt University, Department of Biomedical Engineering, Nashville, TN 37235

This manuscript has been published in the proceedings of *Medical Imaging 2006: Physiology, Function and Structure from Medical Images,* SPIE Press, vol. 6143, pp. 614310-1 to 614310-9, 2006

Abstract

This work extends a recently realized inverse problem technique of extracting soft tissue elasticity information via non-rigid model-based image registration. The algorithm uses the elastic properties of the tissue in a biomechanical model to achieve maximal similarity between image data acquired under different states of loading. A new multi-resolution, non-linear optimization framework has been employed which allows for improved performance and object detection. Prior studies have demonstrated successful reconstructions from images of a tissue-like thin membrane phantom with a single embedded inclusion that was significantly stiffer than its surroundings. For this investigation, a similar phantom was fabricated with two stiff inclusions to test the effectiveness of this method in discriminating multiple smaller objects. Elasticity values generated from both simulation and real data

testing scenarios provided sufficient contrast for detection and good quantitative localization of the inclusion areas.

Introduction

The practice of palpating soft tissue structures in the course of the clinical physical exam has had a long-standing history of providing correlation of improper stiffness with pathology. The ability to characterize the mechanical properties of tissue is a potential source of additional information relevant for detection and diagnosis of a disease process, and has implications for the assessment of treatment. One way in which this could be achieved in a minimally invasive manner is by analyzing tissue deformation through imaging and/or image processing techniques, which is a central goal of the field of elastography [1]. Application of such methods to the interrogation of the breast [2,3], skin [4-6], prostate [7], and other accessible organ systems is an emerging area of research.

Many of the current elastography methods are founded in ultrasound (US) and magnetic resonance imaging (MR) and involve the estimation of induced displacements within the tissue of interest to infer the elasticity distribution. We have pursued the development of a reconstruction method utilizing quasi-static deformation and image similarity metrics that has been termed 'modality-independent elastography' (MIE) [8-10] because of its potential to handle native anatomical image data from different modalities

with simple modification to the acquisition procedure. Common problems facing all of these methods involve limitations with the accurate recovery of elastic property values, detection of small lesions in tissue, and the resolution of multiple discrete lesions [11,12]. Building upon recent study involving a single focal lesion [6], the objectives of this work were to challenge the ability of the MIE method to reconstruct a scenario of two small inclusions embedded in a homogeneous domain and to further explore the feasibility of the method in handling image data from different imaging modalities. This was accomplished by performing simulated reconstructions using images obtained from X-ray computed tomography (CT), MR, and digital photography and then a reconstruction from a real-world experiment using a thin phantom membrane.

Methods

Elastographic reconstruction framework

The conceptual framework for our elastographic reconstruction has been previously described in [6,8-10]. In brief, an image of a tissue of interest (source) is deformed by a biomechanical computer model and compared against an acquired image of the same tissue in a mechanically loaded state (target). The deformation and comparison is repeated using systemic updates of elasticity parameters until a suitable match in intramodal image similarity is achieved in a least squares manner to satisfy a multi-resolution, non-linear optimization scheme. This process can be classified as an inverse problem, with model-based deformation of the source image representing the forward

problem. Each of the three major components (model, image comparison, and optimization) is described in more detail in the following sections, and a flow chart representation of the overall process is included in Figure 13.

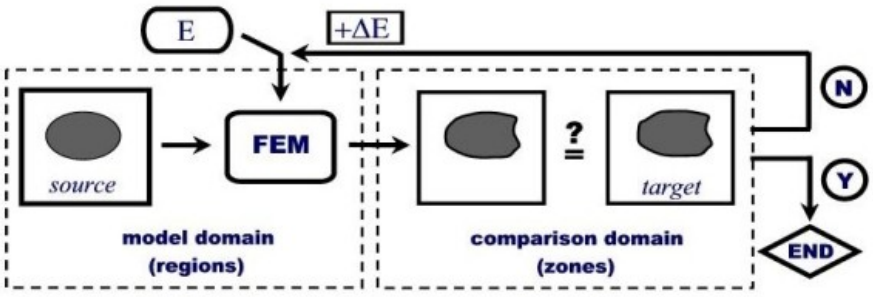

Figure 13. Flow chart of elastographic reconstruction framework.

Elastographic reconstruction framework: Biomechanical model

A central component to the model-based inverse problem is the manner in which the continuum is represented. While the constitutive model that best describes tissue deformation mechanics is more complex, for this work, linear isotropic elasticity has been employed. The partial differential equation that expresses a state of mechanical equilibrium can be written as [13]:

$$\nabla \bullet \sigma = 0 \tag{1}$$

where σ is the Cartesian stress tensor.

For the purposes of the following experimentation, we also apply either the plane stress or plane strain approximations to the thin membrane and breast cross-section trials, respectively. The direct consequence of this is a reduction of the 36 stiffness constraints in the general 3D formulation of Cauchy's Law to

the two parameters of Young's modulus (E) and Poisson's ratio (ν) in 2D. These simplifications, while significant, are appropriate descriptions of sufficiently thin and thick systems under planar loading. In plane stress,

$$\begin{bmatrix} \sigma_x \\ \sigma_y \\ \tau_{xy} \end{bmatrix} = \frac{E}{(1-\nu^2)} \begin{bmatrix} 1 & \nu & 0 \\ \nu & 1 & 0 \\ 0 & 0 & (1-\nu)/2 \end{bmatrix} \begin{bmatrix} \varepsilon_x \\ \varepsilon_y \\ \gamma_{xy} \end{bmatrix} \tag{2}$$

describes the constitutive relationship between the Cartesian stress tensor [σ_x, σ_y, τ_{xy}] and strain tensor [ε_x, ε_y, γ_{xy}]. Similarly, in plane strain,

$$\begin{bmatrix} \sigma_x \\ \sigma_y \\ \tau_{xy} \end{bmatrix} = \frac{E(1-\nu)}{(1+\nu)(1-2\nu)} \begin{bmatrix} 1 & \nu/(1-\nu) & 0 \\ \nu/(1-\nu) & 1 & 0 \\ 0 & 0 & \frac{(1-2\nu)}{2(1-\nu)} \end{bmatrix} \begin{bmatrix} \varepsilon_x \\ \varepsilon_y \\ \gamma_{xy} \end{bmatrix} \tag{3}$$

A finite element (FE) model using triangular elements is constructed from the source image and assigned appropriate boundary conditions based on estimated displacement or stress (i.e. Dirichlet and Neumann conditions, respectively). The standard Galerkin method of weighted residuals [14] is used to construct and solve the system.

Elastographic reconstruction framework: Image deformation and comparison

To further describe the reconstruction process, we introduce some additional terminology at this point. The *model domain* is equivalent to the total area of the FE mesh constructed using the *source* image as stated above

and contains the relevant elasticity information. The model domain is partitioned by a K-means clustering of the element centroids (MATLAB R14, Mathworks, Natick, MA) into *N* number of *regions*, each of which has a distinct set of spatially homogeneous elastic properties. Subdividing in this manner allows for the implementation of the multi-resolution reconstruction whereby progressively finer spatial distributions of elasticity parameters are utilized in the process, a method that improves upon previous versions using only a single resolution [8-10]. Analogously, the *comparison domain* is an area specified by semi-automated segmentation on the *target* image and contains information pertaining to image similarity. The comparison domain is separated into *M* number of rectangular *zones* containing approximately equal numbers of pixels.

The reconstruction algorithm begins by assigning an initial Young's modulus value to each of the regions at the coarsest resolution. Poisson's ratio is held constant at $\nu = 0.485$ to represent a nearly incompressible material. The FE model is solved to determine the nodal mesh displacements, which are in turn used to deform the source image. This model-deformed image is then compared to the target image for every zone using an intensity-based image similarity metric. While a number of methods are available for such a task, here, we utilize the correlation coefficient (CC) [15] throughout, as it has empirically demonstrated superior performance over other metrics such as the sum of squared differences and normalized mutual information.

Elastographic reconstruction framework: Optimization scheme

Let *T* be a function that represents the model-based image deformation and takes as its input a vector of elastic modulus values **E** of length *N* that corresponds to the current distribution of regions in the model domain. Then for two distributions of modulus values $\mathbf{E_1}$ and $\mathbf{E_2}$, the similarity between the images produced by $T(\mathbf{E_1})$ and $T(\mathbf{E_2})$ is the vector **S** of length *M* containing evaluations of the correlation coefficient corresponding to the distribution of zones in the comparison domain. The elasticity parameter optimization can be written as the minimization of the least squares error objective function

$$\Psi = \left| S_{TRUE} - S_{EST} \right|^2 \tag{4}$$

where $\mathbf{S}_{TRUE}$ is the set of similarity values achieved when comparing the target image to itself, $\mathbf{S}_{EST}$ is the similarity between the model-deformed source and the target images using current estimates of the elastic modulus distribution, and $|\bullet|$ denotes the vector L_2 norm. By definition, $\mathbf{S}_{TRUE}$ is the maximum value for the similarity metric (max CC = 1). Using a Levenberg-Marquardt approach, the residual form of equation (4) becomes

$$\left[J^T J + \alpha I \right] \{ \Delta E \} = \left[J^T \right] \{ S_{TRUE} - S_{EST} \} \tag{5}$$

where $\mathbf{J} = \partial \mathbf{S}_{EST} / \partial \mathbf{E}$ is the Jacobian matrix of size *M* x *N* and **I** is the *N* x *N* identity matrix. Because $\mathbf{J}^T\mathbf{J}$ is typically an ill-conditioned term, the regularization parameter α is determined using the methods described in [16].

Modulus values of the regions at a given resolution are updated by $\Delta \mathbf{E}$ until an error tolerance is reached or a maximum number of iterations have been completed. Upon reaching a stopping criterion, the material property description is interpolated onto the next (i.e. finer) resolution and the above steps are repeated. Spatial averaging of modulus values within the model domain and solution relaxation between successive resolution levels are also utilized to improve the stability of the optimization.

Reconstruction Experiments

A two-material phantom membrane of simulated skin had been previously constructed [6] using Smooth-On™ polyurethanes (Smooth-On, Easton, PA) designated by the manufacturer as Evergreen 10 and Evergreen 50. These materials have essentially indistinguishable colors but vary significantly in their elastic modulus values, so the former was used as the bulk material and the latter for stiff objects. From material testing, the elastic modulus contrast was expected to be approximately 5.7:1. The phantom was made to contain two circular stiff inclusions 1.5 cm in diameter embedded near opposing corners of a rectangular field of bulk material measuring 15 cm x 14 cm. A black permanent marker was used to place a pattern of regularly spaced (~1 cm) grid lines across the membrane. The thin membrane was securely clamped along two opposite edges and then subjected to a uniaxial tensile displacement (~8% strain) by means of a milling vise. A commercial webcam (Logitech QuickCam Pro 4000, 960 x 1280 pixel resolution) was rigidly mounted

above the membrane to acquire image pairs of the pre- and post-stretched states.

To initially test the method regarding the two-inclusion scenario, a simulation using the source image of the membrane was performed by deforming it with a prescribed model (plane stress) of known boundary displacements and elasticity parameters to generate a target image; high modulus values were assigned to elements bounded by a segmentation of the inclusion locations. A reconstruction was then performed using the actual image data acquired as described above. In both cases, resolutions of N = 16, 64, 256, 512, and 800 regions and M = 400 zones were used. The results of the idealized and real data reconstructions are shown in Figures 16 and 17, with further quantitative evaluation in Table 3.

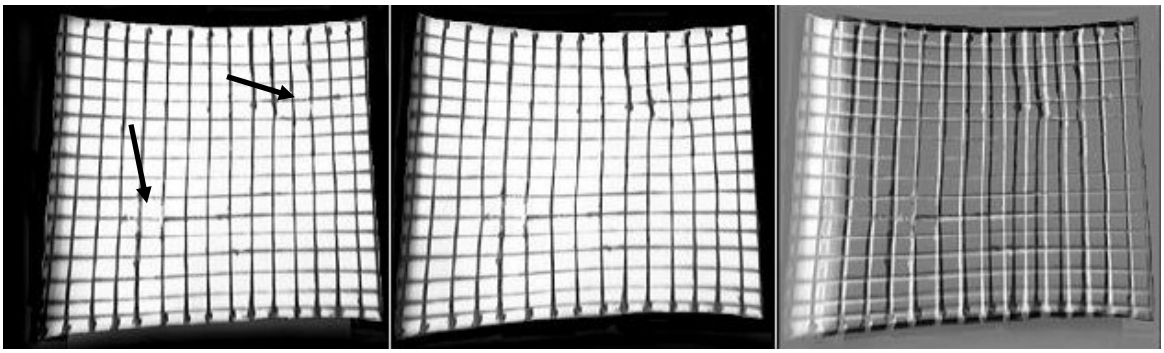

Figure 14. (Left to right): Phantom membrane in undeformed state (source image), under deformation (target image), and difference image. Arrows in the left panel indicate the positions of the two stiff inclusions.

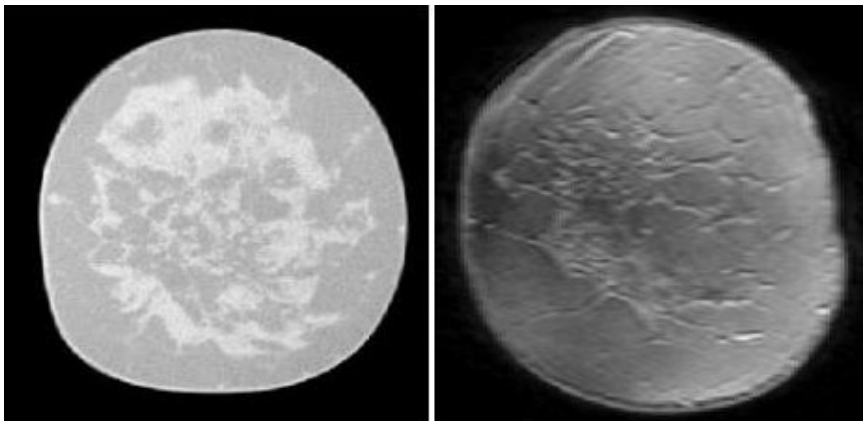

Figure 15. Images slices of breast tissue extracted from a CT volume (left) and MR volume (right) used in simulation study of the ability of the reconstruction method to utilize disparate image data types.

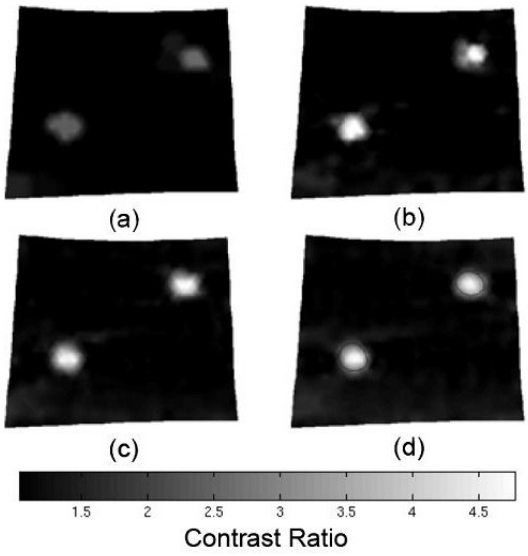

Figure 16. Reconstruction of the simulated membrane deformation using idealized model parameters, progressing through finer resolution distributions (a)-(d) of 64, 256, 512, and 800 regions.

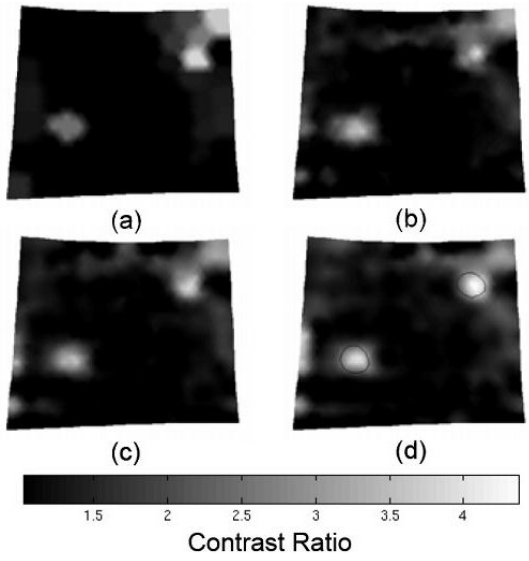

Figure 17. Reconstruction of the actual membrane data. A faint contour in (d) is present to demarcate the actual position of the stiff inclusions. Again, panels (a)-(d) demonstrate the effect of the multi-resolution method in utilizing 64, 256, 512, and 800 regions to better capture the shape and location of the inclusions.

Table 3. Quantitative reconstruction evaluations.

	Avg CR	Max CR	CNR	QRS (%)
Simulation	2.7	4.0	4.4	97.7
Phantom	2.6	4.1	2.8	88.5

In order to examine the robustness of the method regarding its use of data from differing sources, simulation reconstructions were performed using image slices extracted from breast image volumes obtained from CT and MR scans (see Figure 15). Although these were taken from two different patients, the images were selected to be approximately corresponding slices ~2 cm away from the chest wall in the coronal orientation of the standard anatomical position. The simulations were set up in the same manner as for the digital

photographs, using either one or two inclusions of about 1 cm in diameter embedded within the true elasticity distribution and a small compression (~8% strain) in the cranial-caudal direction. The relative stiffness of the inclusions was designated to be 5.7:1 for consistency with the material testing data and also because the value is fairly representative of breast tumor properties [17]. The plane strain model approximation was used in the breast simulation trials, progressing through resolutions of N = 24, 64, 256, and 576 regions using M = 200 zones. The reconstruction method was then run for all four test cases, and the results are presented in Figures 18 and 19 and Table 4.

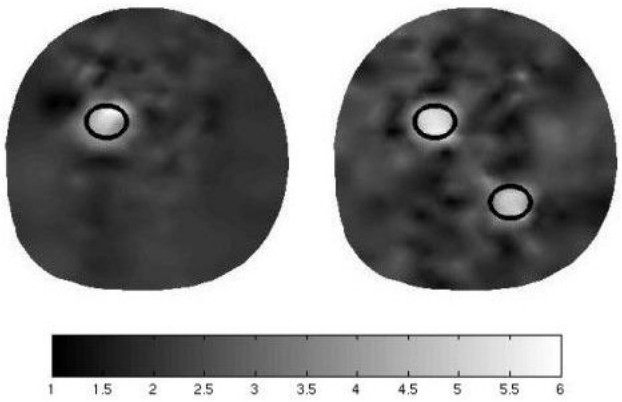

Figure 18. Reconstructions of simulation trials for the CT breast slice using a single inclusion (left) and two inclusions (right). The true inclusion boundaries are overlaid in each elasticity image.

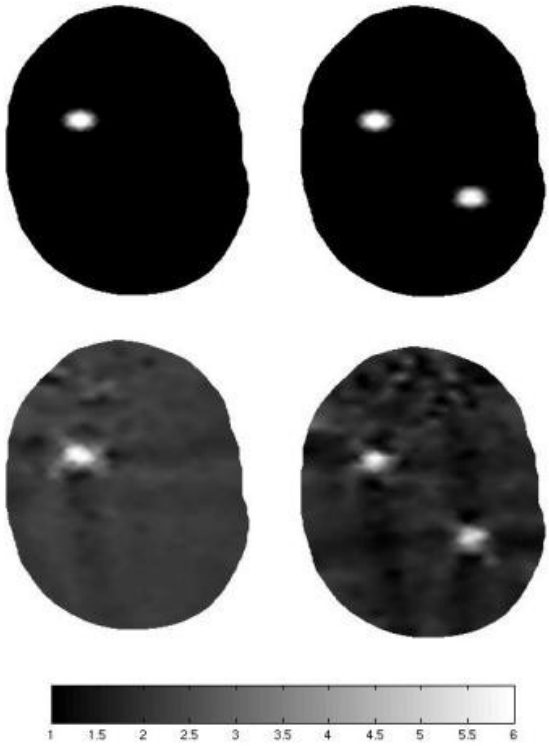

Figure 19. Reconstructions (bottom row) of simulation trials for the MR breast slice using a single inclusion (left) and two inclusions (right). The true elasticity distributions are also shown (top row) for comparison.

Table 4. Quantitative reconstruction evaluations.

	Avg CR	Max CR	CNR	QRS (%)
CT (1 inclusion)	2.1	3.1	3.0	97.6
CT (2 inclusions)	2.0	2.6	3.5	96.9
MR (1 inclusion)	2.8	3.7	20.0	100
MR (2 inclusions)	2.7	3.7	5.7	99.8

Reconstruction evaluation

The fidelity of the elasticity reconstruction was evaluated on its ability to detect the presence of an inclusion based on classification of the material property distribution, and the retrospective accuracy of localizing the lesions. The elastic properties as a whole were treated as a Gaussian mixture of two classes and separated by a threshold established via the method described in [18]. The likelihood of detecting a lesion in the elasticity image was found using the contrast-to-noise ratio as defined by [12,19]:

$$CNR = \sqrt{\frac{2(\mu_L - \mu_B)^2}{\sigma_L^2 + \sigma_B^2}} \tag{6}$$

where μ and σ^2 are the sample mean and variance of a material property distribution and the subscripts *L* and *B* denote the lesion and bulk material classes, respectively. As a quantitative assessment of the localization of the lesion(s), the positive predictive value of correctly identifying a lesion material within the known segmented region of the inclusions was used as a 'quality of reconstruction score' (QRS). This value is significant because identification of the lesion border and material classification are done independently, so any user knowledge of the test scenario does not influence the performance of the measure. Cutoffs for successful detection and localization were set at CNR≥2.2 as noted by [12] and QRS≥80% as determined by prior study in our laboratory. The average modulus contrast is found from the ratio of the means of the two

material classes, and a peak modulus contrast value is also reported by taking the ratio of two manually selected homogeneous regions of approximately equal area known to be representative of the two materials. It should be noted that in other work not presented here, the definition of QRS included a weighting factor provided by the estimated reconstruction modulus contrast, but for the current purposes, only localization accuracy was considered to maintain an objective evaluation of inclusion detection.

Results

Figure 16 demonstrates the ability of the reconstruction method to produce an elasticity map from the simulation data with good localization of the inclusions that are easily visually distinguishable from the surrounding bulk material. The progression through resolutions of N = 64, 256, 512, and 800 regions shows improving delineation of the inclusions and elastic contrast. Figure 17 demonstrates a similar behavior for the reconstruction of the acquired phantom membrane data, with both spatial definition and modulus contrast increasing with the finer discretization. Table 3 summarizes the quantitative evaluation of the reconstructions in both simulation and phantom trials, including CNR, contrast ratio, and QRS values. The CNR values are sufficient to allow for discrimination of the two materials and the identification of the inclusions was determined to be accurate in both cases. The reconstruction of the phantom membrane does show some misclassification

along the border where the deformation was applied as well as in the corner adjacent to one of the inclusions (see Figure 17d).

Figures 18 and 19 show the final reconstruction results for the CT and MR breast slice simulations using either one or two inclusions. In both test scenarios, the resolvability of the stiffer material was found to be adequate according to the CNR threshold, but definitely higher in the MR-derived elasticity images. Localization of the inclusions yielded excellent QRS values in reconstructions using either modality, again higher (though slightly) for the MR images.

Discussion

The results of the phantom membrane experiment are encouraging because of their similarity to the idealized simulation. Despite nonlinear model-data mismatch, out-of-plane distortions during stretching, and possible boundary condition inaccuracies, the elasticity reconstruction demonstrated good localization of the two small inclusions. The majority of the problems in reconstruction are mostly likely due to noise incurred in the mapping of the boundary displacements. It should be noted that the phantom reconstruction was achieved with a non-pigmented lesion (see Figure 14, arrows), indicating that deflections of the image structure are capable of driving the image similarity metric of the reconstruction process. This does intuitively suggest that some metric for rating the complexity and density of image pattern in relation to algorithm success may be important and is currently under

investigation. Preliminary data not presented in this work indicates that such a threshold does exist for image data that can be properly analyzed by the current framework. The modality independence of the method is also supported by the results here; clearly, the Hounsfield units of CT, floating point values from an MR volume, and the luminance captured by the CCD sensor of a digital camera are quite different types of data to handle because they are based on different physical principles. The simulation reconstructions demonstrate that the method is indifferent to these differences by treating the data as an arbitrary range of intensities and will converge towards the true elasticity distribution based on the image pattern available. This is a possible explanation for the qualitatively more satisfactory results from the MR simulations compared to the CT trials because the distribution of intensities from the former modality yielded a more diversified histogram, an attribute that should naturally aid an intensity-based metric.

While an ideal reconstruction would also be accurate in characterizing a lesion by its modulus contrast, our focus in the study was to test the ability of the method to detect and localize the inclusions. In previous experimentation with reconstructions of single focal lesions, we have been generally successful in achieving a contrast ratio within 25% of the true/expected value. It is somewhat troubling that the contrast ratios calculated here did not meet that criterion, although the experiments with the phantom membrane came fairly close (28%). However, these results underscore the difficulty of the scenarios in not only having to deal with multiple inclusions but quite small ones in both

the true physical sense and also the scale of the domain. Any of the given inclusions tested in simulation and with the real data were detected within a homogeneous domain approximately an order of magnitude larger (e.g., 1.5-cm lesions in a 15 cm x 14 cm domain for the phantom). The expectation of being able to identify with any confidence the presence of the inclusion is comparable to the observations made in [12] where the test of finding a single 5-mm lesion within a 4 cm x 5 cm domain proved to be the most problematic. Therefore, the localization of the lesions as determined by the CNR and QRS metrics is deemed to be a success, and further investigation into the nature of the method with respect to the scale of the lesion and domain is warranted.

Conclusions

In this work, we have presented further testing of a method for recovering elasticity parameters by maximizing the similarity between images of a tissue of interest acquired under two different states of quasi-static loading within the context of an inverse problem. The specific experiments presented here examined the effectiveness of the technique for the detection of multiple small discrete focal lesions embedded in an otherwise homogeneous medium, as well as further proof-of-concept work in its applicability to utilize image data from various modalities. In both cases, the method provided accurate localization of the lesions based on the reconstruction of relevant elasticity contrast. Because the biomechanical model, multi-resolution optimization, and image acquisition are each modular components of the

framework, this elastographic reconstruction technique is readily extensible for added sophistication, and there is ongoing work to enhance the methodology with more complex models and advances in imaging technology.

Acknowledgments

The authors would like to thank John Boone, PhD of the University of California-Davis, Department of Radiology and Tom Yankeelov, PhD of the Vanderbilt University Institute of Imaging Science for their generous contributions of breast image data (CT and MR, respectively). This work was supported in part by the Whitaker Foundation Young Investigator Award and the Congressionally Directed Medical Research Program BCRP Predoctoral Traineeship Award.

References

[1] J. Ophir, I. Cespedes, H. Ponnekanti, Y. Yazdi, and X. Li, "Elastography - a quantitative method for imaging the elasticity of biological tissues," *Ultrasonic Imaging*, vol. 13, pp. 111-134, 1991.

[2] A. L. McKnight, J. L. Kugel, P. J. Rossman, A. Manduca, L. C. Hartmann, and R. L. Ehman, "MR elastography of breast cancer: preliminary results," *AJR Am J Roentgenol*, vol. 178(6), pp. 1411-1417, 2002.

[3] R. Sinkus, M. Tanter, T. Xydeas, S. Catheline, J. Bercoff, M. Fink, "Viscoelastic shear properties of *in vivo* breast lesions measured by MR elastography," *Magn Reson Imaging*, vol. 23(2), pp. 159-165, 2005.

[4] L. V. Tsap, D. B. Goldgof, S. Sarkar, and P. S. Powers, "A vision-based technique for objective assessment of burn scars," *IEEE Trans Med Imaging*, vol. 17, pp. 620-633, 1998.

[5] Y. Zhang, D. B. Goldgof, S. Sarkar, and L. V. Tsap, "A modeling approach for burn scar assessment using natural features and elastic property," *IEEE Trans Med Imaging*, vol. 23, pp. 1325-1329, 2004.

[6] M. I. Miga, M. P. Rothney, and J. J. Ou, "Modality-independent elastography (MIE): potential applications for dermoscopy," *Medical Physics*, vol. 32, pp. 1308-1320, 2005.

[7] L. Curiel, R. Souchon, O. Rouviere, A. Gelet, and J. Y. Chapelon, "Elastography for the follow-up of high-intensity focused ultrasound prostate cancer treatment: initial comparison with MRI," *Ultrasound Med Biol*, vol. 31(11), pp. 1461-1468, 2005.

[8] C. W. Washington and M. I. Miga, "Modality independent elastography (MIE): a new approach to elasticity imaging," *IEEE Trans Med Imaging*, vol. 23, pp. 1117-1128, 2004.

[9] M. I. Miga, "A new approach to elastography using mutual information and finite elements," *Phys Med Biol*, vol. 48, pp. 467-480, 2003.

[10] M. I. Miga, "A new approach to elastographic imaging: modality independent elastography," *Proceedings of the SPIE*, vol. 4684, pp. 604-611, 2002.

[11] K. J. Parker, L. S. Taylor, S. Gracewski, and D. J. Rubens, "A unified view of imaging the elastic properties of tissue," *J Acoustical Soc of America*, vol. 117(5), pp. 2705-2712, 2005.

[12] M. M. Doyley, J. B. Weaver, E. E. W. Van Houten, F. E. Kennedy, and K. D. Paulsen, "Thresholds for detecting and characterizing focal lesions using steady-state MR elastography," *Medical Physics*, vol. 30(4), pp 495-504, 2003.

[13] A. Boresi, *Elasticity in Engineering Mechanics*, Wiley-Interscience, 2000.

[14] L. Lapidus and G. F. Pinder, *Numerical Solution of Partial Differential Equations in Science and Engineering*, John Wiley & Sons, 1982.

[15] J. M. Fitzpatrick, D. L. G. Hill, C. R. Maurer, "Image registration," *Handbook of Medical Imaging*, vol. 2. SPIE Press, pp. 447-513, 2000.

[16] N. Joachimowicz, C. Pichot, and J. P. Hugonin, "Inverse scattering: an iterative numerical method for electromagnetic imaging. *IEEE Trans Biomed Engineering*, vol. 39, pp. 1742-1752, 1991.

[17] T. A. Krouskop, T. M. Wheeler, F. Kallel, B. S. Garra, and T. Hall, ''Elastic moduli of breast and prostate tissues under compression,'' *Ultrasonic Imaging*, vol. 20, pp. 260–274, 1998.

[18] N. Otsu, "A threshold selection method from gray-level histograms," *IEEE Trans Syst Man Cybern*, vol. 9, pp. 62-66, 1979.

[19] M. Bilgen, "Target detectability in acoustic elastography," *IEEE Trans Ultrason Ferroelectr Freq Control*, vol. 46, pp. 1128-1133, 1997.

CHAPTER IV

MANUSCRIPT 3: PRELIMINARY TESTING OF SENSITIVITY TO INPUT DATA QUALITY IN AN ELASTOGRAPHIC RECONSTRUCTION METHOD

Jao J. Ou, Stephanie L. Barnes, Michael I. Miga

Department of Biomedical Engineering, Vanderbilt University, Nashville, TN, 37235

This manuscript has been published in the proceedings of *IEEE International Symposium on Biomedical Imaging*, IEEE Press, pp. 948-951, February 2007

Abstract

An elastographic reconstruction method has been developed to recover the material properties of soft tissue by model-based analysis of image data acquired at different states of mechanical loading. The algorithm utilizes image similarity as part of the cost function for a multi-resolution, non-linear optimization. Previous work with a phantom membrane used for simulated dermoscopic application has prompted this preliminary investigation of the relative effects of additive image noise and boundary condition determination errors on the performance of the method. The results as quantified by elasticity contrast and localization accuracy indicate that the reconstruction process is robust in the presence of realistic levels of image corruption and tolerates the majority of boundary condition mapping errors.

Introduction

The practice of palpating soft tissue structures in the course of the physical exam for assessing tissue health has had a long-standing clinical history of providing correlation between improper stiffness and pathology. The ability to characterize the mechanical properties of tissue is therefore a potential source of information relevant for both diagnosis and prognosis. One way in which this could be achieved in a non-invasive manner is through analysis of tissue deformation with imaging and image processing techniques, which is a central goal of the field of elastography [1].

The conceptual framework for our elastographic reconstruction has been previously described in [2-4]. In brief, images of a tissue of interest are acquired in an initial (*source*) and then mechanically loaded state (*target*). The source image is deformed by a prescribed computational model and compared to the target. This is repeated in an iterative process using updates to the elasticity parameters of the model as generated by a multi-resolution, non-linear optimization scheme in order to achieve a suitable match in image similarity. Because the goal of the reconstruction is to determine a spatial mapping of tissue elasticity, this process can also be classified as an inverse problem.

Our observations during the ongoing development and testing of this method have prompted questions concerning the quality of data necessary and sufficient to achieve satisfactory results (i.e. fidelity of the reconstructed

elasticity image). The primary inputs to the reconstruction method are the acquired images and the delineated boundary conditions on the region of interest. While it is clearly preferable to have idealized data, in reality, both inputs involve varying levels of manual interaction. As an initial study, we have sought to test the effects of degradation in data quality on the end reconstruction by using additive image noise and randomized boundary condition selection error.

Methods

Elastographic Reconstruction Framework

There are three major components in the reconstruction framework: a biomechanical model of tissue response to applied deformation, a method of image comparison, and an optimization scheme. For the current version, a continuum-based model of mechanical equilibrium using isotropic Hookean linear elasticity with a plane stress approximation is employed [5]. This allows for a reduction of the general 3D formulation of Cauchy's Law to the two parameters of Young's modulus and Poisson's ratio in 2D. The displacement solution of the finite element representation of the model, solved using the standard Galerkin method of weighted residuals [6], is then applied to the nodes of a simple triangular mesh based on the source image domain in order to perform image deformation. The mesh is partitioned by K-means clustering (MATLAB R14, Mathworks, Nattuck, MA) into *N* number of *regions*, each of which describes a distinct set of homogeneous elastic properties for a grouping

of adjacent elements. This allows for implementation of the multi-resolution approach by creating a hierarchy of increasingly finer spatial distributions of elasticity parameters, which has been shown to be an improvement upon previous versions using only a single resolution [2,3]. A second discretization is performed to divide the target image into *M* number of rectangular *zones* containing approximately equal numbers of pixels. The deformed source image is compared to the target using an intensity-based image similarity metric (here, the correlation coefficient [7]) in the evaluation of the least squares error objective function

$$\sum_{m=1}^{M}(S_{TRUE} - S_{EST})^2 \qquad (1)$$

where S_{TRUE} is an *Mx1* vector of the (maximum) similarity values achieved when comparing the target image to itself and S_{EST} is the *Mx1* vector of similarity between the target and model-deformed source image created using current estimates of the elastic modulus distribution. It should be noted that S_{TRUE} has by definition a value of 1 for the correlation coefficient.

The minimization of equation (1) using a Levenberg-Marquardt approach takes the form

$$\left[J^T J + \alpha I\right]\{\Delta E\} = \left[J^T\right]\{S_{TRUE} - S_{EST}\} \qquad (2)$$

where **J** is the Jacobian matrix of size *M*x*N* estimating $\partial S/\partial E$, ΔE is the *N*x*1* vectors of updates to the current elasticity values, and α is the scalar regularization term for the Hessian matrix as described in [8].

Material Preparation and Image Acquisition

For our simulation purposes, a two-material skin phantom had been previously constructed [2] as a thin membrane measuring 15 cm x 15 cm, with a single 5-cm circular stiff inclusion embedded in the center (Figure 20). The phantom was manufactured with Smooth-On™ polyurethanes (Smooth-On, Easton, PA) Evergreen 10 and Evergreen 50. These materials have essentially indistinguishable colors but vary significantly in their elastic modulus values, so the former was used as the bulk material and the latter for the inclusion. Based on material testing, the expected contrast ratio of Young's modulus values was determined to be approximately 5.7:1. A black permanent marker was used to place a pattern of regularly spaced (~1 cm) grid lines on the membrane. The membrane was clamped along two opposite edges and then stretched in a uniaxial fashion by means of a milling vise. A commercial webcam (Logitech QuickCam Pro 4000) was mounted above the assembly to acquire image pairs of the membrane in pre- and post-stretched states (960 x 1280 pixel resolution, 8-bit grayscale).

Reconstruction Experiments

Based on prior work, a data set consisting of a particular image pair and associated boundary conditions known to produce a satisfactory reconstruction was designated as the gold standard for the remainder of the experiments (Figure 20). In order to test the effect of increasing amounts of additive noise on the reconstruction algorithm, Gaussian random fields of 1, 5, 10, 15, 20, 25, and 30% noise were applied to the base target image in three separate trials. This presents a challenge that ascertains the ability of the similarity metric and objective function to discern a proper match.

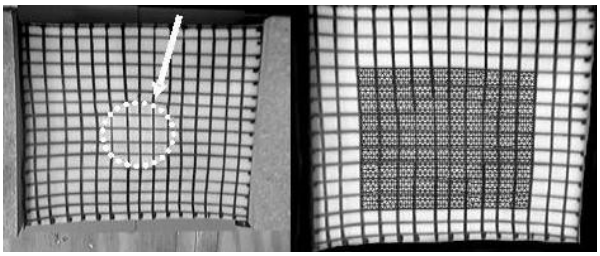

Figure 20. Experimental phantom membrane system (left) and input image with overlaid finite element mesh (right). The inclusion location is indicated by the arrow and dotted line. The mesh designates the actual region reconstructed.

The current method for selecting Dirichlet boundary conditions on the finite element mesh is semi-automated and requires the user to make a final determination on point correspondence. The second experiment was intended to simulate the targeting error of the user (e.g. visual cues and input device control). Each test involved applying randomized vectors of equal magnitude to alter the boundary conditions of the gold standard data set. Errors of 0.1, 0.2, 0.3, 0.5, 0.75, 1.0, 1.5, and 2.0 mesh units (scaled to be equivalent to pixel

coordinates) were used in two separate trials for a total of 16 reconstructions. Sub-pixel magnitudes were included after determining that the accuracy of selecting a feature point in the image/mesh was typically less than or equal to 0.5 units for users ranging from moderate to expert skill.

For all reconstructions, resolutions progressing through N = 16, 36, 64, 144, 256, and 400 regions and M = 9 similarity zones were used; domains were initialized to homogeneous elasticity and Poisson's ratio held constant at 0.485 to represent nearly incompressible material(s).

Reconstruction Analysis

The final reconstructed elasticity values were modeled as a mixture of two Gaussian distributions, and a threshold was established to maximize inter-class variation [9] and subsequently classify each region as bulk or stiff material. Because Dirichlet boundary conditions are exclusively used in these reconstructions, the method is only sensitive to relative differences in elasticity. The quantities used in evaluating reconstruction success are the elasticity contrast ratio, localization accuracy of the inclusion, and an overall measure designated the 'quality of reconstruction score' (QRS). The elasticity contrast ratio (CR) was calculated from the mean values of the two material classes, and the positive predictive value of identifying stiff material within the independently segmented boundary of the inclusion gives a measure of localization accuracy (LA). The quality of reconstruction is simply then the

product QRS = CR*LA, which allows the user to consider the other two measures in conjunction.

Results

Figures 21 and 22 show examples of reconstructions achieved under various image noise and boundary condition errors, and individual localization errors and contrast ratio values are listed in Table 5. Note that the data for the image noise experiment was averaged from the three trials, and that the data presented for the boundary condition experiment is from one [representative] trial. Figure 23 is a plot of the reconstruction quality decreasing with increasing image noise, and Figure 24 shows the reconstruction quality trend plotted against the change in initial alignment error (detailed in the following section) relative to that of the gold standard.

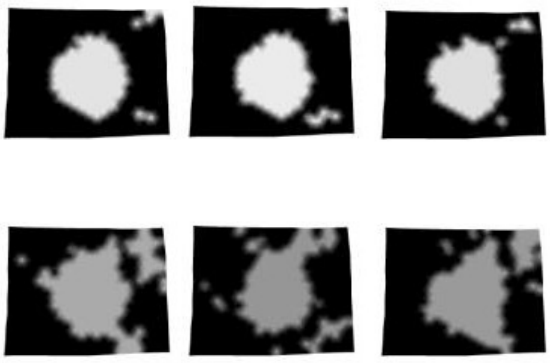

Figure 21. Representative reconstructions with image noise. From top left: 1, 5, 10, 20, 25, and 30% additive Gaussian noise. The reconstructions are visualized as two materials, with whiter areas indicating higher elasticity contrast values.

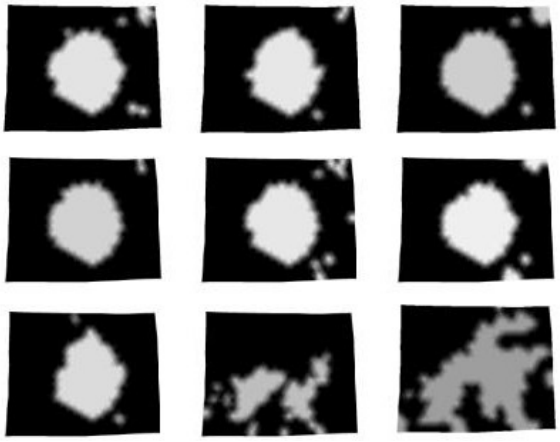

Figure 22. Representative reconstructions with boundary condition error. Left to right: 0.1, 0.2, 0.3 units (top row); 0.75, 1.0, 2.0 units (middle row, trial #1); 0.75, 1.0, 2.0 units (bottom row, trial #2). Error magnitudes greater than or equal to 0.5 mesh units are not accurate predictors of reconstruction quality.

Table 5. Reconstruction quality under noise conditions

Additive image noise							
% Noise	1	5	10	15	20	25	30
LA	0.92	0.90	0.91	0.70	0.69	0.66	0.56
CR	3.56	3.45	3.45	3.24	2.88	2.83	2.68

Gold standard: LA = 0.95, CR = 3.60

Boundary condition error								
Err	0.1	0.2	0.3	0.5	0.75	1.0	1.5	2.0
AE	0.96	3.32	2.21	102	0.93	32.2	12.6	7.66
LA	0.87	0.92	0.88	0.59	0.94	0.86	0.86	0.96
CR	3.63	3.68	3.44	2.91	3.46	3.71	3.78	3.30
CR = elasticity contrast ratio, LA = localization accuracy AE = initial alignment error (%), Err = error magnitude.								

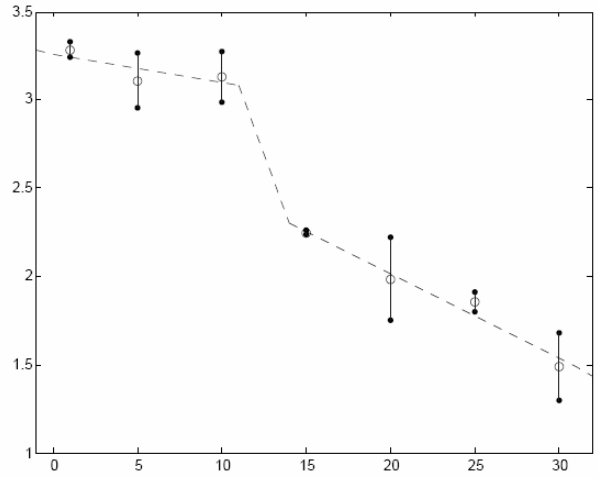

Figure 23. Reconstruction quality vs. percent additive image noise. The drop-off after 10% additive noise indicates the threshold of tolerance for the method.

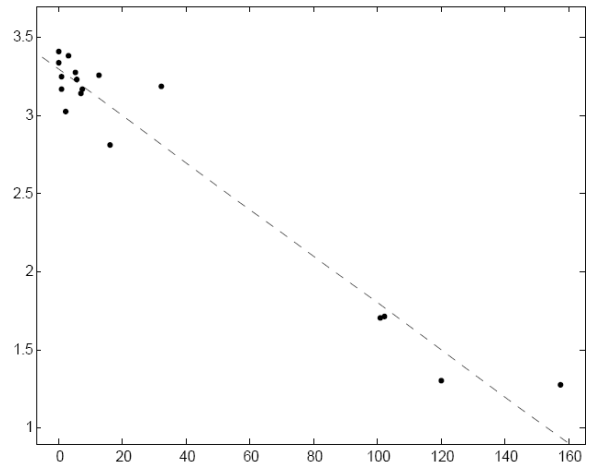

Figure 24. Reconstruction quality vs. percent change in initial alignment relative to gold standard. The majority of errors tested produced satisfactory reconstructions.

Discussion

From visual inspection of Figure 21, it is apparent that the achieved reconstruction becomes more inaccurate with increased image noise. However, the ability to identify and localize the stiff inclusion is not significantly impaired until a noise field of greater than 10% is applied. The threshold was found by determining which level of noise provided the best minimum sum squared error fit of two lines to the distribution of reconstruction quality in Figure 23. This would indicate that the similarity metric and objective function are robust to intensity deviations of about 6 gray levels. While Gaussian noise is one of several possible types and may not always be an ideal model, it is still relevant to acquisition inaccuracy and corruption processes that may be encountered across several medical imaging modalities. The use of an intensity-based similarity metric appears to give the method an advantage in being generally insensitive to reasonably expected amounts of image noise.

Figure 22 demonstrates that because of the random nature of the boundary condition errors, the magnitude is itself not an accurate indicator of reconstruction quality. This necessitated the introduction of a more suitable parameter that accounts for the net effect of the altered boundary conditions in order to perform fair evaluations. In essence, randomizing the vectors at every node causes the optimization to use an unpredictable starting pose and increases its chance of converging to an improper minimum. Therefore, the 'initial alignment error' (AE) is defined as the relative percent change between the objective function evaluation using the gold standard boundary conditions

and those of the test case. An as example, it could be assumed that vectors of magnitude 0.5 would be a much more tolerable error than 2.0, but it is the significantly larger AE of the former that actually predicts the poor outcome. However, it should also be noted (results not shown here) that even if the same set of error vectors are scaled over varying magnitudes, there is no clear trend in alignment error or reconstruction quality. This appears to imply that certain boundary nodes, most likely those in the direction of largest strain, have a greater effect on reconstruction and merit particular care in selection. Other factors influencing unfavorable reconstructions are most likely nonlinear effects not predicted by the current model as well as an inherent lack of discrimination by intensity-based similarity metrics in analyzing the regularity of the imposed grid pattern. Nevertheless, for the error magnitudes tested that best approximate realistic inaccuracies (i.e. <0.5 units), the alignment errors were small and quality of the end reconstruction was seen to be quite good. This qualitatively validates the current method of determining point correspondence as a reasonable procedure with an accommodating margin (factor of four) in light of typical user interaction.

Conclusions

In this work, we have presented a method for recovering elasticity parameters from image data of thin membrane structures by maximizing the image similarity between two different states of mechanical loading within the context of an inverse problem. The biomechanical model, multi-resolution

optimization, and image acquisition are each modular components of this elastographic reconstruction framework, making it extensible to added sophistication. Tests were conducted to examine the tolerance of the method to degraded or improper inputs. The results indicate that the gold standard data set was mostly optimal for obtaining a successful reconstruction. Widening disparities in either image data or boundary condition selection from that in the gold standard caused observable trends of declining reconstruction quality. Based on these observations, it appears that the method handles most expected variations encountered in image acquisition as well as the majority of typical user inaccuracies. Because there are complicated effects associated with mapping of the Dirichlet boundary conditions in constraining the displacement solution of the model, further study on inter-rater variability in selection as well as comparisons with more automated point correspondence methods is ongoing.

Acknowledgments

This work was supported in part by a Whitaker Foundation Young Investigator Continuation Award and the Congressionally Directed Medical Research Program – Breast Cancer Research Program Pre-doctoral Fellowship.

References

[1] J. Ophir, I. Cespedes, H. Ponnekanti, Y. Yazdi, and X. Li, "Elastography - a quantitative method for imaging the elasticity of biological tissues," *Ultrasonic Imaging*, vol 13, pp. 111-134, 1991.

[2] M.I. Miga, M.P. Rothney, J.J. Ou, "Modality-independent elastography (MIE): potential applications for dermoscopy," *Medical Physics*, vol 32 pp. 1308-1320, 2005.

[3] C.W. Washington, M.I. Miga, "Modality independent elastography (MIE): a new approach to elasticity imaging," *IEEE Trans Med Imaging*, vol 23, pp. 1117-1128, 2004.

[4] M.I. Miga, "A new approach to elastography using mutual information and finite elements," *Phys Med Biol*, vol 48, pp. 467-480, 2003.

[5] Boresi, A., *Elasticity in Engineering Mechanics*, Wiley-Interscience, 2000.

[6] Lapidus, L., and G.F. Pinder, *Numerical Solution of Partial Differential Equations in Science and Engineering*, John Wiley & Sons, 1982.

[7] Fitzpatrick, J.M., Hill, D.L.G., and C.R. Maurer, "Image registration," *Handbook of Medical Imaging, Volume 2*. SPIE Press, pp. 447-513, 2000.

[8] N. Joachimowicz, C. Pichot, J.P. Hugonin, "Inverse scattering: an iterative numerical method for electromagnetic imaging," *IEEE Trans Biomed Engineering*, vol 39, pp. 1742-1752, 1991.

[9] N. Otsu, "A threshold selection method from gray-level histograms," *IEEE Trans Syst Man Cybern*, vol 9, pp. 62-66, 1979.

CHAPTER V

MANUSCRIPT 4: EVALUATION OF 3D MODALITY INDEPENDENT ELASTOGRAPHY FOR BREAST IMAGING: A SIMULATION STUDY

Jao J. Ou[1], Rowena E. Ong[1], Thomas E. Yankeelov[1,2,3,4], and Michael I. Miga[1,2,3]

[1]Vanderbilt University, Department of Biomedical Engineering, Nashville, TN 37235, USA

[2]Vanderbilt University Medical Center, Department of Radiology and Radiological Sciences, Nashville, TN 37232, USA

[3]Vanderbilt University Institute of Imaging Science, Nashville, TN 37232, USA

[4]Vanderbilt University, Department of Physics and Astronomy, Nashville, TN 37235, USA

This manuscript has been published in *Physics in Medicine and Biology*, Vol. 53, No. 1, January 2008

Abstract

This paper reports on the development and preliminary testing of a three-dimensional implementation of an inverse problem technique for extracting soft tissue elasticity information *via* non-rigid model-based image registration. The modality independent elastography (MIE) algorithm adjusts the elastic properties of a biomechanical model to achieve maximal similarity between images acquired under different states of static loading. A series of simulation experiments with clinical image sets of human breast were performed to test the ability of the method to identify and characterize a radiographically occult stiff lesion. Because boundary conditions are a critical

input to the algorithm, a comparison of three methods for semi-automated surface point correspondence was conducted in the context of systematic and randomized noise processes. The results illustrate that 3D MIE was able to successfully reconstruct elasticity images using data obtained from both magnetic resonance and X-ray computed tomography systems. The lesion was localized correctly in all cases and its relative elasticity found to be acceptably close to the true values. In addition, the inaccuracies of surface registration performed with thin-plate spline interpolation did not exceed empiric thresholds of unacceptable boundary condition error.

Introduction

Breast cancer is the most common cancer of women in the United States, the second most common cause of cancer death in women, and the leading cause of death in women ages 45 to 55. Estimates for the year 2007 indicate that 178,480 American women will be diagnosed with the disease and 40,910 women will die from it (ACS, 2007). While many advances have been made in the treatment of the disease, the ability to detect its presence for either screening or diagnostic purposes remains an area of active research involving many novel forms of imaging. The characterization of the mechanical properties of breast tissue is an important potential source of clinical information because of the long-standing association of palpable differences in stiffness with possible pathological states. A minimally invasive methodology for analyzing tissue elasticity through imaging and/or image processing

techniques is a central goal of the field of elastography (Parker *et al.*, 2005), with the application of various techniques being found not only in the interrogation of the breast (McKnight *et al.*, 2002; Melodelima *et al.*, 2006; Sinkus *et al.*, 2000), but also skin (Miga *et al.*, 2005; Tsap *et al.*, 1998; Zhang *et al.*, 2004), prostate (Curiel *et al.*, 2005; Egorov *et al.*, 2006), and other accessible organ systems.

Many of the current elastography methods are founded in ultrasound (US) (Ophir *et al.*, 1991; Ophir *et al.*, 2000) and magnetic resonance (MR) (Manduca *et al.*, 2001; Muthupillai *et al.*, 1995) imaging and involve the estimation of induced displacements within the tissue of interest to infer the elasticity distribution. We have recast the problem as a physically-constrained, non-rigid image registration utilizing numerical models of static deformation with image similarity metrics to reconstruct the spatial distribution of elasticity parameters. This technique has been termed 'modality-independent elastography' (MIE) (Miga, 2002, 2003; Washington and Miga, 2004) because of its ability to handle anatomical images from different sources with relatively simple modifications to the acquisition procedure. To date, data from MR, X-ray computed tomography (CT), and digital photography have been used to successfully drive the algorithm in two-dimensional (2D) work. Others have also pursued similar approaches within the context of ultrasound elastography (Garra *et al.*, 1997; Gokhale *et al.*, 2004; Sarvazyan *et al.*, 1995), optical image analysis (Tsap *et al.*, 1998), and to a lesser degree magnetic resonance elastography (Fowlkes *et al.*, 1995). While the use of MIE in 2D has been

illuminating for algorithmic development and may have its own applications in studying the more planar system of the skin, ultimately, translation of the method to utilize volumetric data is desirable (if not necessary) in order to provide an accurate representation of organs such as the breast as a whole. In this work, we present a newly realized three-dimensional (3D) version of MIE along with simulation experiments to evaluate its performance. In addition, some potential effects of degraded input quality are addressed by examining robustness of the algorithm to inaccuracies in specified boundary conditions and then comparing the reconstruction fidelity of three different techniques developed for semi-automatic generation of boundary conditions.

Methods and Materials

MIE reconstruction framework

The conceptual framework for our elastographic reconstruction has been previously described in (Miga, 2002, 2003; Miga *et al.*, 2005; Washington and Miga, 2004). To review, an image of a tissue of interest (*source*) is deformed by a biomechanical model and compared against an acquired image of the same tissue in a mechanically loaded state (*target*). Iterative updates of elasticity parameters to the model are performed until a suitable match in image similarity is achieved in a least squares manner to satisfy a non-linear optimization scheme. This process as illustrated in Figure 25 can be classified as an inverse problem, with model-based deformation and registration of the source image representing the forward problem.

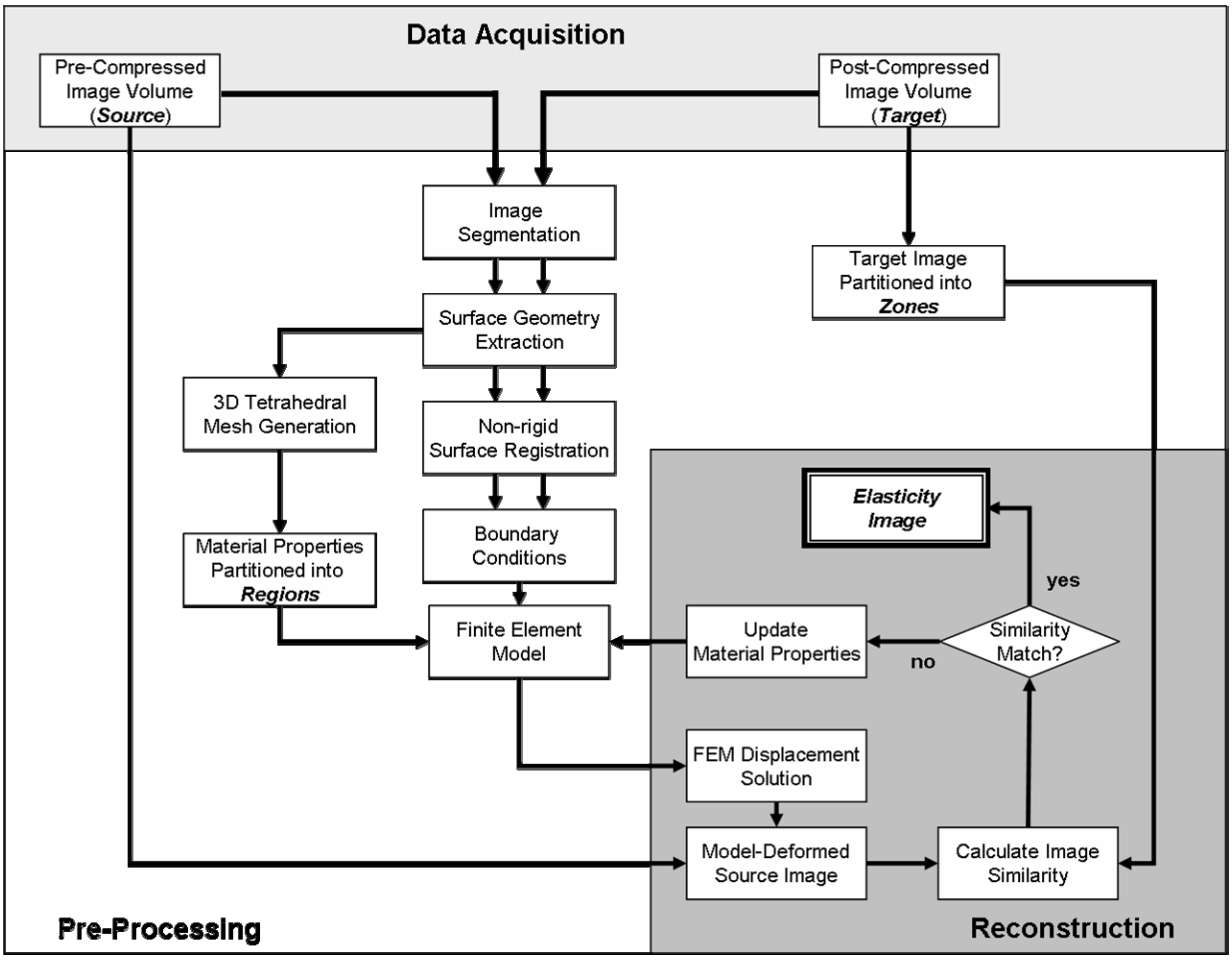

Figure 25. Schematic of MIE framework. After acquisition of image data, surface representations are segmented from the pre- and post-deformation volumes (*source* and *target*, respectively). A number of pre-processing steps are performed to generate boundary conditions for the biomechanical model, which produces a deformed image that can be compared with the true target volume. The optimization routine updates the elasticity distribution until the best similarity is achieved.

The three major components of the reconstruction algorithm are the biomechanical model, image comparison, and optimization. Although there are a number of models for soft-tissue mechanics, it is reasonably appropriate to begin with a general elastic body. The partial differential equation that expresses a state of mechanical equilibrium is

$$\nabla \cdot \sigma = 0 \tag{1}$$

where σ is the Cartesian stress tensor (Boresi and Chong, 1999). We have elected to describe the constitutive tissue behavior using Hooke's Law of linear elasticity, which states that the strain is proportional to the applied stress, and further assume that materials are isotropic and nearly incompressible in nature. The description of the constitutive relationship between stress and strain is ultimately expressed in terms of the elasticity parameters *E* (Young's modulus) and ν (Poisson's ratio).

A finite element representation of the model is constructed from the source image. Elements of the mesh are grouped using a K-means algorithm by initializing a number (*N*) of seed points that are the centers of the clusters and iteratively minimizing their summed distance to all element centroids in the mesh. This process defines a set of nearly equally-sized but spatially non-uniform *regions* that are homogeneous with respect to their material properties and establish the 'resolution' of the reconstructed elasticity image. After assigning appropriate boundary conditions based on estimated displacement or stress, the standard Galerkin method of weighted residuals (Lapidus and Pinder, 1982) is used to construct a matrix system. The solution of that system yields displacements that are used to deform the source image. A second discretization is performed by binning the target image into *M* groups of contiguous voxels termed *zones*. The model-deformed image is then compared to the target by summing the similarity metric evaluated for all zones. The

correlation coefficient (Fitzpatrick *et al.*, 2000) is used throughout this work as it has empirically demonstrated better performance for our method over other intensity-based metrics such as the sum of squared differences and normalized mutual information. Optimization of the elasticity parameters is taken as the minimization of the objective function

$$\Psi = \left| S_{TRUE} - S_{EST} \right|^2 \tag{2}$$

where S_{TRUE} is the set of similarity values achieved when comparing the target image to itself, S_{EST} is the similarity between the target and model-deformed source images using current estimates of the elastic modulus distribution, and $|\bullet|$ denotes the vector L^2-norm. Note that by definition, S_{TRUE} for the correlation coefficient has a constant value of 1. Differentiating (2) with respect to the elasticity distribution and setting the resulting expression equal to zero generates a series of nonlinear equations that can be solved using the Levenberg-Marquardt method,

$$\begin{aligned} \left[J^T J + \alpha I \right] \{\Delta E\} &= \left[J^T \right] \{S_{TRUE} - S_{EST}\} \\ \alpha^2 &= \lambda \left[\frac{1}{N} \sum_{i=1}^{N} (J^T J)_{ii} \right] \Psi^2 \end{aligned} \tag{3}$$

where **J** is the Jacobian matrix of size M x N, and ΔE is the vector of updates to the material property distribution defined by the regions. The regularization parameter α uses an empirical scalar factor λ as determined by the methods

described in (Joachimowicz *et al.*, 1991). Each column of the Jacobian matrix is a finite difference approximation of the change in image similarity over all zones due to the perturbation of a single material property region, such that

$$J = \frac{\partial S_{EST}}{\partial E} = \begin{bmatrix} \frac{\partial S_1}{\partial E_1} & \frac{\partial S_1}{\partial E_2} & \text{L} & \frac{\partial S_1}{\partial E_N} \\ \frac{\partial S_2}{\partial E_1} & \text{O} & & \text{M} \\ \text{M} & & \text{O} & \text{M} \\ \frac{\partial S_M}{\partial E_1} & \text{L} & \text{L} & \frac{\partial S_M}{\partial E_N} \end{bmatrix} \quad (4)$$

Modulus values contained in E are updated by ΔE until an error tolerance on the relative objective function error evaluation is reached or a maximum number of iterations are completed. Spatial averaging of elasticity values in the model and solution relaxation between iterations are also utilized to improve the stability of the optimization.

Parallel computing framework

The transition of this method from 2D to 3D entails a much higher computational overhead that affects all parts of the reconstruction. The mesh needed to describe the entire breast as opposed to a single slice is at least 20-40 times greater in the number of structural components (nodes and elements), and the model must account for an additional degree of freedom. The resulting system of equations to be solved is thus nearly two orders of magnitude larger. The finite difference approximation of each column of the Jacobian matrix requires a "forward solve" consisting of the biomechanical

model, image deformation, and evaluation of the similarity metric. Because this must be done for every elasticity region, attempting to adequately sample the spatial domain makes the building of this matrix the primary expenditure of computing resources.

In order to achieve a reasonable level of performance, the Message Passing Interface standard for parallel processing is used to distribute formation of the Jacobian among a number of communicating nodes controlled within a static SPMD (single process, multiple data) scheme. The Portable Extensible Toolkit for Scientific Computation (PETSc) (Balay *et al.*, 2004; Balay *et al.*, 1997) has provided the necessary coding base for interfacing sparse matrix system solvers with our C/C++ Gauss-Newton optimization routine. This design scales readily to the number of processors available; it has been tested on a homogeneous cluster of eighteen processors (2.0 GHz Pentium4 Xeon, 1GB RAM) located in the laboratory, as well as a heterogeneous cluster of hundreds of processors available through the Vanderbilt Advanced Computing Center for Research and Education project. The use of many processors is capable of producing a nearly linear speedup and otherwise agrees in principle with the performance impact suggested by Amdahl's Law (Ahmdahl, 1967).

Simulation experiment setup

For this work, a simulation experiment is defined by the creation of an idealized target image volume from a deformation achieved by specification of boundary conditions at the surface of the breast. This ensures data fidelity in

order to effectively evaluate reconstruction performance in the optimization and model characteristics. Two image volumes of human breast were made available to further test the modality independence of the algorithm. The first was obtained from a dedicated breast CT scanner (256 x 256 x 130, voxel size 0.6 mm^3) as described in (Boone *et al.*, 2006; Boone and Lindfors, 2006; Boone *et al.*, 2001), and the second from a Philips Achieva 3.0-T MR unit (256 x 256 x 98, voxel size 1.0 mm^3) using a clinically-approved transmit-receive double-breast coil to acquire a 3D T1-weighted exam with a fat-nulling inversion pulse (TR/TE/a/NEX=4.6 ms/2.3 ms/10°/1) (Yankeelov *et al.*, 2007). The surfaces of the breast were segmented (ANALYZE 6.0, Mayo Clinic, Rochester, MN) to create tetrahedral meshes composed of 39,013 nodes connected in 214,163 elements for the CT volume and 20,623 nodes and 111,142 elements for the MR volume. A 2-cm spherical tumor was synthetically implanted in the center of each mesh by assigning a stiff modulus to appropriate member elements that was six times higher than the surrounding material (Krouskop *et al.*, 1998; Samani *et al.*, 2007). Tissue deformation was performed by creating a set of displacements calculated to approximate a Gaussian stress distribution applied to a rectangular area on lateral surface of the breast. The displacements were then applied to the original volumes in order to create the desired target images. Figure 26 illustrates the setup of the simulation data.

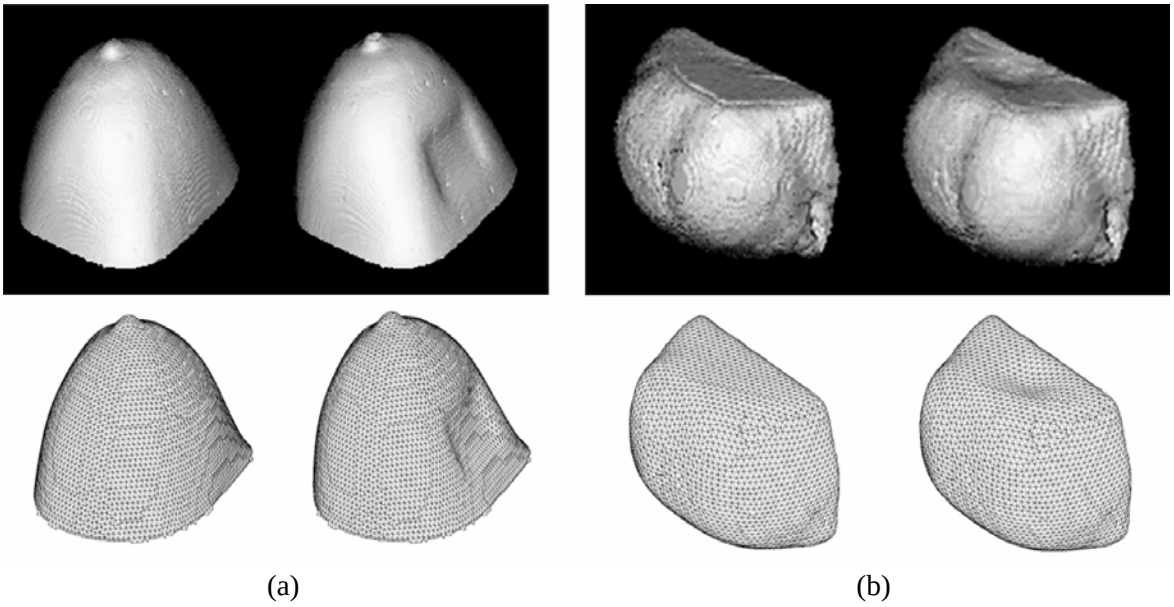

Figure 26. (a) CT data set and (b) MR data set used for 3D MIE simulations. Surface renderings of the image volumes (top row) and meshes (bottom row) are shown for the pre- (*source*) and post-deformation (*target*) scenarios.

Reconstruction experiments

Reconstructions using spatial *a priori* knowledge of the location and size of the inclusion were first performed in order to constrain the problem, as well as the computational expense of the Jacobian matrix, to a two-material discrimination of relative stiffness (elastic contrast). A second set of experiments were then used to address the viability of the method to perform a generalized detection of the lesion with no knowledge of the actual structure of the domain. To run these naïve reconstructions for the CT data set, 3180 material regions and 733 voxel similarity zones were partitioned, while in the MR data set, 3166 regions and 768 zones were used. In all cases, the reconstruction was initialized with a homogeneous elasticity distribution and

the value of Poisson's ratio held constant at ν = 0.485 to represent a nearly incompressible material.

Evaluating boundary condition influence

In addition to image acquisition, the other major input to the reconstruction algorithm is the delineation of boundary conditions on the region of interest over which the model is applied. While relatively easy to control in simulation, in a real clinical situation, this presents the challenge of accurately determining point correspondences between the source and target breast surfaces. The effect of any inaccuracies is cumulative, as errors are propagated from the model to the image deformation and finally the similarity measurements. In previous 2D work, manual delineation of boundary conditions was possible with guidance and correction using standard computer input devices (*i.e.* a mouse). However, the increased complexity of mesh geometry in 3D necessitates a more automated technique of determining correspondence between two surfaces. Potentially non-trivial random and/or operator-dependent noise is introduced into the generated boundary conditions. Therefore, the following experiments were performed to examine the ability of the algorithm to tolerate various types of mis-mappings.

Robustness to randomized boundary errors

The gold standard boundary conditions used to create the simulated target image volumes were deliberately disrupted to examine the effect of

random noise on reconstruction fidelity. A series of magnitudes ranging from 0.01 to 2.0 voxel units (mesh coordinates normalized by their respective spacing in image space) were applied to the CT and MR data sets. Therefore, every boundary position is displaced by the same amount but in a completely unpredicted manner, as illustrated in Figure 27. These altered boundary conditions sets were utilized in the reconstruction of the *a priori* two-material test case, and the tolerance of the method was evaluated by calculating the average reconstructed elasticity contrast ratios over four trials of each level of noise, with deviations less than 20% from the true stiffness being deemed acceptable.

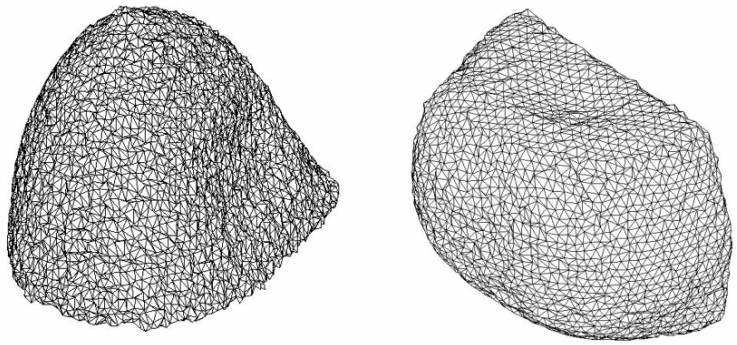

(a) (b)

Figure 27. Examples of distortion due to additive randomized error. For effect, noise of 2.0 voxel units is shown as applied to the gold standard boundary condition set for CT (a) and MR (b). At these extreme levels, the smooth surface of the breast as originally captured in Figure 26 is completely lost, and the forced reconfiguration of internal elements in the finite element mesh adversely affects all aspects of the reconstruction.

Feasibility of automated boundary condition generating methods

Three methods of surface registration and point correspondence were considered as the basis of a semi-automated method for determining boundary conditions input to the reconstruction algorithm. Two were specifically developed for this work by attempting to use potential energy distributions derived from classic partial differential equations (PDEs) for surface matching, and the other is a free-form geometrical warping.

If the flow of a hypothetical substance over both the source and target breast surfaces is taken to be a conserved process and modeled using potential theory, correspondence can be assigned by matching areas of similar energy deposition, that is, the equivalent level sets. The algorithm for the PDE-based surface matching methods can be summarized in the following steps:

1. *Determine an energy distribution for each surface.* Laplace's equation is commonly used to describe the steady-state distribution of potential energy Φ in a system:

$$-\nabla^2\Phi = 0 \tag{5}$$

Similarly, the diffusion equation describes the temporal change in potential over a region:

$$\frac{\partial\Phi}{\partial t} = D\nabla^2\Phi \tag{6}$$

where *D* is the diffusion coefficient. Each PDE is solved over both breast surfaces (source and target). For both equation (5) and (6), the nipple is

assigned as an area of high potential energy. Additionally, with equation (5), nodes at the chest wall are assigned a value of 0 in order to obtain a non-trivial solution, whereas the propagating front produced by (6) is artificially halted at the chest wall boundary. While both PDE solutions similarly establish an energy gradient over the breast surfaces, their application in the following steps results in more apparent differences.

2. *Determine correspondence between energy distributions.* From the solution of the PDEs on the source surface, a series of spatially distributed isocontours representing distinct potentials are determined. For each level set, an isocontour of equivalent potential energy is found on the target surface, and the two curves matched according to the symmetric closest point method described by (Papademetris *et al.*, 2002).

3. *Generate boundary conditions.* By extracting a number of isocontours of different values, the resulting point correspondence vectors define a relatively dense three-dimensional displacement field. The displacement for each boundary node can then be interpolated from the set of its nearest neighbors.

The final method employs thin-plate splines (Goshtasby, 1988) to generate a set of boundary conditions. In this well-established method of non-rigid transformation, a number of control points with known correspondences establish constraints on the deflection of a hypothetical thin sheet of material in order to best warp the two surfaces together. Displacements at each

boundary node are then simply interpolated from the calculated fit. For these simulation experiments, a subset of boundary nodes was used to represent physical markers on the breast surface. Forty points were uniformly distributed over the CT mesh and eighty for the MR mesh in order to handle the more highly variegated shape of the latter data set.

The automated methods were initially evaluated according to their target registration error (TRE), which was calculated as the average Euclidean distance between the generated and true boundary conditions. Because the deployment of these fits represents a more correlated form of noise, these boundary conditions were also applied to the two-material scenario, and the reconstructed elasticity contrast values compared to the trials of additive randomized error for which the magnitude was approximately equal to the TRE. Finally, a mapping of the objective function space was performed by calculating the similarity values for model-based image deformations over a range of elasticity contrasts from 0.5:1 to 30:1. An interpolating curve was fit to extract the minimum objective function value and associated contrast ratio to determine a theoretical optimal reconstruction as constrained by the estimated boundary conditions.

Results

MIE reconstructions

Because the use of *a priori* spatial information about the inclusion limits the reconstruction to a two-material system, the fidelity of the reconstruction

is simply evaluated by examining the elastic contrast between the inclusion and the normal tissue of the breast (ideal of 6:1). Figure 28 demonstrates the behavior of the algorithm in optimizing the objective function while successfully characterizing the stiffness of the inclusion to within 5% of the actual value (6.02:1 and 6.21:1 for the CT and MR data sets, respectively).

The fidelity of the generalized reconstruction experiments (using no *a priori* knowledge of the domain) was primarily evaluated on its ability to detect the presence of an inclusion based on classification of the material property distribution as well as the retrospective accuracy of localizing the lesion. The final elasticity values were treated as a Gaussian mixture of two classes and separated by a threshold established *via* the method described in (Otsu, 1979). The likelihood of discriminating a lesion in the resulting elasticity image was found using the contrast-to-noise ratio (CNR) as defined by (Bilgen, 1999; Doyley *et al.*, 2003):

$$CNR = \sqrt{\frac{2(\mu_L - \mu_B)^2}{\sigma_L^2 + \sigma_B^2}} \tag{7}$$

where μ and σ^2 are the sample mean and variance of a material property distribution and the subscripts *L* and *B* denote the lesion and normal material types, respectively. As a quantitative assessment of the localization of the lesion, the positive predictive value of correctly identifying a lesion material within the known segmented region of the inclusions was also calculated as a 'quality of reconstruction score' (QRS). This value is significant because

identification of the lesion border and material classification are done independently, so user knowledge of the test scenario does not influence the performance of the measure. The 'true positive' (TP) elements of the mesh are counted as the number correctly identified as tumor and lying within the known segmentation of the lesion, while the 'false positive' (FP) elements are those identified as tumor but in an incorrect location. Thus, the calculation of QRS is simply TP/(TP+FP). Cutoffs for successful detection and localization were set at CNR≥2.2 as noted by (Doyley *et al.*, 2003) and QRS≥80% as empirically determined by a prior study in 2D MIE work (Ou *et al.*, 2006a, b), and both the CT and MR reconstructions successfully identified the embedded lesions according to these criteria (see Table 6).

The peak modulus contrast value of a reconstruction was calculated by taking the ratio of the average elasticity for manually selected homogeneous regions of approximately equal area known to be representative of the two materials. As reported in Table 6, the characterization of the relative stiffness is less than the true elasticity contrast by nearly a factor of three in both cases. This reveals a difficulty with large inverse problems in 3D where a need for reasonable performance can lead to a tradeoff in accuracy. By choosing approximately 3,200 regions to cover the domain of the breasts for the naïve reconstructions, the number of degrees of freedom presented to the optimization scheme is quite high. However, this is also relatively coarse in the sense of visualizing the reconstruction, as it roughly corresponds to a 15x15x15 image volume. Because the elasticity regions do not conform

perfectly to the actual lesion borders and furthermore are comprised of both tumor and healthy tissue, it seemed reasonable to surmise that in this mis-estimation of spatial extents, the algorithm was forced to attempt a best-fit compromise. To test this hypothesis, we agglomerated all regions in the original partitioning that overlapped the tumor and then ran the reconstruction again as a two-material characterization. Upon inspection, this regrouping was clearly a larger entity than the tumor itself (closer to 3 cm in diameter) and resulted in a shift of the global optimum to a lower elasticity contrast. In effect, the model reacted to this new, oversized tumor by reducing its stiffness in order to achieve the proper image similarity match. When viewed in light of this analysis as summarized in Table 6, the elasticity contrast found by the naïve reconstruction is then actually quite accurate.

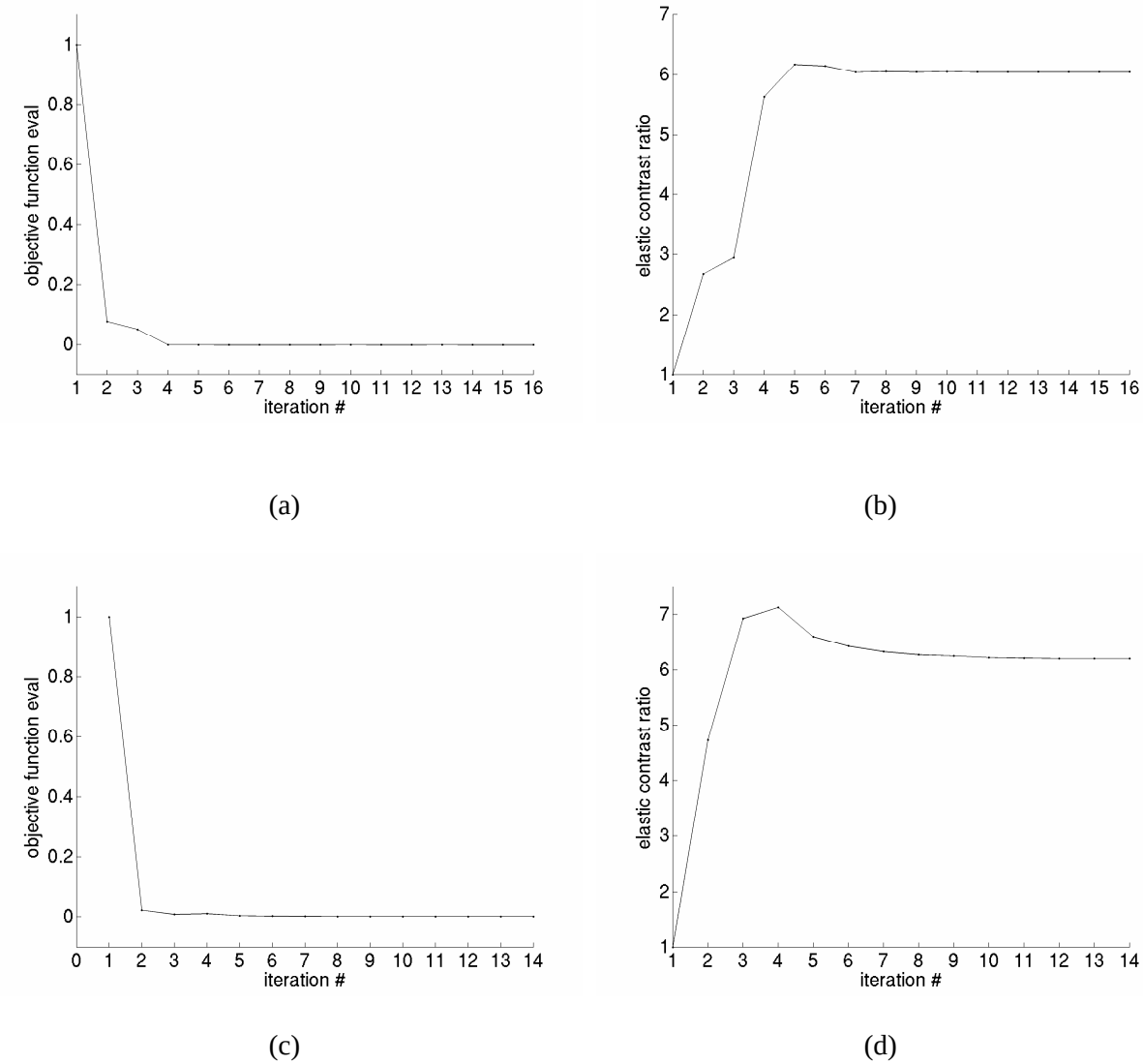

Figure 28. Optimization behavior of reconstructions using *a priori* knowledge of the inclusion location. For the CT simulation, the objective function evaluation (normalized to the initial dissimilarity value of a homogeneous elasticity distribution) and elastic contrast over several iterations of the algorithm are shown in panels (a) and (b), respectively. Similarly, this behavior for the MR data set is displayed in (c) and (d). In each case, the minimum value is achieved quickly and stably, with the corresponding contrast ratio matching the true value of 6:1 very closely (6.02:1 and 6.21:1 for CT and MR, respectively).

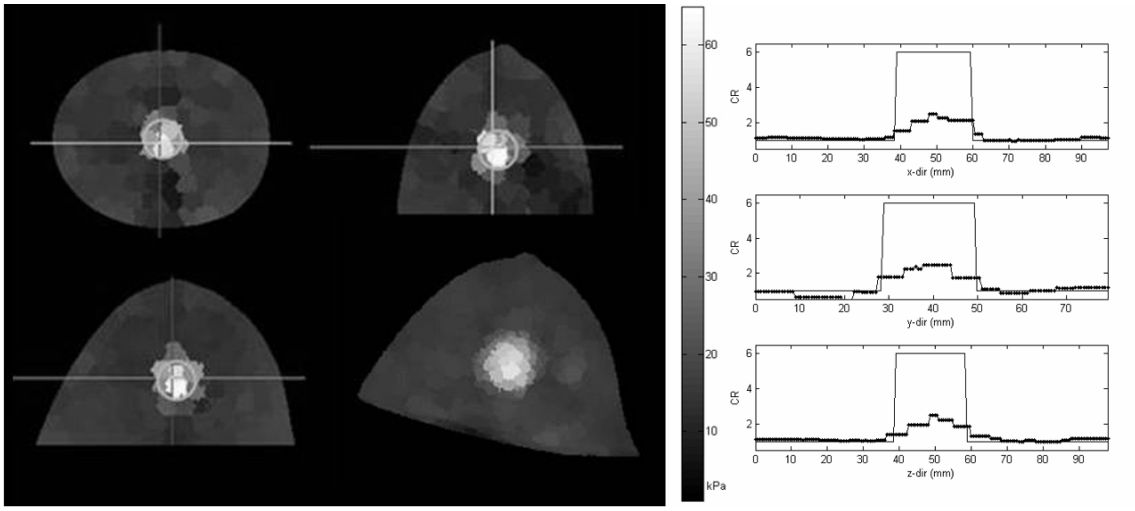

Figure 29. Reconstruction used for lesion detection in the CT data set. (a) Orthogonal views taken through the center of the elasticity image volume are shown along with a projection surface rendering (lower right). The simulated inclusion implanted in the mesh is visually distinguished from surrounding tissue. The colorbar indicates the range of elasticity values (~7-42 kPa) designated by the reconstruction, with higher (stiffer) values shown in the white end of the grayscale mapping. (b) Transect plots through the center of the volume along the cardinal directions show the profile of elasticity contrast (dotted lines) overlaid by the true profile of the simulation (solid lines).

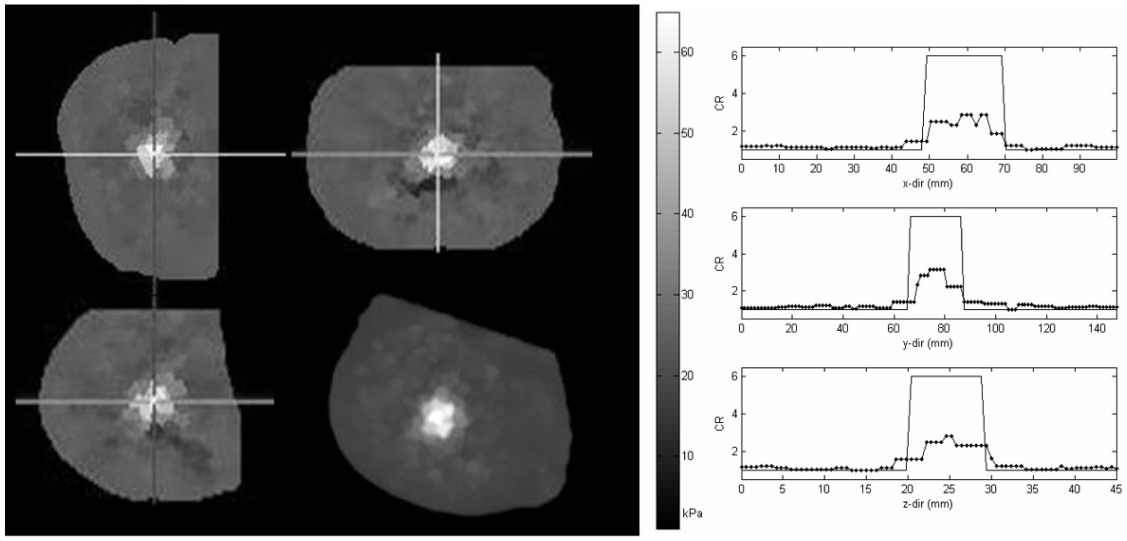

Figure 30. Reconstruction used for lesion detection in the MR data set. (a) Orthogonal views taken through the center of the elasticity image volume are shown along with a projection surface rendering (lower right). Once again, the inclusion appears to have a recognizably different elasticity, with values on the colorbar ranging from ~10-57 kPa. (b) Transect plots through the center of the volume along the cardinal directions show the profile of elasticity contrast (dotted lines) overlaid by the true profile of the simulation (solid lines).

Table 6. Evaluation of reconstruction fidelity for lesion detection

	CNR	QRS (%)	Max CR (×:1)	Optimal CR (×:1)
CT	3.55	99.4	2.66	3.01
MR	3.93	99.7	2.02	2.26

Max CR = maximum elasticity contrast between lesion and normal tissue in naïve reconstruction

Optimal CR = optimal elasticity contrast after accounting for overlap in elasticity region partitioning

Evaluating boundary condition influence: Robustness to randomized noise

Table 7 demonstrates that as the magnitude of the applied randomized noise vectors was increased, changes in the reconstructed elasticity contrast reflected a decreased ability to achieve a successful result (recall that the correct ratio is 6:1). For the CT simulation, on average, errors of 0.5 voxel units or greater showed a dramatically reduced ability to accurately characterize the stiffness of the lesion. Similarly, though at a much smaller scale, the MR simulation began to have noticeable difficulty in achieving a reasonable reconstruction at noise levels of 0.05 voxel units. These values were taken as suitably conservative measures for evaluating the efficacy of boundary conditions generated by the semi-automated methods.

Table 7. Effect of applied random boundary condition noise on objective function space and reconstructed elasticity contrast ratio. The respective ranges where a cutoff in reconstruction tolerance was observed are listed for each simulation set.

CT		***MR***	
Randomized vector magnitude (voxel units)	Mean optimal elasticity contrast value (×:1)	Randomized vector magnitude (voxel units)	Mean optimal elasticity contrast value (×:1)
0.1	5.62 ± 0.421	0.01	6.33 ± 0.096
0.2	5.70 ± 0.588	0.02	6.75 ± 0.058
0.3	5.97 ± 0.846	0.03	6.93 ± 0.634
0.5	2.36 ± 0.393	0.05	7.60 ± 0.821
1.0	2.47 ± 0.266	0.1	9.35 ± 1.27
2.0	2.17 ± 0.422	0.2	11.3 ± 0.866

Evaluating boundary condition influence: Reconstruction effects of generated boundary conditions

The accuracy of each automated boundary condition technique described in Section "Feasibility of automated boundary condition generating methods" was assessed by the target registration error with the gold standard boundary condition set and its ability to characterize the elastic contrast in the two-material reconstruction test case. Figure 31 depicts the deformation fields as applied to the CT data. Qualitatively, the displacements found by the diffusion method are quite different from the true set, while the results from the solution of Laplace's equation and the thin-plate spline interpolation appear to be more satisfactory. The mean TRE of the three methods confirms that the spline-based method has the best performance (0.26 mm), the Laplace method next (0.52 mm), and the diffusion method being the worst (1.5 mm). Inspection of Figures 32 and 33 further demonstrates that the imposition of an

inexact boundary condition set on the model has a distinct effect on the optimization by shifting the objective function minimum value to a different optimal elastic contrast ratio. Additionally, the convexity of the objective function is lost in the cases with a higher TRE. The differences in the generated boundary condition sets for the MR simulation are not easily visualized but follow a similar performance trend (TRE of spline 0.023 mm, Laplace method 0.48 mm, diffusion 0.61 mm). For both simulations, there exists a direct relationship between a low TRE and increased reconstruction fidelity in characterization of the elasticity contrast of the lesion.

Table 8. Reconstruction performance as affected by semi-automated boundary condition generation methods. The mean error of surface registration is related to the accuracy of characterizing the lesion stiffness.

	CT		***MR***	
Method	TRE (mm)	Elasticity contrast (×:1)	TRE(mm)	Elasticity contrast (×:1)
Diffusion	1.5	17.5	0.61	348.
Laplace	0.52	5.02	0.48	673.
Thin-plate spline	0.26	5.66	0.023	6.26

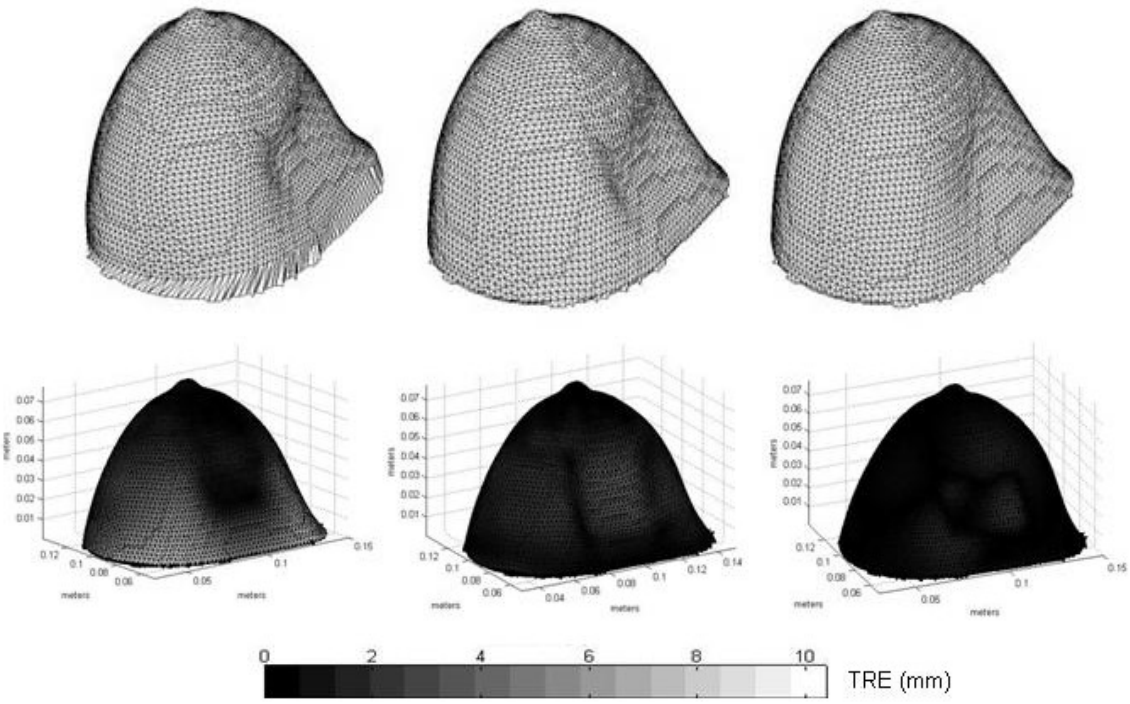

Figure 31. Three candidate automated methods for MIE boundary condition generation applied to simulation CT data. Top row, from left to right: surface deformations calculated from diffusion energy matching, Laplace solution energy, and thin-plate spline interpolation. Bottom row: target registration error (TRE) distribution for each method when compared against the gold standard of known correspondence. The diffusion-based mesh is both qualitatively and quantitatively the worst performer. The Laplace solution appears to capture the shape of the bladder indentation more precisely, but the thin-plate spline has the best overall accuracy in determining point correspondence.

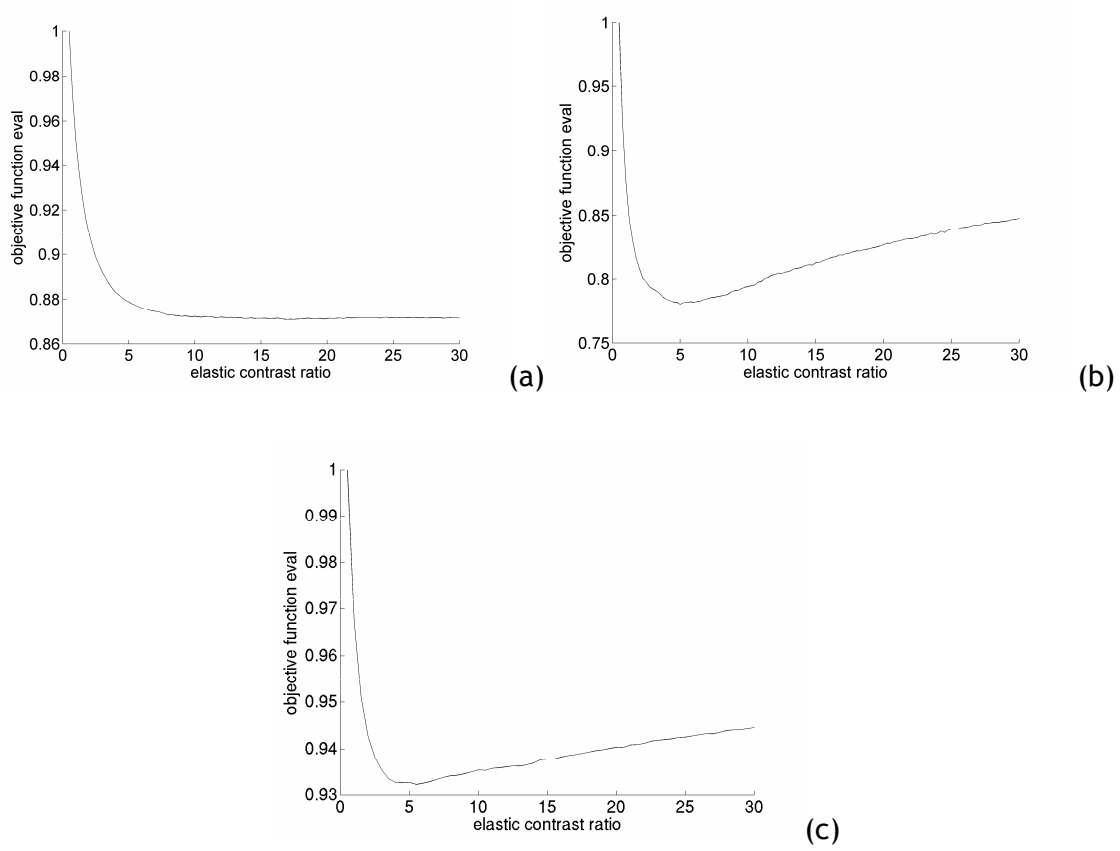

Figure 32. Mappings of objective function value vs. elasticity contrast ratio (tumor:breast) affected by the boundary condition sets generated from the different automated methods of surface point correspondence as applied to the CT data set. The minimum value of each curve corresponds to the altered optimal elasticity contrast when constrained by the inaccuracies of the methods: (a) diffusion, (b) Laplace, and (c) thin-plate spline interpolations. The ordinate is normalized to the initial value of each case. The global minimum of (a) is out of range of the plot.

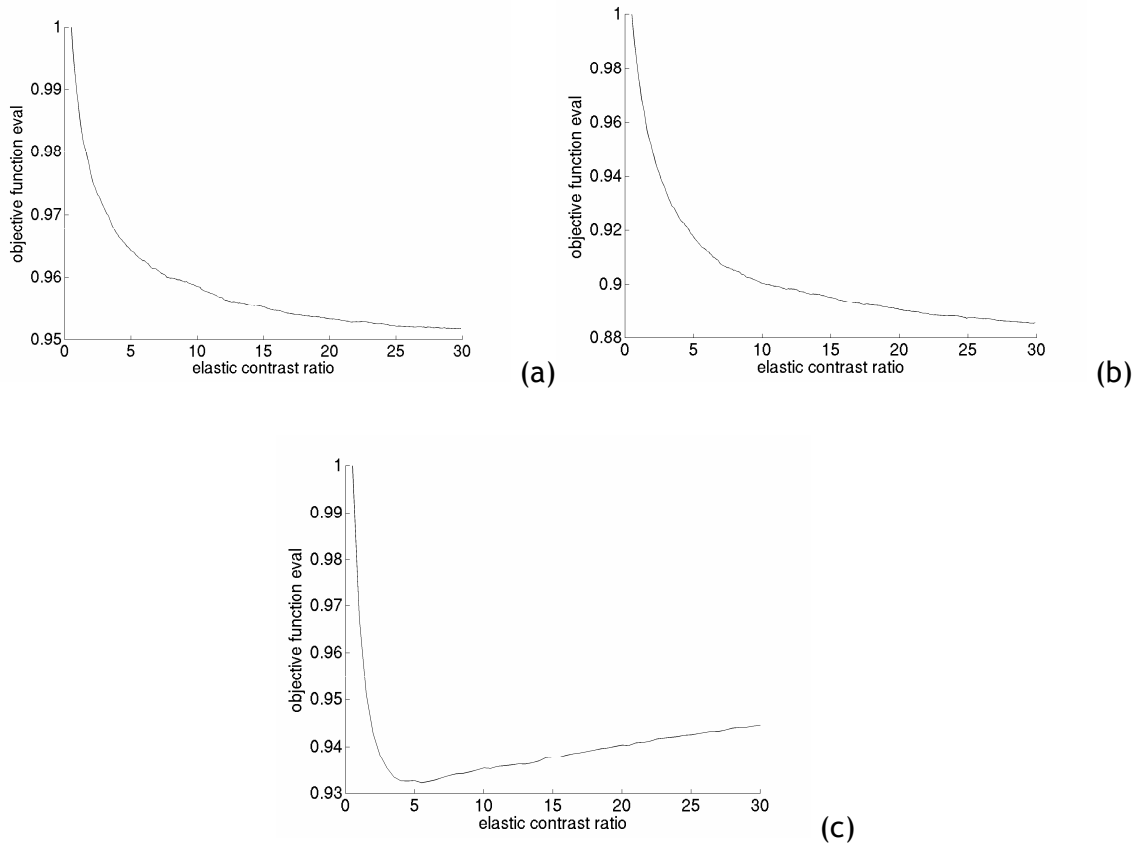

Figure 33. Mappings of objective function value vs. elasticity contrast ratio (tumor:breast) affected by the boundary condition sets generated from the different automated methods of surface point correspondence as applied to the MR data set. The minimum value of each curve corresponds to the altered optimal elasticity contrast when constrained by the inaccuracies of the methods: (a) diffusion, (b) Laplace, and (c) thin-plate spline interpolations. Again, the ordinate is normalized to the initial value and should not be interpreted as an equivalent scale for each case. The global minima of (a) and (b) are out of range of the plot.

Discussion

As other researchers have noted, the incorporation of *a priori* information can greatly enhance the performance of their elastography methods (Doyley *et al.*, 2006; Doyley *et al.*, 2005). We recognize that the judicious use of information regarding lesion morphology as obtained from conjunctive imaging studies and post-processing would potentially aid MIE as well, especially in reducing the number of search parameters and improving initialization of the algorithm. The reconstructions using *a priori* spatial knowledge of the inclusion were initially intended to simply illustrate that the objective function space formed by using an image similarity metric was smooth and readily traversed by the algorithm in a manner expected for a Gauss-Newton optimization. However, they also provide a stark contrast to the naïve lesion detection test cases, which were performed to evaluate the inverse problem framework and demonstrate its ability to analyze the full 3D domain of the breast. The results of the generalized reconstructions are very encouraging in having successfully identified and localized the inclusions. Although the discretizations of the meshes did not achieve particularly accurate material characterizations, the optimal elasticity contrast as dictated by the available objective function was matched in each case to within 12%. The observation that mis-estimation of the lesion extent altered the underlying test scenarios suggests that investigating methods of dynamically adjusting region assignment could facilitate shape resolution and concomitantly better elasticity contrast ratio values.

In translating MIE and its associated technologies to a clinical setting, a number of factors must be considered for realistic deployment. From an implementation and performance perspective, the large size of the inverse problem necessitated the careful selection of matrix solvers and programming of parallel computing routines that proved effective with the availability of a number of processors. Initial predictions based on sequential execution times needed to handle the high degrees of freedom in the naïve reconstructions were thus reduced from two weeks to several hours. Additional challenges were eventually overcome in the pre-processing load of image segmentation, model generation, and partitioning schemes.

The results presented in this paper also further our understanding of how the loss of input data quality, whether through design limitations or unpredictable factors, could have a significant impact on the end reconstruction. In particular, the proper application of accurate boundary conditions plays a critical role in MIE reconstruction success. This is due to the link between surface shape matching and subsequent interpolation of internal displacements in affecting sub-surface image intensities and similarity measurements. The results of the boundary condition noise experiment are interesting because they indicate that some level of improper localization of surface point correspondence is reasonably tolerated by the algorithm. However, perturbations greater than an empirically observed threshold can impair its ability to determine the underlying elasticity distribution. This is a similar result to prior work done in two-dimensional systems for which

successful reconstructions correlated to boundary condition selection errors limited to half a pixel length (Ou *et al.*, 2006b). It also confirms that randomizing the vectors for the additive noise experiments poses a considerable challenge to the algorithm because of the introduction of grossly non-physical deformations in the finite element mesh that decrease the stability of the numerical model. We observed that the threshold for the MR simulation was an order of magnitude less than that of the CT set and initially seemed to require an unfeasible level of accuracy, as well as quite a few more fiducials. These key differences are likely related to image resolution (the MR volume had fewer slices and a larger voxel spacing) and to the inherent differences in soft-tissue contrast between the two modalities. Both issues present interesting challenges that will be explored in future work.

The implausibility of performing manual selection on all boundary nodes of a three-dimensional mesh (there were 6,319 points for the CT and 5,416 for the MR set) underscores the importance of finding an automated method for determining point correspondences. In general, energy matching from the solutions of the diffusion and Laplace equations yielded boundary condition sets that were inadequate for reconstructing a proper elasticity contrast. This can be partly explained because the TRE of those surface registration techniques (as compared to the gold standard) was typically greater than the permissible value established by the robustness tests. The primary manifestation of these poor matches was that the model often had difficulty in obtaining a stable solution. Indeed, only the boundary conditions generated by

thin-plate spline method, which had the least error, were able to consistently achieve successful reconstructions while also satisfying the putative cutoffs. Overall, the reconstruction behavior for this method was consistent to within 6% of the true value. This appears to recommend the use of thin-plate spline interpolation as a strong candidate for generating boundary conditions for MIE.

Conclusion

In this work, we have presented the first fully three-dimensional realization of the MIE algorithm and preliminary evaluation of accompanying strategies for automated boundary condition deployment. The use of parallel processing enabled a practical implementation of a computational problem that might otherwise prove intractable. Simulation experiments demonstrate the viability of the method to utilize images obtained from different sources in reconstructing an embedded lesion with or without the benefit of *a priori* information concerning its location and size. We have also characterized the robustness of the elastography method to inaccuracies in boundary condition inputs derived from either random noise or by surface point correspondence methods. These results should prove valuable in the customization and streamlining of data acquisition and pre-processing for forthcoming clinical tests.

Acknowledgments

The authors would like to acknowledge John Boone, PhD (University of California-Davis Medical Center, Dept. of Radiology) for the donation of the CT data set, and Prashanth Dumpuri, PhD (Vanderbilt University, Dept. of Biomedical Engineering) for software development support. Additional thanks goes to the Vanderbilt Advanced Computing Center for Research and Education for use of cluster resources. This work was funded by a Breast Cancer Research Program Predoctoral Traineeship Award (BC043661) of the Congressionally Directed Medical Research Program along with a Whitaker Foundation Young Investigator Award. T.E. Yankeelov is supported by NIBIB 1K25EB005936-01.

References

ACS 2007 Cancer Facts and Figures. (Atlanta: American Cancer Society)

Ahmdahl G 1967 Validity of the single processor approach to achieving large-scale computing capabilities. In: *AFIPS Conference Proceedings,* pp 483-5

Balay S, Buschelman K, Eijkhout V, Gropp W, Kaushik D, Knepley M, McInnes L, Smith B and Zhang H 2004 PETSc Users Manual. (Argonne, IL: Argonne National Laboratory)

Balay S, Gropp W D, McInnes L C and Smith B F 1997 *Modern Software Tools in Scientific Computing*: Birkhauser Press) pp 163-202

Bilgen M 1999 Target detectability in acoustic elastography *IEEE Transactions on Ultrasonics Ferroelectrics and Frequency Control* **46** 1128-33

Boone J M, Kwan A L, Yang K, Burkett G W, Lindfors K K and Nelson T R 2006 Computed tomography for imaging the breast *Journal of mammary gland biology and neoplasia* **11** 103-11

Boone J M and Lindfors K K 2006 Breast CT: potential for breast cancer screening and diagnosis *Future oncology (London, England)* **2** 351-6

Boone J M, Nelson T R, Lindfors K K and Seibert J A 2001 Dedicated breast CT: radiation dose and image quality evaluation *Radiology* **221** 657-67

Boresi A and Chong K P 1999 *Elasticity in Engineering Mechanics* (New York: Wiley-Interscience)

Curiel L, Souchon R, Rouviere O, Gelet A and Chapelon J Y 2005 Elastography for the follow-up of high-intensity focused ultrasound prostate cancer treatment: initial comparison with MRI *Ultrasound in medicine & biology* **31** 1461-8

Doyley M M, Srinivasan S, Dimidenko E, Soni N and Ophir J 2006 Enhancing the performance of model-based elastography by incorporating additional a priori information in the modulus image reconstruction process *Physics in medicine and biology* **51** 95-112

Doyley M M, Srinivasan S, Pendergrass S A, Wu Z and Ophir J 2005 Comparative evaluation of strain-based and model-based modulus elastography *Ultrasound in medicine & biology* **31** 787-802

Doyley M M, Weaver J B, Van Houten E E, Kennedy F E and Paulsen K D 2003 Thresholds for detecting and characterizing focal lesions using steady-state MR elastography *Medical physics* **30** 495-504

Egorov V, Ayrapetyan S and Sarvazyan A P 2006 Prostate mechanical imaging: 3-D image composition and feature calculations *IEEE transactions on medical imaging* **25** 1329-40

Fitzpatrick J M, Hill D L G and Maurer C R 2000 *Handbook of Medical Imaging,* (Bellingham, WA: SPIE Press) pp 447-513

Fowlkes J B, Emelianov S Y, Pipe J G, Skovoroda A R, Carson P L, Adler R S and Sarvazyan A P 1995 Magnetic-resonance imaging techniques for detection of elasticity variation *Medical physics* **22** 1771-8

Garra B S, Cespedes E I, Ophir J, Spratt S R, Zuurbier R A, Magnant C M and Pennanen M F 1997 Elastography of breast lesions: initial clinical results *Radiology* **202** 79-86

Gokhale N, Richards M, Oberai A, Barbone P E and Doyley M M 2004 Simultaneous elastic image registration and elastic modulus reconstruction. In: *IEEE International Symposium on Biomedical Imaging,* (Arlington, VA: IEEE Press) pp 543-6

Goshtasby A 1988 Registration of images with geometric distortions *IEEE Trans Geosci and Remote Sensing* **26** 60-4

Joachimowicz N, Pichot C and Hugonin J P 1991 Inverse scattering: an iterative numerical method for electromagnetic imaging *IEEE Trans Biomed Engineering* **39** 1742-52

Krouskop T A, Wheeler T M, Kallel F, Garra B S and Hall T 1998 Elastic moduli of breast and prostate tissues under compression *Ultrason Imaging* **20** 260-74

Lapidus L and Pinder G F 1982 *Numerical Solution of Partial Differential Equations in Science and Engineering* (New York: John Wiley & Sons)

Manduca A, Oliphant T E, Dresner M A, Mahowald J L, Kruse S A, Amromin E, Felmlee J P, Greenleaf J F and Ehman R L 2001 Magnetic resonance elastography: non-invasive mapping of tissue elasticity *Med Image Anal* **5** 237-54

McKnight A L, Kugel J L, Rossman P J, Manduca A, Hartmann L C and Ehman R L 2002 MR elastography of breast cancer: preliminary results *AJR Am J Roentgenol* **178** 1411-7

Melodelima D, Bamber J C, Duck F A, Shipley J A and Xu L 2006 Elastography for breast cancer diagnosis using radiation force: system development and performance evaluation *Ultrasound in medicine & biology* **32** 387-96

Miga M I 2002 A new approach to elastographic imaging: modality independent elastography. In: *Medical Imaging 2002: Image Processing,* (San Diego, CA: SPIE Press) pp 604-11

Miga M I 2003 A new approach to elastography using mutual information and finite elements *Physics in medicine and biology* **48** 467-80

Miga M I, Rothney M P and Ou J J 2005 Modality independent elastography (MIE): potential applications in dermoscopy *Medical physics* **32** 1308-20

Muthupillai R, Lomas D J, Rossman P J, Greenleaf J F, Manduca A and Ehman R L 1995 Magnetic resonance elastography by direct visualization of propagating acoustic strain waves *Science* **269** 1854-7

Ophir J, Cespedes I, Ponnekanti H, Yazdi Y and Li X 1991 Elastography: a quantitative method for imaging the elasticity of biological tissues *Ultrason Imaging* **13** 111-34

Ophir J, Garra B, Kallel F, Konofagou E, Krouskop T, Righetti R and Varghese T 2000 Elastographic imaging *Ultrasound in medicine & biology* **26 Suppl 1** S23-9

Otsu N 1979 Threshold Selection Method from Gray-Level Histograms *IEEE Transactions on Systems Man and Cybernetics* **9** 62-6

Ou J J, Barnes S L and Miga M I 2006a Application of multi-resolution modality independent elastography for detection of multiple anomalous objects. In: *Medical Imaging 2006: Physiology, Function and Structure from Medical Images,* (San Diego, CA: SPIE Press) pp 614310-1 to -9

Ou J J, Barnes S L and Miga M I 2006b Preliminary testing of sensitivity to input data quality in an elastographic reconstruction method. In: *IEEE International Symposium on Biomedical Imaging,* (Arlington, VA: IEEE Press) pp 948-51

Papademetris X, Sinusas A J, Dione D P, Constable R T and Duncan J S 2002 Estimation of 3-D left ventricular deformation from medical images using biomechanical models *IEEE transactions on medical imaging* **21** 786-800

Parker K J, Taylor L S, Gracewski S and Rubens D J 2005 A unified view of imaging the elastic properties of tissue *The Journal of the Acoustical Society of America* **117** 2705-12

Samani A, Zubovits J and Plewes D 2007 Elastic moduli of normal and pathological human breast tissues: an inversion-technique-based investigation of 169 samples *Physics in medicine and biology* **52** 1565-76

Sarvazyan A P, Skovoroda A R, Emelianov S Y, Fowlkes J B, Pipe J G, Adler R S, Buxton R B and Carson P L 1995 *Acoustical Imaging,* ed J P Jones (New York: Plenum Press) pp 223–40

Sinkus R, Lorenzen J, Schrader D, Lorenzen M, Dargatz M and Holz D 2000 High-resolution tensor MR elastography for breast tumour detection *Physics in medicine and biology* **45** 1649-64

Tsap L V, Goldgof D B, Sarkar S and Powers P S 1998 A vision-based technique for objective assessment of burn scars *IEEE transactions on medical imaging* **17** 620-33

Washington C W and Miga M I 2004 Modality independent elastography (MIE): a new approach to elasticity imaging *IEEE transactions on medical imaging* **23** 1117-28

Yankeelov T E, Lepage M, Chakravarthy A, Broome E E, Niermann K J, Kelley M C, Meszoely I, Mayer I A, Herman C R, McManus K, Price R R and Gore J C 2007 Integration of quantitative DCE-MRI and ADC mapping to monitor treatment response in human breast cancer: initial results *Magnetic resonance imaging* **25** 1-13

Zhang Y, Goldgof D B and Sarkar S 2004 Significance of elastic properties in physics-based nonrigid motion modeling: a numerical sensitivity analysis. In: *CVPRW* p21

CHAPTER VI

MANUSCRIPT 5: DEVELOPMENT AND PRELIMINARY TESTING OF A BREAST PHANTOM SYSTEM FOR 3D MODALITY-INDEPENDENT ELASTOGRAPHY

Jao J. Ou[1], Rowena E. Ong[1], Aubrey A. McKelvey[1], and Michael I. Miga[1,2,3]

[1]Vanderbilt University, Department of Biomedical Engineering, Nashville, TN 37235, USA

[2]Vanderbilt University Medical Center, Department of Radiology and Radiological Sciences, Nashville, TN 37232, USA

[3]Vanderbilt University Institute of Imaging Science, Nashville, TN 37232, USA

This manuscript is in preparation for submission to *Medical Image Analysis*

Abstract

This paper reports on the creation of a tissue-mimicking breast phantom system and its use in the preliminary testing of a three-dimensional inverse problem technique for extracting soft tissue elasticity information. The modality independent elastography (MIE) algorithm determines the spatially distributed material properties of a domain via a non-rigid model-based image registration between images acquired under different states of loading. Previous simulation experiments with clinical image sets of human breast were able to identify and characterize a radiographically occult lesion. Therefore, a real-world study was performed using two polyvinyl alcohol cryogels designed with an embedded stiff inclusion and appropriate imaging properties for X-ray computed tomography. Data acquisition was accomplished with a customized chamber that delivered a

static compression to the phantoms. MIE reconstructions were evaluated by independent mechanical instrumentation testing as well as retrospective localization accuracy. The phantom experiencing a near-field deformation with respect to the subsurface position of the inclusion had a more successful performance (5.5% error in elasticity contrast, 80% positive localization) in comparison with the one under far-field deformation (24%; 58%).

Introduction

Early detection of breast lesions with malignant potential plays an important role in patient prognosis and survival. While X-ray mammography is the current clinical standard for screening and detection of breast cancer, physicians also continue to use palpation during the physical exam as a means of identifying lesions that are distinct from the tactile properties of unremarkable breast tissue. Although palpation is a purely qualitative evaluation of a lesion's firmness and motility, the concept of utilizing movement in tissue to deduce its constituent stiffness was effectively refined with advances in ultrasound (US) [1] and magnetic resonance (MR) [2] imaging which led to the creation of the field of elastography. Recent and ongoing research [3-9] has indicated that this diverse family of methods may have a viable clinical role in the process of identifying breast lesions.

Most elastography techniques are grounded in specific imaging sequences and protocols for the particular modality of acquisition, usually for the purpose of encoding precise measurements of displacements in the domain of interest. In contrast, a quantitative technique known as 'modality-independent elastography'

(MIE) has been introduced [10-12] with the intent of analyzing typical diagnostic image sets as a generalized inverse problem using only image similarity. The forward problem is a non-rigid, intramodal image registration performed *via* a biomechanical computer model, and the inferred parameters of the system constitute the spatial distribution of elasticity. The end result is a reconstructed mapping of the material properties that can be inspected for the assessment of lesions. To accomplish this goal, an image of a tissue of interest (*source*) is deformed by the model and compared against an image of the same tissue in a mechanically loaded state (*target*). Iterative updates of elasticity parameters to the model are applied until a suitable match in image similarity is achieved in a least squares manner to satisfy a non-linear optimization scheme.

A recent development for MIE has been the implementation of the algorithm to handle fully three-dimensional data that would be expected from the majority of modern medical imaging platforms, especially MR and X-ray computed tomography (CT). In simulation studies presented in [13], the method was able to identify a radiographically occult lesion within images of human breast obtained from both MR and CT scanners. The relative success of these experiments provided the impetus for us to initiate this study of real-world performance of the algorithm. Because a clinical trial is at this stage still potentially premature, the next logical step is to create a phantom system. The objectives were to 1) create a phantom with suitable material and imaging characteristics 2) build a test platform that could reliably deliver necessary compression to the phantom during imaging acquisition 3) perform independent mechanical testing to provide a gold

standard for evaluating reconstructed elasticity parameters and 4) evaluate MIE performance in characterizing the material composition of the phantom and detecting an embedded inclusion. This paper reports on recent experimental work with a simple phantom of the breast constructed from polyvinyl alcohol cryogel (PVA-C) and containing a single spherical tumor.

Methods

Material preparation

A variety of tissue-mimicking materials have been utilized by researchers [14, 15] attempting to replicate characteristics of the breast. However, a number of these substances involve the use of potentially hazardous crosslinking and stabilizing reagents. In contrast, polyvinyl alcohol is generally non-toxic and biocompatible. It also has the known property of becoming progressively stiffer with the application of repeated phases of freezing and thawing, making it well-suited for elastography-related research [8, 16-19].

The basic polymer mixture was prepared by creating a 7% w/v suspension of hydrolyzed polyvinyl alcohol powder (Flinn Scientific, Batavia, IL) in cold water and heating to 80^{o}C. A 10% by volume addition of glycerol (Fisher Scientific, Pittsburgh, PA) was then incorporated until clear and fluid. The container was covered tightly to minimize dehydration and allowed to cool to room temperature while gently agitated on a magnetic stir plate. To create the cryogel, full polymerization was achieved by the application of sequential freeze-thaw cycles

(FTCs), where the material was brought to -37°C over the course of 12 hours and then naturally returned to approximately 20°C over another 12 hours.

Phantom construction

The manufacturing of a phantom began by mixing 400 cc of the above formulation. To achieve separation in material elasticity, it was decided that the tumor would be created from PVA-C that underwent two FTCs in total, with the bulk of the rest of the phantom encasing it in a single freeze-thaw cycle. Initial experimentation had indicated that differing numbers of applied FTCs had no discernable impact on the resulting CT units, probably because the cryogel is primarily composed of water and therefore did not have a detectable change in density. Therefore, a relatively small amount of radiopaque contrast was introduced to dope the polymer mix for the tumor with a 6% v/v quantity of barium sulfate suspension (Lafayette Pharmaceuticals, Lafayette, IN). The tumor was initially manufactured in a silicone mold to produce a 25-mm diameter sphere using a single freeze-thaw cycle. It was then suspended by very thin plastic wires to be slightly off-centre inside a polystyrene mold used to simulate the shape of a pendant breast. The entire system was filled with about 250 cc of the basic liquid polymer. Approximately 5cc of the remaining mixture was enhanced with 3% v/v barium and gently injected into the system to distribute a few random streams for image texture in the bulk material. The whole phantom was then subjected to another full freeze-thaw cycle and the wires removed to produce the final semi-anthropomorphic phantom with an embedded stiff tumor. In order to provide

tracking of displacements, required as a pre-processing input to the algorithm described below, approximately 30 polytetrafluoroethylene spherical beads (McMaster-Carr, Atlanta, GA) measuring 1.6 mm in diameter were embedded just below the surface of the phantom.

Material testing protocol

To obtain gold-standard values of the elastic moduli for the two types of gel, independent mechanical tests were performed on samples of the materials. Using the remaining portion of polymer mixture from the batch used to make the phantom, a polymer mixture was poured into standard 24-well polystyrene cell culture plates (Corning Inc., Corning, NY) and then freeze-thawed for either one or two cycles to produce regular cylindrical blocks approximately 15 mm x 15 mm (diameter x height) in size. For this study, the PVA-C was subjected to compression testing to match the usage of the chamber on the phantom. An ElectroForce 3100 test instrument (Bose, Eden Prairie, MN) adapted for biological tissues was programmed to provide fixed displacements to the cryogels. Each sample was mounted on a platform over a load cell rated at 25 N and subjected to five cycles of a half-triangle charge with a speed of 0.15 mm/s followed by a hold of 300 s ('ramp-dwell'). This control protocol was calibrated for each sample to test a range of applied strains at 2, 5, 10, and 15%, in keeping with small deformation theory. The transducer in line with the direction of compression provided a temporal tracking of force measurement. The elastic modulus values

were thus obtained from the slope of the derived stress-strain curves in the region of nearly steady-state loading.

Device construction

Because a basic requirement for acquisition of data for MIE is a static loading of the subject, a chamber was designed to hold the breast phantom in place during imaging while applying a gentle compression to its surface. The primary structural component is a rectangular housing of clear acrylic with an adjustable wall that can slide to trap the phantom and then be locked in place with nylon set screws. The opposing face contains a neoprene air bladder adapted from the inflation bag of a sphygmomanometer (W.A. Baum, Copiague, NY) that is positioned such that its center is nearly tangent to the midpoint of the height of the phantom. With the use of extended tubing, this system is capable of safely delivering compression from a distance of up to 25 feet, thus allowing the chamber to remain undisturbed between pre- and post-deformation acquisitions. The choice of materials used in the construction of the unit was intended to be compatible with different imaging modalities. Figure 34 below shows the device components and an example of a phantom mounted within the apparatus.

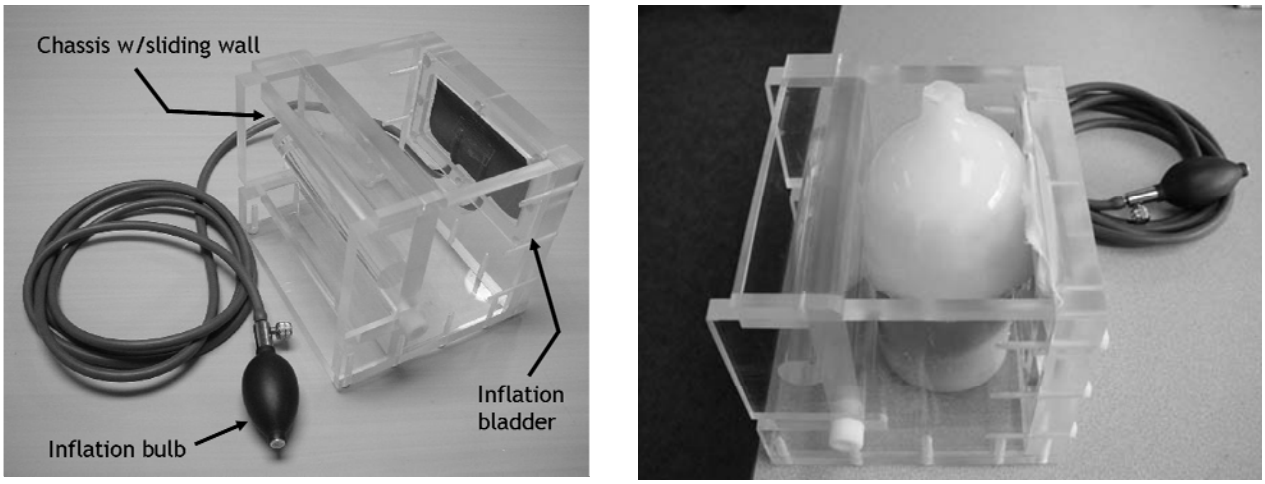

(a) (b)

Figure 34. MIE compression chamber setup for PVA-C breast phantom. The device used to deliver static loading to the phantoms is shown (a) in a perspective view with key components labeled and (b) angled top view with a phantom mounted within ready for imaging. The phantom rests on a cylindrical silicone platform in order to raise its height to be at the level of the inflation bladder.

Data acquisition

Two phantoms were constructed for this study and differed in the relative position of the tumor to the surface being deformed. The first (hereafter designated as Phantom1) contained a tumor embedded approximately 12 mm below the outer surface, while the second (Phantom2) was made with the tumor approximately 26 mm away. This variance in depth from the air bladder was designed in order to observe any behaviors related to near- or far-field compression.

In order to properly position a phantom within the compression chamber, a platform was constructed to elevate it to approximately the level of the air bladder. The platform was made from a cylinder of VytaFlex 10 urethane rubber

(Smooth-On, Easton, PA) and a thin cardboard spacer. This provided a stable base for the phantom to rest on and had advantageous imaging characteristics by being visibly distinct from the PVA-C while introducing minimal artifacts. After securing the sliding wall of the chamber to hold the phantom in place without being deformed, the unit placed in the CT scanner (Philips Medical, Bothell, WA). The pre-compression image was acquired using a high-resolution abdominal spiral sequence at 140 kVp/200 mAs. Phantom1 was reconstructed as a 512x512x143 volume with voxel spacing of 0.26 x 0.26 x 0.8 mm, while Phantom2 was obtained as a 512x512x139 volume with spacing 0.27 x 0.27 x 0.8 mm. The bladder was then inflated to approximately 200 mm Hg and the imaging protocol repeated to obtain the respective post-compression sets.

Reconstruction experiments

There are three primary components to the MIE reconstruction framework: a finite element representation of the model, an image comparison methodology, and a computational optimization routine. We utilize a finite element representation of a continuum model of mechanical equilibrium [20] and posit that the materials are isotropic Hookean solids and nearly incompressible in nature. While more complex models certainly exist, these assumptions are a reasonable starting point and have been made by other research groups working with PVA-C [19]. To create the models, the source image volumes were segmented from the compression chamber structures using semi-automatic techniques available in a commercial software package (ANALYZE 7.0, Mayo Clinic, Rochester, MN). The

resulting surface descriptions were then used to create tetrahedral meshes (Phantom1: 30,900 nodes and 166,509 elements; Phantom2: 33,930 nodes and 183,609 elements). Boundary conditions for the models were generated from the beads implanted just under the surface of the phantom. The positions of these physical markers were localized in both the source and target volumes by thresholding the images and finding the centroids of the voxels identified as part of the beads. Because the correspondence is known, these coordinates were used as the control points of a thin-plate spline [21] that provided an interpolation of displacements between the two surfaces. In this manner, all Type I (Dirichlet) conditions were specified for the model. The solution of the model using the Galerkin method of weighted residuals [22] was used to deform the source image. Image comparison was performed by the evaluation of local similarity, based on the correlation coefficient, between the model-deformed source image and the acquired target image over a number of groups of contiguous voxels termed *zones*. The change in these measures was used to guide a Levenberg-Marquardt optimization scheme (initialized as a homogeneous domain) to adjust the elasticity parameters until either a maximum number of iterations have been completed, or the relative change in similarity has converged to a threshold value of 1e-8. Further details of these processes and their implementation have been discussed previously in [10-12, 23] and extended to the current version described in [13].

The nature of the MIE algorithm is flexible depending on the amount of spatial *a priori* information used to constrain the problem. On one hand, full awareness of the composition of the domain reduces the computational burden of

the reconstruction process and focuses the task to a characterization of relative differences in material properties. At the other end of the spectrum, total lack of such knowledge requires the simultaneous optimization of a large number of parameters in order to perform a 'naïve' detection. We attempted both types of analyses with the data collected. For the *a priori* experiments, the elements comprising the tumor and bulk materials were identified according to a segmentation of the inclusion margin and assigned as their respective type within the model. The reconstruction was used to determine the elasticity contrast between the two forms of PVA-C based on the minimum objective function evaluation obtained by the optimization. In order to observe the effect of Poisson's ratio on the characterization, a range of values from ν = 0.3, 0.35, 0.4, 0.45, and 0.485 were tested. The naïve reconstructions require a separate pre-processing step using a basic K-means algorithm [24] to partition the domain by grouping the elements of the mesh into nearly equally-sized but spatially non-uniform *regions*. This sets the 'resolution' of the final reconstructed elasticity image and defines the degree of refinement for detection. In all experiments, 80 zones were used to discretize the images for similarity measurements, and 3200 regions created in breaking down the domains for the naïve reconstructions.

Results

MIE data acquisition

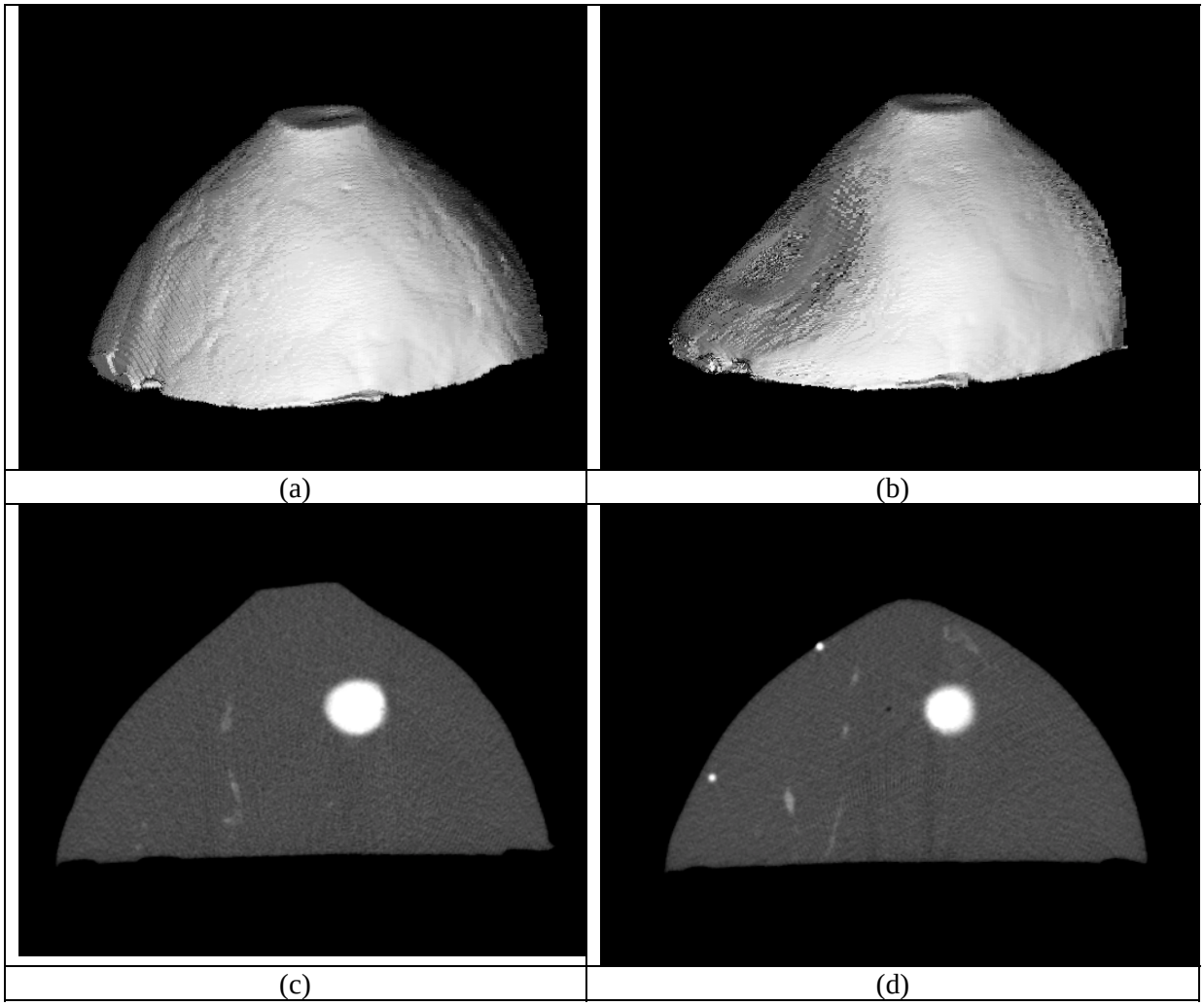

Figure 35. Surface renderings and selected cross-sectional views of PVA-C breast phantom acquired during MIE experiment. Panels (a) and (b) illustrate the deformation applied by the inflation system that distinguish the source and target image volumes, respectively. Panels (c) and (d) show the embedded inclusion enhanced by contrast agent as well as distributed amounts of barium sulfate that provide some image texture. Note in panel (d) the beads implanted just below the surface that are used for motion tracking. Phantom2 is shown as an example here.

Figure 35 shows an example of the imaging data acquired during an MIE experiment. The PVA-C breast phantom was visually distinct from the acrylic compression chamber and urethane rubber platform and therefore readily segmented. In addition, the figure shows that contrast within the phantom was reasonably achieved, with the bulk of the gel having CT numbers ranging from approximately 40-65, barium sulfate streams from 214-256, and the tumor at around 800-877 Hounsfield units.

Material testing

The elastic moduli of the two different forms of PVA-C as obtained from the ELF-3100 data are listed in Table 9. The values of the more pliable single freeze-thaw cycle material (FTC1) appear to be relatively stable over the range of applied strains, while the samples that experienced two cycles (FTC2) exhibit a stiffening behavior in resistance to higher compression. Comparison of the mean elasticity of each type shows that the materials differ by a factor of 4.03, which was set as the reference elasticity contrast ratio for evaluating subsequent reconstructions.

Table 9. Elastic modulus values (kPa) obtained from mechanical testing on samples of PVA-C for varying strain and freeze-thaw cycle.

Strain	FTC1	FTC2
2%	3.00 ± 0.758	7.92 ± 2.30
5%	4.73 ± 1.56	12.4 ± 0.998
10%	2.81 ± 0.265	15.1 ± 0.625
15%	3.01 ± 0.336	20.4 ± 0.295
Mean FTC1: 3.39 ± 1.14 Mean FTC2: 13.9 ± 4.77		

MIE Reconstructions

Recalling that the boundary conditions of the models are applied as all displacements, the relevant value for characterization of the phantoms is the elasticity contrast between the two materials (tumor:bulk). Table 10 summarizes the results of the reconstructions performed with full *a priori* spatial knowledge. The lowest objective function evaluation of the trials was used to determine optimally fitted elasticity parameters for each phantom. As the value of ν was increased, there was a concomitant decreasing trend in the objective function minimum. Figures 36 (a) and (b) illustrate the objective function spaces traversed by the algorithm where the best Poisson's ratio was found to be 0.485 for both phantoms, with a contrast ratio of 3.81 for Phantom1 and 3.06 for Phantom2.

Table 10. Reconstructed elasticity contrast ratios for MIE *a priori* experiments with varying Poisson's ratio.

	Phantom1		Phantom2	
ν	Min obj func eval	MIE contrast ratio	Min obj func eval	MIE contrast ratio
0.3	50.8146	21.9	45.3893	3.72
0.35	50.5398	8.97	45.2009	2.94
0.4	50.1303	7.59	44.9367	4.97
0.45	49.6868	9.27	44.4318	2.59
0.485	49.6762	3.81	43.8620	3.06

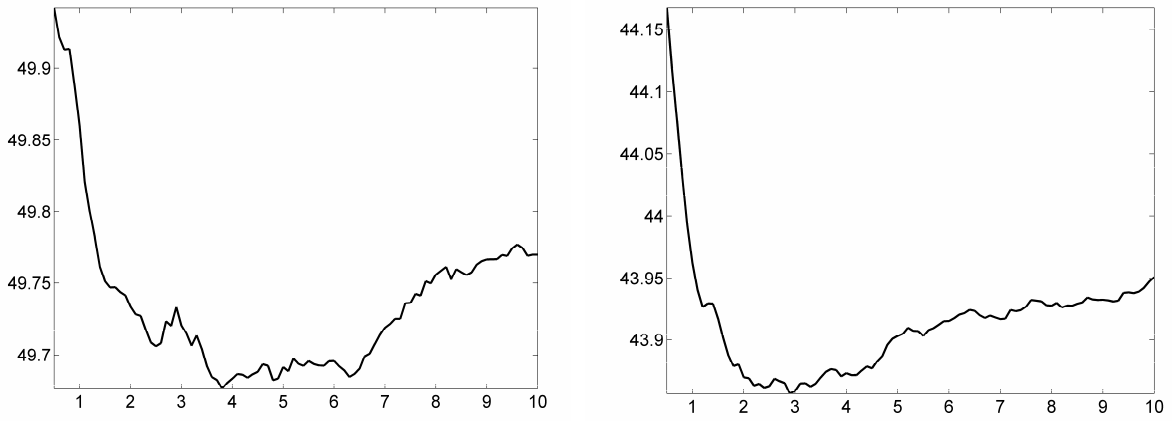

(a) (b)

Figure 36. Objective function spaces of *a priori* MIE reconstruction experiments performed on (a) Phantom1 and (b) Phantom2. In both cases, the trials using $\nu = 0.485$ produced the minimal values of the objective function (shown on the ordinate) and were used to determine the optimal elasticity contrast ratios reported in the text. The range of elasticity contrasts (abscissa) are shown over approximately an order of magnitude [0.5,10] for the ratio of tumor:bulk materials.

Table 11. MIE naïve reconstruction performance summary.

	CNR	CR	QRS (%)
Phantom1	2.97	2.03	80
Phantom2	2.61	1.91	58

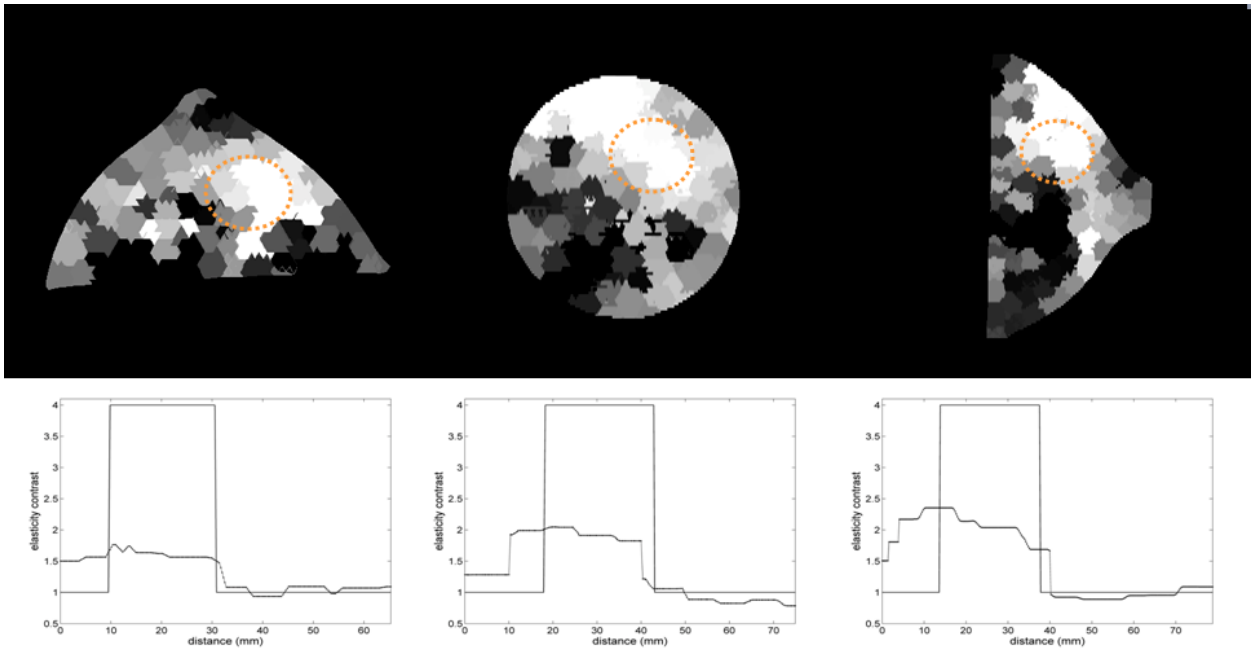

Figure 37. MIE naïve reconstruction of Phantom1. Higher (stiff) values of elasticity are shown at the white end of the grayscale mapping of the full range (~4-27 kPa). Top panel: orthogonal sections of the elasticity image volume taken through the center of the tumor. The margin of the tumor is indicated by the superimposed dotted line. Bottom panel: corresponding transect profiles through the tumor, demonstrating the profile of elasticity contrast overlaid by the true distribution (rectangular waveform).

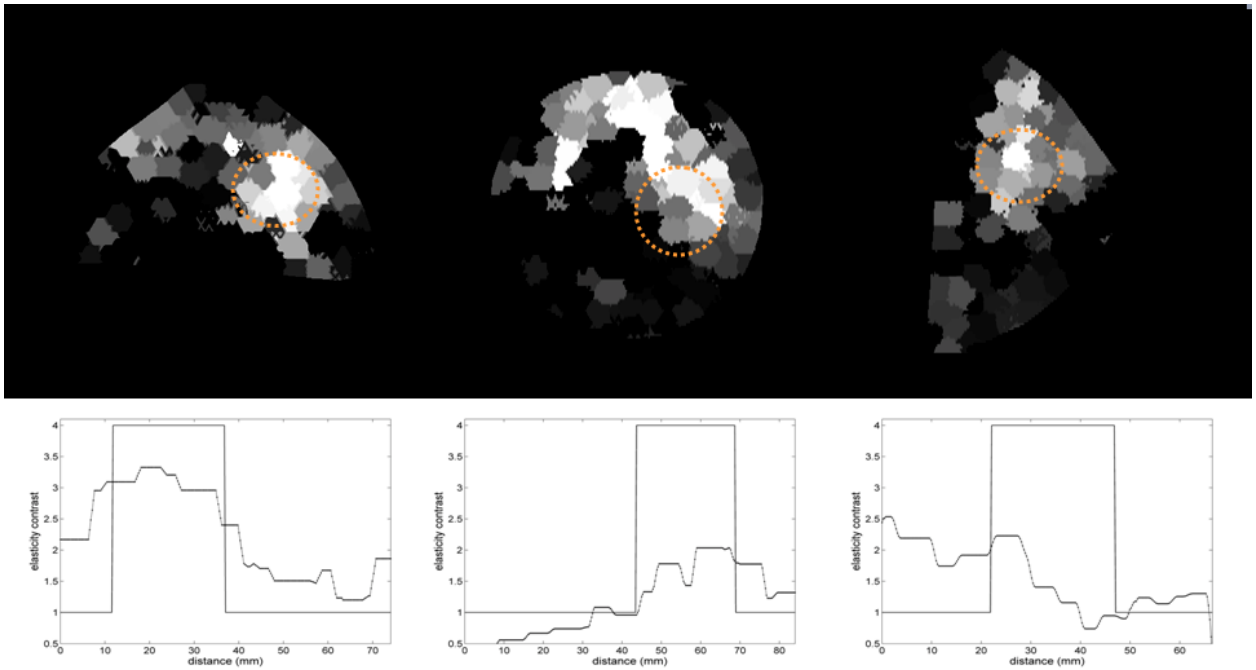

Figure 38. MIE naïve reconstruction of Phantom2. Higher (stiff) values of elasticity are shown at the white end of the grayscale mapping of the full range (~6-32 kPa). Top panel: orthogonal sections of the elasticity image volume taken through the center of the tumor. The margin of the tumor is indicated by the superimposed dotted line. Bottom panel: corresponding transect profiles through the tumor, demonstrating the profile of elasticity contrast overlaid by the true distribution (rectangular waveform).

The success of the naive reconstruction experiments was primarily evaluated on three criteria: the ability to detect the presence of two materials, the contrast between the materials based on classification of the material property distribution, and the retrospective accuracy of localizing the lesion as a distinct member of one of the material types. To obtain these measures, the final elasticity values obtained by the MIE algorithm were first treated as a Gaussian mixture of two classes and separated by a threshold established *via* the method described in [25]. The likelihood of discriminating a lesion within the resulting elasticity image was found using the contrast-to-noise ratio (CNR) as defined by [26, 27]:

$$CNR = \sqrt{\frac{2(\mu_L - \mu_B)^2}{\sigma_L^2 + \sigma_B^2}} \tag{1}$$

where μ and σ^2 are the sample mean and variance of a material property distribution and the subscripts *L* and *B* denote the lesion (FTC2 PVA-C) and bulk material types, respectively. Both Phantom1 and Phantom2 successfully identified the embedded stiff tumors as being distinct materials according to the cutoff of CNR≥2.2 as noted by [27]. Next, the mean modulus contrast value of a reconstruction was calculated by selecting equally sized areas representative of the two materials and taking the ratio of the average elasticity contained within. In both phantoms, this was approximately 2:1 as reported in Table 11. Finally, the

localization of the lesion was assessed by comparing the 'true positive' (TP) rate of correctly identifying a stiffer element within the known location of the inclusion (the dotted lines in Figures 37 and 38) against the 'false positive' (FP) rate of finding the stiff material elsewhere. These quantities are used to define the 'quality of reconstruction score' (QRS) as simply TP/(TP+FP). We continue to utilize a criteria of success as QRS≥80% as empirically determined in prior study of MIE [13, 28, 29]. Phantom1 appears to nearly satisfy this condition, while Phantom2 clearly falls below the desired level.

Discussion

From the mechanical testing data presented in Table 9, we observed a four-fold increase in mean elasticity between the first and second freeze-thaw cycles, which was used as the gold standard of elasticity contrast in evaluating subsequent reconstructions. It is interesting to note that [19] also identified a comparable 4.2-fold increase in elastic modulus for their PVA-C material from FTC1 to FTC2. In our characterization experiments using *a priori* spatial designation of the material types, it was determined (from tracking the minimum value of the objective functions) that the most appropriate Poisson's ratio was $\nu = 0.485$. This is typically the highest value we have empirically assigned in previous work for reasons of numerical stability, and the observed improvement in reconstruction performance over the lower values tested here is consistent with the expected behavior of a material with high water content. Despite some differences in

cryogel formulation, our finding is in line with the conclusions of [19] where the Poisson's ratio of their PVA-C was measured to be 0.499. Recent analyses by [30] indicate that values approaching 0.5 may incur problems with locking phenomena in the solution of the finite element model. Therefore, our use of $\nu = 0.485$ is a suitable approximation of near incompressibility for a tissue-mimicking material like PVA-C while maintaining favorable convergence properties in iterative matrix solvers.

The analysis presented in Table 10 also reveals some interesting behavior in the reconstructed elasticity contrast as linked to the variation in Poisson's ratio. This is most noticeable for Phantom1, where the contrast ratio shows a marked improvement with the decrease in objective function evaluation, producing a final value within 5.5% of that indicated by material testing. For Phantom2, the elasticity contrasts appear to fluctuate within a much smaller range of values. Although one trial for Phantom2 exhibited a similarly close match in contrast ratio, this occurred at the extreme lower limit of $\nu = 0.3$ (a physically unlikely value) and had the highest objective function evaluation in the experiment.

For Phantom2, the optimal contrast ratio had a 24% relative difference when compared to the "gold standard." However, this difference may be accounted for by the far-field compression, since the applied stresses have been more thoroughly dissipated by the bulk material. The consequent lack of force distributed to the area of the inclusion could cause less displacement to be generated, leading to a less distinct deformation in local image texture.

The naïve reconstructions were able to differentiate two distinct materials in the phantom by their CNR that differed in average elasticity by a factor of 2. From visual inspection of Figures 37 and 38, the stiffer material can be seen to mostly fall within the inclusion boundaries. According to the standards of localization currently set for the QRS, Phantom1 lay within the cutoff; however, Phantom2 did not meet the criteria. One explanation for this is that the discretization provided by the K-means regions is the only guidance for the algorithm in searching for the tumor. Without bias in the spatial partitioning, the likelihood of multiple regions intersecting the tumor leads to mis-estimation of the borders of the inclusion. Because these regions are comprised of both stiff and bulk materials, the reconstruction is forced to make best-fit compromises in elasticity throughout the domain. It is therefore not expected that the elasticity contrast ratio should accurately match the gold standard or even the *a priori* experiments. By examining the layout of the 3200 regions used in each phantom, we observed that grouping all regions overlapping the tumor produces an entity that overestimates the size of the inclusion by several millimeters. As a result, the algorithm was essentially attempting to reconstruct a 33 mm inclusion in Phantom1, while the agglomeration in Phantom2 was slightly larger at 35 mm, corresponding to its comparatively poorer localization. These findings emphasize the fact that the naïve reconstructions in MIE represent the highest degree of difficulty in utilizing a large-scale inverse scheme for both 3D detection and characterization. It is interesting to note that other applications in similar classes of problems, such as diffuse optical tomography, also experience marked

reductions in error with the incorporation of spatial priors to constrain the inherently ill-posed system [31, 32].

This phantom study has provided several other interesting pieces of information and elucidated some areas for future work. In the course of experimentation, we actually created and tested two different formulations of polyvinyl alcohol using 7% and 10% w/v of monomer. For material testing of the 10% material, the four-fold increase in stiffness between freeze-thaw cycles as seen for the 7% PVA-C was nearly exactly preserved, and the higher concentration had modulus values approximately doubled by comparison. This expands the range of elasticity values available for the design of newer phantoms, since the literature indicates that there are certainly variations in properties among tumors as well as normal breast tissue [33]. The 7% solution was eventually selected for its ease of handling and because the resulting cryogel had a tactile quality comparable to the palpation of breast tissue. We note that the use of glycerol in our mixtures was a successful improvement upon previous recipes tested, as the addition of the cryoprotectant aided in stabilizing the freezing process, thereby producing a more homogeneous medium. Another challenge encountered in the creation of the phantoms was the introduction of suitable imaging contrast and texture with which the reconstruction algorithm could make viable comparisons. The majority of work with PVA-C has been done with US and MR. Here, the injection of barium streams was able to add intensity variation to the phantom for CT imaging that would be otherwise provided by the normal lobulated breast parenchyma. While the end products created performed reasonably well, further

study into the distribution and characteristics of image pattern is an interesting avenue to pursue in the production of even more realistic phantoms. Finally, we confirmed that the use of implanted fiducials and thin-plate spline interpolation for boundary condition assignment was a reasonably practical application as suggested by our previous simulation work, as no non-physical deformations were forced upon the solution of the finite element model. Ongoing refinements are expected to further improve the accuracy of these estimates.

Conclusion

This paper represents an important advancement in the development of the MIE method for use in assessment of breast lesions. We have demonstrated a proof-of-concept system by creating a tissue-mimicking phantom with an embedded inclusion that was imaged within a customized compression chamber. The algorithm was able to reasonably characterize the elasticity of the phantom with the use of spatial priors as compared with independent material testing. In detection experiments without *a priori* information, the reconstruction was able to discriminate stiff components at a lower elasticity contrast. The phantom subjected to near-field compression (relative to the tumor location) overall had a more successful performance, especially in localization of the lesion as compared to the far-field compression. The results of this study are promising and will continue to guide our latest efforts to understand MIE behavior and ultimately its utility in a clinical setting.

Acknowledgments

The authors would like to thank the members of the CT Technologist staff at the Vanderbilt University Hospital (Debbie Deskins, Ed Quirante, Dahl Irwin, Wayman Bean, and many others) for their assistance in providing imaging facility support. Thanks also to David Kwartowitz, PhD of the Dept. of Biomedical Engineering, Vanderbilt University, for additional assistance in image acquisition. Finally, we are grateful to John Fellenstein and Bob Patchin from the machine shop of the Vanderbilt University College of Arts and Sciences for aiding in the design and construction of the compression chamber. This work was funded by a Breast Cancer Research Program Predoctoral Traineeship Award (BC043661) of the Congressionally Directed Medical Research Program.

References

[1] J. Ophir, I. Cespedes, H. Ponnekanti, Y. Yazdi, and X. Li, "Elastography: a quantitative method for imaging the elasticity of biological tissues," *Ultrason Imaging,* vol. 13, pp. 111-34, Apr 1991.

[2] R. Muthupillai, D. J. Lomas, P. J. Rossman, J. F. Greenleaf, A. Manduca, and R. L. Ehman, "Magnetic resonance elastography by direct visualization of propagating acoustic strain waves," *Science,* vol. 269, pp. 1854-7, Sep 29 1995.

[3] A. Thomas, T. Fischer, H. Frey, R. Ohlinger, S. Grunwald, J. U. Blohmer, K. J. Winzer, S. Weber, G. Kristiansen, B. Ebert, and S. Kummel, "Real-time elastography--an advanced method of ultrasound: First results in 108 patients with breast lesions," *Ultrasound Obstet Gynecol,* vol. 28, pp. 335-40, Sep 2006.

[4] A. Itoh, E. Ueno, E. Tohno, H. Kamma, H. Takahashi, T. Shiina, M. Yamakawa, and T. Matsumura, "Breast disease: clinical application of US elastography for diagnosis," *Radiology,* vol. 239, pp. 341-50, May 2006.

[5] G. M. Giuseppetti, A. Martegani, B. Di Cioccio, and S. Baldassarre, "Elastosonography in the diagnosis of the nodular breast lesions: preliminary report," *Radiol Med (Torino),* vol. 110, pp. 69-76, Jul-Aug 2005.

[6] T. Xydeas, K. Siegmann, R. Sinkus, U. Krainick-Strobel, S. Miller, and C. D. Claussen, "Magnetic resonance elastography of the breast: correlation of signal intensity data with viscoelastic properties," *Invest Radiol,* vol. 40, pp. 412-20, Jul 2005.

[7] R. Sinkus, M. Tanter, S. Catheline, J. Lorenzen, C. Kuhl, E. Sondermann, and M. Fink, "Imaging anisotropic and viscous properties of breast tissue by magnetic resonance-elastography," *Magn Reson Med,* vol. 53, pp. 372-87, Feb 2005.

[8] R. Sinkus, M. Tanter, T. Xydeas, S. Catheline, J. Bercoff, and M. Fink, "Viscoelastic shear properties of in vivo breast lesions measured by MR elastography," *Magn Reson Imaging,* vol. 23, pp. 159-65, Feb 2005.

[9] H. Zhi, B. Ou, B. M. Luo, X. Feng, Y. L. Wen, and H. Y. Yang, "Comparison of ultrasound elastography, mammography, and sonography in the diagnosis of solid breast lesions," *J Ultrasound Med,* vol. 26, pp. 807-15, Jun 2007.

[10] M. I. Miga, "A new approach to elastographic imaging: modality independent elastography," in *Medical Imaging 2002: Image Processing*, San Diego, CA, 2002, pp. 604-611.

[11] M. I. Miga, "A new approach to elastography using mutual information and finite elements," *Physics in Medicine and Biology,* vol. 48, pp. 467-480, Feb 21 2003.

[12] C. W. Washington and M. I. Miga, "Modality independent elastography (MIE): a new approach to elasticity imaging," *IEEE Trans Med Imaging,* vol. 23, pp. 1117-28, Sep 2004.

[13] J. J. Ou, R. E. Ong, T. E. Yankeelov, and M. I. Miga, "Evaluation of 3D modality independent elastography for breast imaging: a simulation study," *Physics in Medicine and Biology,* in press.

[14] E. L. Madsen, M. A. Hobson, G. R. Frank, H. Shi, J. Jiang, T. J. Hall, T. Varghese, M. M. Doyley, and J. B. Weaver, "Anthropomorphic breast phantoms for testing elastography systems," *Ultrasound Med Biol,* vol. 32, pp. 857-74, Jun 2006.

[15] E. L. Madsen, M. A. Hobson, H. Shi, T. Varghese, and G. R. Frank, "Tissue-mimicking agar/gelatin materials for use in heterogeneous elastography phantoms," *Phys Med Biol,* vol. 50, pp. 5597-618, Dec 7 2005.

[16] K. J. Surry, H. J. Austin, A. Fenster, and T. M. Peters, "Poly(vinyl alcohol) cryogel phantoms for use in ultrasound and MR imaging," *Phys Med Biol,* vol. 49, pp. 5529-46, Dec 21 2004.

[17] K. C. Chu and B. K. Rutt, "Polyvinyl alcohol cryogel: an ideal phantom material for MR studies of arterial flow and elasticity," *Magn Reson Med,* vol. 37, pp. 314-9, Feb 1997.

[18] E. Brusseau, J. Fromageau, G. Finet, P. Delachartre, and D. Vray, "Axial strain imaging of intravascular data: results on polyvinyl alcohol cryogel phantoms and carotid artery," *Ultrasound Med Biol,* vol. 27, pp. 1631-42, Dec 2001.

[19] J. Fromageau, J. L. Gennisson, C. Schmitt, R. L. Maurice, R. Mongrain, and G. Cloutier, "Estimation of polyvinyl alcohol cryogel mechanical properties with four ultrasound elastography methods and comparison with gold standard testings," *IEEE Trans Ultrason Ferroelectr Freq Control,* vol. 54, pp. 498-509, Mar 2007.

[20] A. Boresi and K. P. Chong, *Elasticity in Engineering Mechanics*, 2nd ed. New York: Wiley-Interscience, 1999.

[21] A. Goshtasby, "Registration of images with geometric distortions," *IEEE Trans Geosci and Remote Sensing,* vol. 26, pp. 60-64, Jan 1988.

[22] L. Lapidus and G. F. Pinder, *Numerical Solution of Partial Differential Equations in Science and Engineering*. New York: John Wiley & Sons, 1982.

[23] M. I. Miga, M. P. Rothney, and J. J. Ou, "Modality independent elastography (MIE): potential applications in dermoscopy," *Med Phys,* vol. 32, pp. 1308-20, May 2005.

[24] J. B. MacQueen, "Some Methods for classification and Analysis of Multivariate Observations," *Proceedings of the 5th Berkeley Symposium on Mathematical Statistics and Probability,* vol. 1, pp. 281-297, 1967.

[25] N. Otsu, "Threshold Selection Method from Gray-Level Histograms," *IEEE Transactions on Systems Man and Cybernetics,* vol. 9, pp. 62-66, 1979.

[26] M. Bilgen, "Target detectability in acoustic elastography," *IEEE Transactions on Ultrasonics Ferroelectrics and Frequency Control,* vol. 46, pp. 1128-1133, Sep 1999.

[27] M. M. Doyley, J. B. Weaver, E. E. Van Houten, F. E. Kennedy, and K. D. Paulsen, "Thresholds for detecting and characterizing focal lesions using steady-state MR elastography," *Med Phys,* vol. 30, pp. 495-504, Apr 2003.

[28] J. J. Ou, S. L. Barnes, and M. I. Miga, "Application of multi-resolution modality independent elastography for detection of multiple anomalous objects," in *Medical Imaging 2006: Physiology, Function and Structure from Medical Images*, San Diego, CA, 2006, pp. 614310-1 to 614310-9.

[29] J. J. Ou, S. L. Barnes, and M. I. Miga, "Preliminary testing of sensitivity to input data quality in an elastographic reconstruction method," in *IEEE International Symposium on Biomedical Imaging*, Arlington, VA, 2006, pp. 948-951.

[30] J. Fehrenbach, "Influence of Poisson's ratio on elastographic direct and inverse problems," *Phys Med Biol,* vol. 52, pp. 707-16, Feb 7 2007.

[31] P. K. Yalavarthy, B. W. Pogue, H. Dehghani, and K. D. Paulsen, "Weight-matrix structured regularization provides optimal generalized least-squares estimate in diffuse optical tomography," *Med Phys,* vol. 34, pp. 2085-98, Jun 2007.

[32] M. Guven, B. Yazici, X. Intes, and B. Chance, "Diffuse optical tomography with a priori anatomical information," *Phys Med Biol,* vol. 50, pp. 2837-58, Jun 21 2005.

[33] T. Krouskop, R. Price, T. Wheeler, and P. Younes, "Modulus variations in breast tissues," in *Proc International Conference of the Ultrasonics Measurements and Imaging of Tissue Elasticity*, Niagara Falls, 2002.

CHAPTER VII

MANUSCRIPT 6: APPLICATION OF MODALITY-INDEPENDENT ELASTOGRAPHY FOR EX VIVO TISSUE CHARACTERIZATION: INITIAL RESULTS WITH A MURINE LIVER FIBROSIS MODEL

J. J. Ou[1], S. L. Barnes[1,3], and M. I. Miga[1,2,3]

[1]Vanderbilt University, Department of Biomedical Engineering, Nashville, TN 37235, USA

[2]Vanderbilt University Medical Center, Department of Radiology and Radiological Sciences, Nashville, TN 37232, USA

[3]Vanderbilt University Institute of Imaging Science, Nashville, TN 37232, USA

This manuscript is in preparation as a technical note for submission to *Medical Physics*

Abstract

We report on the use of an inverse elasticity problem technique of image analysis to perform material property characterization of an *ex vivo* model of murine hepatic fibrosis. The tissue was embedded within a polyacrylamide gel block and subjected to a compression while being scanned in a microCT unit. These results were compared to two previously published methods of elasticity measurement taken on the same experiment. The elastography reconstruction matched the stress analysis to within 3% and was able to identify the global minimum of its objective function space within six iterations.

Introduction

Modality-independent elastograpy (MIE) is a novel inverse problem technique of using an iterative non-rigid, model-constrained image registration to reconstruct the spatial distribution of elastic properties. We have previously performed experiments in simulation and on phantom systems that demonstrate its ability to distinguish objects of differing elastic properties. The pathologic deposition of collagen in fibrotic processes over time can lead to a progressive stiffening of an organ such as the liver, making it a logical choice for material elasticity experiments. In this technical note, we extend MIE to another clinically relevant purpose by performing an *ex vivo* tissue characterization of a fibrotic murine liver sample embedded in a polyacrylamide gel matrix.

Methods

Sample preparation

As per the protocol reported in [1], an adult C57 mouse was treated with weekly intraperitoneal injections of a 1:4 suspension of 1 mL/kg carbon tetrachloride in olive oil and sacrificed on approximately day 35 of the experiment cycle. The resulting fibrotic liver was excised and the two largest lobes submerged in a 5% polyacrylamide gel (BioRad Laboratories, Hercules, CA) doped with a 2% v/v addition of ioversol X-ray contrast enhancement agent (Opitray, Mallinckrodt, Hazelwood, MO). The other lobes were reserved for independent material characterization (described below). The total liver-gel preparation was allowed to polymerize and fill the volume of a standard 35-mm polystyrene cell

culture dish (BD Biosciences, San Jose, CA) to create a cylindrical sample approximately 10 mm in height.

Material tests

Compression testing was previously performed using an ELF 3100 (Bose, Eden Prairie, MN) calibrated for displacement control and equipped with a 250-g transducer that recorded the in-line force. The liver-gel sample was mounted between two platens and subjected to a series of six sequential cycles of a 0.05-mm step excitation followed by a 60-s hold ('ramp-dwell'). A control sample of equal size but fabricated only out of polyacrylamide was tested in the same manner, and its elastic modulus obtained from analysis of the linear regions of its resulting stress-strain curves. This value was used as a fixed reference input to a finite element model of the composite sample in order to fit the elastic modulus of the liver according to an average surface stress match to the collected force data.

Image acquisition

An acrylic cage measuring approximately 50 mm x 50 mm x 20 mm (Figure 39a) was used to hold the sample dish with the liver-gel in place. A piston 19 mm in diameter was initially placed to rest just on the surface of the gel and was manually driven by machined nylon set screws to deliver a 1.4-mm compression to the exposed surface. Pre- (*source*) and post-compression (*target*) images of this setup were obtained from microCT scans (MicroCAT II, Imtek Inc., Knoxville, TN)

and reconstructed as a 512x512x512 volumes with isotropic spacing of 142 μm. In order to reduce computer memory requirements, 104 corresponding slices from both images known to be air were cropped out and the volumes downsampled by a factor of two. Before proceeding to the reconstruction, the target image was rigidly registered to the source in order to remove any unintended motion incurred between scans.

MIE Reconstruction

A tetrahedral mesh (91,116 nodes and 503,028 elements) was generated for the model from a segmentation of the source image (ANALYZE 7.0, Mayo Clinic, Rochester, MN), with each element being assigned as either gel or liver. Boundary conditions for the model were assigned such that all surfaces of the sample in contact with the dish were treated as fixed positions (Type I), those in contact with the piston displaced according to the compression (Type I), and the free surface not impinged as pure Neumann (Type II). Two elasticity regions defined by the spatial priors of the internal liver-gel interface along with 568 similarity zones were prescribed according to the procedures described in [2]. The finite element model (illustrated in Figure 40) was used to deform the source image and compared to the acquired target using the correlation coefficient [3] as the local similarity metric. The reconstruction was initiated with a homogeneous elasticity distribution and updated until either the completion of a maximum number of iterations or a convergence in the objective function evaluation to a relative tolerance of 1e-8.

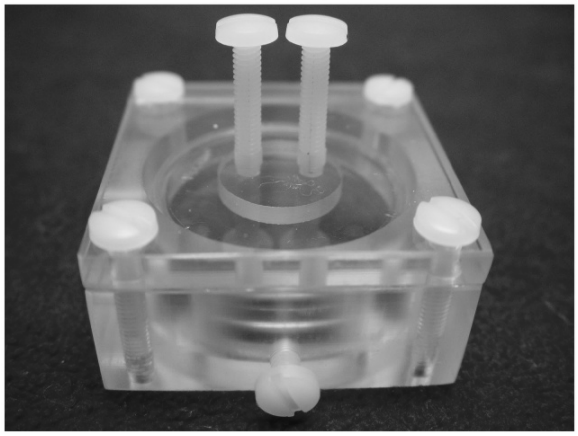
(a)

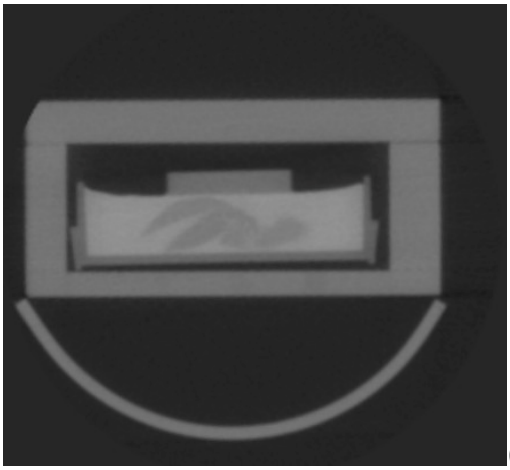
(b)

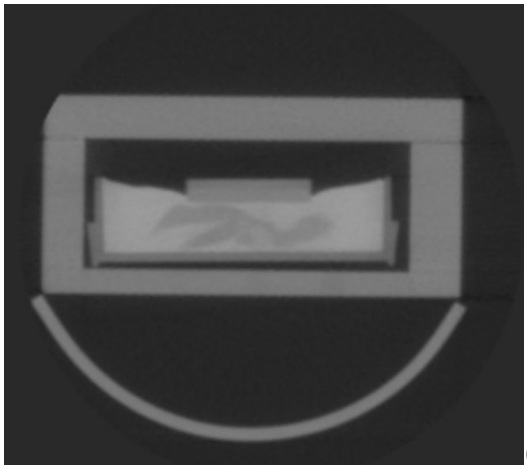
(c)

Figure 39. MIE data acquisition. (a) Photograph of compression chamber, (b) transverse CT slice of setup, and (c) liver-gel block under compression.

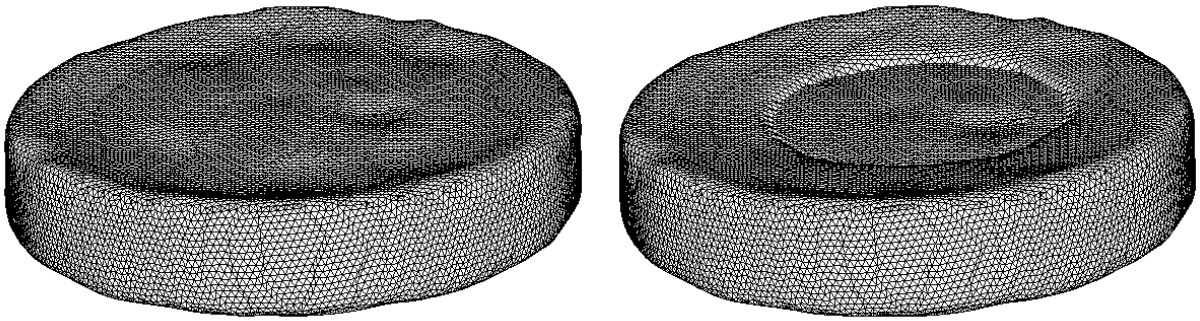

(a) (b)

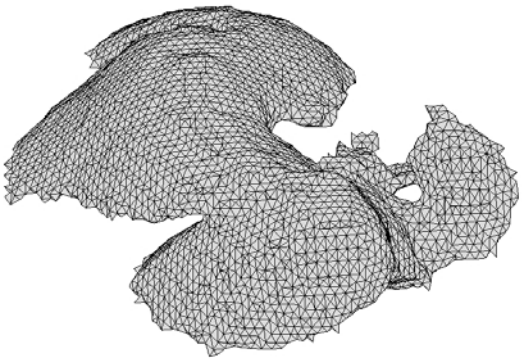

(c)

Figure 40. Wireframe renderings of the finite element model derived from segmentations of the acquired image volumes. (a) Pre-compression (*source*) mesh, (b) post-compression (*target*) mesh, and (c) internal boundary of the embedded mouse liver.

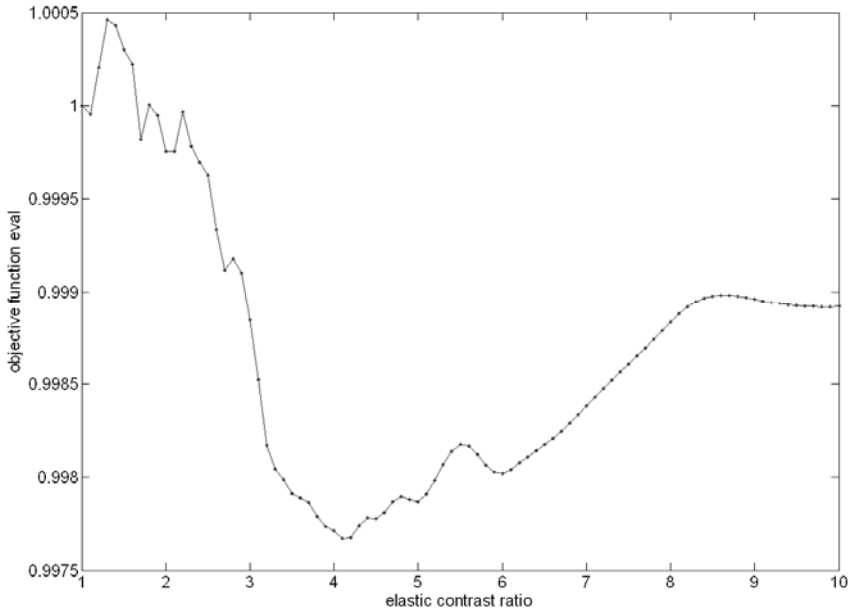

Figure 41. Objective function mapping of aggregate similarity as encountered by the MIE algorithm over an order of magnitude of elasticity contrast ratios. Values on the ordinate have been normalized to the evaluation at 1:1 (homogeneity).

Table 12. Elasticity contrast ratios obtained by different material property analyses

	Elasticity contrast (gel:liver)
Compression/stress	4.23:1
MIE	4.09:1

Discussion

This experiment represents a new and unconventional application of MIE due to the reversal of stiffness between lesion and surrounding material. The typical presenting problem in MIE has been the characterization and/or detection

of a firm object (e.g. a solid tumor) embedded within a pliable matrix. In this case, however, the surrounding polyacrylamide gel was actually stiffer than the fibrotic liver. We found that although there was sufficient contrast between the liver and gel that allowed for segmentation of boundaries, the overall variation in intensity was somewhat less than expected. Because the MIE algorithm depends on the presence of image texture in order to calculate similarity measures that drive the optimization, this sparsity of gray-level values is reflected in the shallow nature of the objective function and the presence of several local minima as shown in Figure 41. Despite this challenge, the reconstruction was still able to find the global minimum within six iterations (a runtime of approximately 24 minutes on a single 3.0 GHz Pentium4 Xeon CPU). The final elasticity contrast ratio results as displayed in Table 12 show a very close agreement between the two methods to within 3.3%.

Conclusion

This work represents the first attempt to utilize MIE for the material characterization of a biological tissue sample. The preliminary results compare well with previously published testing and indicate that the image registration technique of this algorithm is capable of producing elasticity contrast values equivalent to those derived from directly measured force data on a sample. As refinement in our data acquisition protocol progresses, the success of this initial experiment is of interest for providing further correlative analysis to the interrogation of soft-tissue systems.

References

[1] S. L. Barnes, A. Lyshchik, M. K. Washington, J. C. Gore, and M. I. Miga, "Development of a mechanical testing assay for fibrotic murine liver," *Medical Physics,* vol. 34, pp. 4439-4450, November 2007.

[2] J. J. Ou, R. E. Ong, T. E. Yankeelov, and M. I. Miga, "Evaluation of 3D modality independent elastography for breast imaging: a simulation study," *Physics in Medicine and Biology,* in press.

[3] J. M. Fitzpatrick, D. L. G. Hill, and C. R. Maurer, "Image registration," in *Handbook of Medical Imaging*. vol. 2 Bellingham, WA: SPIE Press, 2000, pp. 447-513.

CHAPTER VIII

SUMMARY

This work documents the process undertaken to develop and study a novel approach to elastography in the context of its possible clinical application for mammographic imaging. In contrast to the predominant techniques of the field that encode the spatial displacement of a tissue, we have investigated a recasting of the problem as an inverse methodology of iterative non-rigid, model-constrained image registration termed 'modality-independent elastography' (MIE). Chapters II, III, and IV detail the testing of MIE in detecting inclusions within a nearly planar geometry as well as further simulations with differing image acquisition modalities. The success of these experiments in two-dimensional systems provided a proof-of-concept platform for the method, helped formalize evaluation procedures of results, and provided insight into the factors affecting the fidelity of reconstructed elasticity images. Chapter V describes the creation of the first implementation of the MIE method that addressed issues involved with the transition to a fully three-dimensional algorithm. The performance of this new version was tested first in simulation and then in phantom experiments reported in Chapter VI. Finally, the diversity of application for MIE for tissue characterization is explored in Chapter VII.

The progress made in the course of this research has elucidated key elements for future study and demonstrates significant promise for its application in breast cancer detection. Indeed, at the time of this writing, a prototype system

derived from this work has been constructed and is undergoing refinement for preliminary clinical trial.